Università degli Studi di Modena e Reggio Emilia

DIPARTIMENTO DI SCIENZE FISICHE, INFORMATICHE E MATEMATICHE
Corso di Dottorato di Ricerca in "Physics and Nanosciences"

Tesi di dottorato

Tuning interfacial charge, adhesion and resistance to sliding by surface chemical modification.

Candidato:
Giulio Fatti

Relatore:
Prof. M. Clelia Righi

Ciclo XXXII, Anno accademico 2019-2020

Contents

Ought we not remind to ourselves
we who believe ourselves bound to
a finitude which belongs only to us,
and which opens up the truth of the
world to us by means of our cognition
ought we not to remind that we are bound
to the back of a tiger?
M. Foucault

Introduction

Friction is a ubiquitous phenomenon in nature, with massive energetic and environmental costs. It is calculated that around one quarter of the energy consumed in manufacturing, power generation and transportation is lost due to friction [1]. This huge energy consumption however is not unavoidable: it is estimated that improved tribology technologies might lead to a 40% reduction of the energy losses in around 15 years and to a 18% reduction in $\sim$ 8 years [2]. For this reason a considerable scientific effort has been devoted to understand friction since the birth of modern science. However, the fundamental mechanisms governing friction at the microscopic scale are still not fully understood. The reason resides in the complexity of the chemical and physical phenomena occurring at the sliding buried interface, which are extremely difficult to monitor experimentally. Atomistic simulations can play a key role as they allow to monitor the molecular-level mechanisms occurring at the sliding interface in real time. *Ab initio* simulations in particular provide a description of both the electronic and ionic degrees of freedom, which is essential to describe with high accuracy the chemical processes in condition of enhanced reactivity as imposed by the tribological conditions. This allows for a detailed microscopic description of many phenomena as the chemical reactions prompted by frictional forces, the formation of protective tribofilms, material and charge transfer across the contact interface and adhesive friction.

Surface chemical modifications play a key role in tribology. Protective tribofilms modify the surface reactivity and resistance to wear, as well as interfacial charge transfer, improving the tribological performances. Tuning these material (or inter-material) properties would then be of great importance to control friction and friction-related phenomena, like triboelectrification. This requires that a relation is identified between the tribological and the electronic/chemical surface properties. Understanding the inherent relation of intrinsic material properties and tribological phenomena would constitute a great step forward in the direction of a general understanding of microscopic friction.

Here we employ *ab initio* methods to investigate this relationship, focusing on three main topics: *i*) changing the tribological behavior of metal surfaces by elemental layer adsorption. We identify the chemical and physical properties that protective layers should possess to reduce

friction and wear of reactive metal surfaces. In particular, we study the capability of selected elemental monolayers to alter the surface electronic structure, so to reduce the chemical reactivity and thus the adhesive friction of iron surfaces. *ii*) The tribocatalytic conversion of hydrocarbons into graphene and other carbon nanostructures. Carbon-composite coatings are well known for their exceptional tribological properties [3–5]. Usually these films are deposited through various chemical techniques on the target surfaces. However, in tribological contact they eventually wear out, exposing again the underlying surface to high friction and wear. Self-replenishing carbon films formed within the tribological contact directly from the dissociation of hydrocarbon compounds represent an extraordinary technologically advance. Here we study the mechanism of graphene extraction from the tribocatalytic dissociation of methane molecules intercalated in nickel-nickel interfaces. *iii*) The triboelectrification of insulating polymers and solids. It is well known that electronic and ionic charge transfer across the interface in tribological contact. This effect is employed in many applications at the forefront of the technological innovation, including energy harvesting [6–8] and pharmaceutical technology [9–11]. However there is no explanation why this charge transfer should happen in insulators, where charge are not supposed to move. We studied the role of intrinsic electronic properties of polytetrafluoroethylene to understand its capability to retain negative charge at a fundamental level. Moreover, we studied the role of material transfer in silica-diamond hetero-interfaces in promoting charge transfer from silica to diamond.

Chapter 1

Challenges in modern tribology

In this chapter, after a brief resume of the historical development of tribology, we present some of the most intriguing challenges in modern tribology: *i*) real-time monitoring of the buried interface; *ii*) tuning adhesion by surface modifications, tribofilms and nanocoatings; *iii*) the mechanisms of triboelectrification.

1.1 Brief historic introduction

Friction has always impacted human activities. Since the ancient times the use of lubricants has been vital in manufacturing and transportation and smart solutions were often found heuristically. The first systematic studies on friction were carried out by Leonardo da Vinci more than two centuries before Newton. He stated that *i*) friction is independent of the area of contact; *ii*) friction is linearly dependent of the load imposed on the sliding body, which are currently known as the laws of dry friction. However da Vinci never published these studies, that remained unknown for nearly two more centuries, since the establishment of modern science. The laws of dry sliding friction were re-dicovered by Amontons at the end of the 17^{th} century, and extended by Coulomb in the 18^{th} century [12]. The Amontons' laws state that friction is directly proportional to the applied load and independent of the contact area: $F_{friction} = \mu F_{load}$ where μ, the *coefficient of friction*, is an empirical property of the sliding materials. During the 19^{th} century the industrial development required new techniques for controlling and reducing friction. This needed the study of lubrication. The work of Hirn, Petrov and Reynolds on one hand, and of Martens, Stribeck and Hersey on the other, led to the phenomenological understanding of lubricated friction, and the introduction of the Stribeck curve, reported in Fig. 1.1. It describes three different lubricating regimes as a function of the sliding velocity, the applied load and the lubricant viscosity.

These important advances provided a phenomenological description of friction phenomena

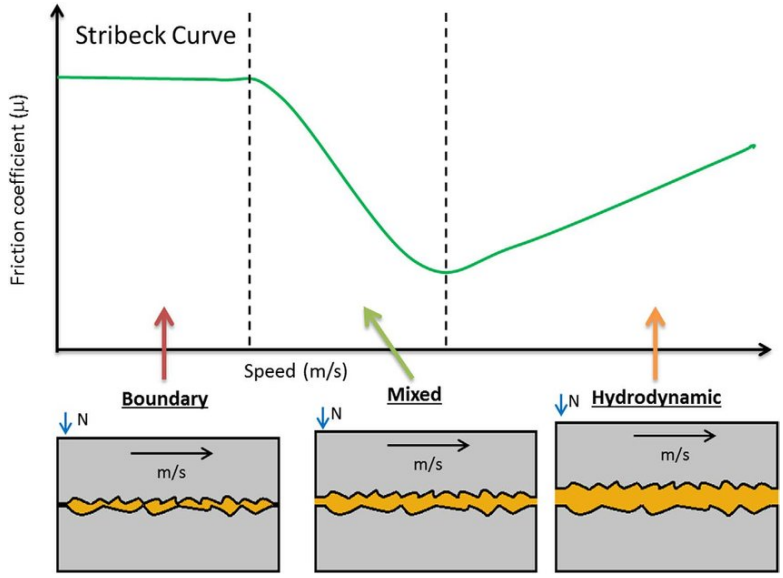

Figure 1.1: The Stribeck curve identifies three different friction regimes, with a minimum coefficient of friction at the beginning of the hydrodynamic lubrication zone. Image from [13].

at the macroscopic level. The first fundamental insight into the origin of friction came from the groundbreaking work of Bowden and Tabor at the end of the 50's [14], who introduced the concepts of real area of contact and adhesive friction. Between the end of the 1960's and the beginning of the 1970's the Surface Force Apparatus (SFA) was developed by Tabor and Israelachvili [15, 16], allowing to estimate both frictional forces and adhesion at the nanoscale. Thanks to this technological advance some major differences between macroscopic and microscopic friction became evident: for example at the nanoscale becomes possible to have a non-zero coefficient of friction even for a negative load, thanks to adhesive forces, *i.e.* chemical and physical bonds across the interface.

The development of tribology took advantage from the contemporary development of surface science. Experimental techniques like Auger Electron Spectroscopy (AES) and Low Energy Electron Diffraction (LEED) allowed the characterization of single crystal surfaces and the thin films adsorbed on them [17–19], which are important for tribochemistry, the subfield of tribology that studies chemical processes occurring in tribological conditions.

The advent of Atomic Force Microscopy (AFM) [20–22] constituted a key development for the birth of nanotribology. In AFM a single-asperity tip is connected to a cantilever, whose deflections allow to measure normal forces. A later adaptation allowed to measure also lateral forces, leading to Lateral Force Force Microscopy (LFM) or Friction Force Microscopy (FFM) [23]. FFM makes possible to measure the lateral and normal forces simultaneously, and thus to estimate the coefficient of friction for single-asperity microscopic contact. In this way the complexity of the multi-asperity contact is eliminated. These experimental advancements

were accompanied by theoretical studies aiming at unravelling the origin of friction in terms of chemical bonding and of energy dissipation processes. The mechanisms proposed involve the generation of a drag force due to the coupling of the tip electron density to the surface [24–26], the excitation of phonon modes in stick-slip motion, where the delocalization of the modes and their anharmonic coupling with other phonons transport the energy away from the interface [27, 28], atomic wear processes leading to the rupture of chemical bonds, dislocations and microscopic debris particle [21].

Molecular Dynamics (MD) simulations have been consistently used to integrate AFM experiments, allowing for a thorough investigation of single-asperity sliding contact [29]. Recently, *ab initio* MD simulations have also been adopted to study tribological phenomena such as tribochemical reactions [30], and charge redistribution during sliding [31]. In section 1.2 we shall discuss in more detail the experimental and theoretical techniques to study the chemical and physical processes occurring at the buried interface.

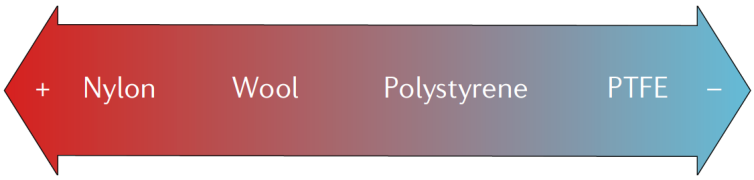

Figure 1.2: Stylized example of a tribolectric series. Materials on the left side of the series tend to charge positively when rubbed against materials on the right side of the series, which tend to charge negatively. Image from [32].

Another important friction-related phenomenon that has been intensively studied during the last century is triboelectricity, *i.e.*, electrostatic charging due to contact and rubbing. Electrostatic charging due to rubbing is commonplace and has been studied since the ancient times: although the often-referenced experiments by the Greek philosopher Thales never occurred, the phenomenon was mentioned already by Plato in his Timaeus [33]. The scientific analysis of triboelectricity however began much later. Around 1600, Gilbert distinguished materials that charge during rubbing (the insulators) from those that do not (the conductors) [34]. A second important discovery appeared in 1733, when du Fay reported that there are two types of triboelectric charge, positive and negative [35]. He initially believed that the type of charge is determined by the material, *i.e.* that a given material always charges either positively or negatively. However, some years later it was found that any material can charge with either sign, depending on the material against which it is rubbed. This led to categorizing materials in a triboelectric series. The triboelectric series is an ordering of materials such that, when two materials are rubbed against one another, the material left-side in the series (Figure 1.2) charges positively while the material on the right-side in the series charges negatively. However

triboelectric ordering is not well defined, since it was shown at the beginning of 20^{th} century that mechanical deformation can alter the material position in the triboelectric series [36]. Some years later it was first reported that rubbing two pieces of identical material together causes them to acquire opposite charges [37]. These findings show conclusively that triboelectric charging depends on many factors, not just the differences in chemical composition. A natural first step to the scientific understanding of triboelectric charging is determining the species that transfer charge between surfaces. Until the 60's electrons were deemed responsible for charge transfer, but then evidence emerged that adsorbed ions play a role as well [38]. When the aforementioned spectroscopic techniques for surface characterization became available, it was found that, as surfaces are rubbed, material fragments can be transferred from one surface to another and the transferred material could carry charge [39]. Further measurements demonstrated that triboelectrically charged surfaces exhibit areas of different polarity, typically with one dominant polarity, rather than being charged uniformly with a single polarity [40–42]. Progresses towards a fundamental understanding of triboelectrification have been hindered by the complexity of the phenomenon, so that deeper investigations seem to provide less clarity, rather than improving it.

In general, the large amount of data collected in the last decades has led to many crucial discoveries. However, the wide variety of concurring and interacting processes involved in tribological contact, and the difficulty in treating them in a comprehensive picture leave the microscopic origin of friction and triboelectrification elusive. We give now an overview of the most important open challenges in modern tribology, and of their relation to the topics of this thesis project.

1.2 Real time monitoring of tribological interfaces

Microscopic friction is governed by a variety of different physical and chemical phenomena: interfacial chemical bonding, phonon excitations, dislocations, wear, fractures, material and charge transfer across the interface. Furthermore, adsorbed films, whether in the form of intentionally applied lubricants or physisorbed contaminants, are ubiquitous at interfaces and must be taken into account in realistic studies [43, 44]. In particular in boundary lubrication the formation of protective layers on the sliding surfaces, called *tribofilm*, is the most effective way to reduce friction and wear. Understanding the chemical processes that generate these films is hence extremely important to improve the capability to control friction. This is no simple task as chemical reactions occurring under tribological conditions include several types of chemical processes [45]: *i*) mechanochemical reactions, *i.e.* chemical reaction processes initiated only by the mechanical stresses applied; *ii*) thermochemical processes (*e.g.* oxidation, polymerization,

and degradation); *iii*) heat enhanced tribochemical reactions controlled by both mechanical action and heat; *iv*) catalytic processes.

The above described phenomena generate a complex, non-linear and non-equilibrium dynamics that is difficult to describe. A major complication comes from the fact that the interface is buried, and it is not directly observable. A variety of approaches has been employed to overcome this issue. Important results have been achieved monitoring the onset of sliding friction and its precursors: Rubinstein *et al.* designed an experimental apparatus that allowed light to pass through the contact interface only at the actual points of contact, so that the light intensity was proportional to the area of contact. With this apparatus they could observe that the onset of frictional slip is governed by the propagation of a slow subsonic crack-front front, since no overall motion is observed before this front traverses the entire interface [46, 47]. With the same experimental setup it was possible to accurately determine the evolution of slip-stick motion in terms of detachment and re-attachment fronts and to conclude that the coefficient of friction depends on this complex dynamics and is not just a material property [48–51].

The characterization of tribofilm properties is of special interest for this thesis work. As already mentioned, the experimental observation and the characterization of tribofilm formation in real time is currently impossible. Valuable insights into tribological processes can nonetheless be obtained by comparative analysis of the surfaces before and after the friction experiment. Although the *post-mortem* spectroscopy does not give direct information on the reactions paths, it reveals the chemical composition of the tribofilm, the surface structure and defects generated by rubbing. By relating the spectra with friction measurements, the compounds that provide lubrication can be identified, while the comparison with the spectra outside the wear track allows to distinguish between tribochemical reactions and surface reactions, not activated by the mechanical stresses.

In liquid lubrication additive compounds are dissolved into the base oil, *i.e.* a mixture of different hydrocarbons chains. The most common anti-wear and friction modifiers additives are zinc dithiophosphate (ZDDP) [52] and molybdenum dithiocarbamate (MoDTC) [53]. ZDDP-generated tribofilms have been intensively studied on steel and iron surfaces, where phosphate or polyphosphate films are formed. These tribofilms have been experimentally characterized very accurately in their composition and morphology and correlated with their anti-wear action [54–56]. Recent characterizations were carried out by means of X-ray Photoelectron Spectroscopy (XPS), X-ray Absorption Near Edge Structure (XANES) and AES, often combined to get a complete chemical and morphological characterization [57–59], and reaction pathways have been proposed following different chemical approaches [60, 61]. MoDTC has been also studied since the 90's, and it is understood that its effectiveness is due to the tribologically-induced formation of molybdenum disulfide MoS_2 layers [53], a very well known 2D solid lubricant. MoDTC is also used in combination with ZDDP: the synergistic effect of the two molecules on

one hand enhances MoDTC transformation to MoS_2 [62], on the other hand shorter phosphate chains are dissociated on the surface, allowing the lubricated surface to carry higher loads [59]. There is no agreement about the dissociation pathway, that is still under investigation (see for example Ref. [63]).

Other lubricant additives of special interest to the scope of this work are organophosphorus [64, 65] and organosulfur molecules [66, 67]. In gas phase lubrication (GPL) experiments these molecules could be studied in dry contact with the surfaces, *i.e.* without the presence of the base oil [68, 69]. Spectroscopy measurements performed *in situ*, without exposing the sample to air after the tribo-test, provided valuable insights on the role of the lubricant molecules [65, 68, 70, 71]. For example in Ref. [68] authors studied the GPL of steel by organophosphorus compounds. *In-situ* XPS and AES revealed that the friction reduction observed in GPL could be attributed to the formation of an iron phosphide tribofilm. This implied the previous removal of the oxide layer and the exposure of the nascent iron surface.

At the nanoscale it is possible to monitor the forces at contact interfaces by using AFM. For example, an important measurement is the load dependence of friction [21, 72]. Microscopic friction can be characterized precisely in its dependence on the composition and on the morphology of the surface. A major result in this context is the observation of atomic stick-slip [23, 73], as well as the dependence of friction on the tip sliding speed [74, 75]. AFM can be used to monitor in real time and *in-situ* the microscopic growth of a tribofilm. These observations can be associated with *in-situ* spectroscopy analyses to identify the tribofilm composition. Moreover, by measuring the volume of the tribofilm while it forms allows for the determination of the reaction rates [76, 77].

In general, modern *in-situ* techniques make possible a stepwise monitoring and characterization of tribofilms growth: modern instrumentation allows spectroscopic and diffraction measurements on a sample to be conducted in significantly less time than a minute [78]. A good overview of the currently available experimental techniques is given in Ref. [79]. However, stepwise analysis may be misleading in cases where dividing the mechanical treatment into segments leads to products different from those obtained from continuous rubbing.

Nowadays a real time monitoring of sliding asperities in contact is only possible by means of Transmission Electron Microscopy (TEM). *In-situ* TEM permits direct observation of the asperities while they are brought into contact, sliding, and separation, and allows precise measurements of the contact geometry, and its change during sliding [80, 81]. Limitations of test platforms still exist which reduce image quality [82]. Moreover, this method allows to observe in real time wear and mechanical phenomena [83], but not to observe nor to measure tribochemical processes.

MD simulations are a key tool to overcome the described shortcomings of the experimental methods. They allow to calculate the forces acting between the atoms of a system and to

describe the resulting dynamics by solving numerically the Newton's equations of motion. In classical MD atomic forces are calculated as the gradients of potentials, or force fields (FF's), parametrized empirically. Classical devised FF's are nonreactive, *i.e.* they cannot describe bond formation and rupture accurately. Hence they can be applied to describe mechanical and structural features not depending on the chemical activity at the interface. Despite this major limitation, these kind of FF have been successfully employed to explain the atomic mechanisms underlying important friction phenomena. The role of commensurability between paired sliding surfaces has been understood in its microscopic origin: if the surfaces are incommensurate, because of their different lattice constants, symmetries or orientations, it becomes harder for surface atoms to interlock collectively with the counter-surface and sliding becomes easier. In suitable conditions, the coefficient of friction can decrease to almost zero, reaching a regime that has been named superlubricity [3, 84–86]. Another major result is the breakdown of continuum contact mechanics: it was shown that the pressure field distribution on tips in contact is inconsistent with the predictions of any known continuum contact models, independently of the tip geometry [87, 88]. Nonreactive simulations can also be employed to study the phase transition-controlled dynamics of confined films depending on velocity, concentration and geometry of the film [89, 90]; or to simulate indentation and nano-wear [91, 92].

The impossibility to consider chemical activity in tribological conditions however constitutes a serious limitation of classical MD. A reactive FF (ReaxFF) has been thus designed to include in the classical framework the possibility to form and break bonds [93] without recurring to the more computational expensive quantum methods. Many version of this potential have been parametrized in the last years to provide a description of the first chemical steps leading to the formation of a tribofilm [94, 95]. However, ReaxFF current parametrizations do not necessarily reproduce accurately the interactions under tribological conditions, where the confinement and the mechanical stresses can destabilize the electronic structure of the compounds, with consequent changes in their reactivity.

An *ab initio* approach allows to accurately describe chemical processes occurring in conditions of enhanced reactivity. The use of first principles calculations to investigate tribochemical processes has increased significantly in the last decades. Within this approach, the tribochemistry of different lubricant materials such as diamond and diamond like carbon [30, 96–98], layered materials [99–104] and lubricant additives [105–111] have been successfully studied. The main focus of these studies has been on the effects of tribochemical modifications on the adhesion and shear strength, while few studies [30, 97, 98, 101, 104] analyze the occurrence of these reactions in real time.

We applied AIMD to monitor the tribologically induced formation of a carbon nano-coating from methane molecules, providing insights into the microscopic mechanisms underlying the formation of a self-replenishing carbon tribofilm, as observed by an associated experiment

(chapter 4).

As described in the next section we also applied static first principle calculations to describe surface chemical modifications leading to friction reduction.

1.3 Modifying interfacial adhesion by layer adsorption

To reduce friction and wear of a surface it is often necessary to modify its mechanical and chemical properties. An efficient way to do so is through the formation of protective tribofilms, as we have already mentioned. Understanding the way tribofilms alter surface properties, and ultimately which kind of modifications reduce friction is important, both for fundamental understanding and practical applications. In particular such understanding is necessary to design new, effective, and possibly environmental-friendly lubricant additives. During the tribological process, sliding surfaces are scratched under the effect of very high stresses, and reactive native surfaces are exposed. The newly generated dangling bonds tend to form new chemical bonds across the interface, giving rise to high adhesion and coefficient of friction. Preventing the formation of these interfacial bonds is then critical to keep friction under control. Tribofilms can achieve this goal either by acting as anti-wear coating, *i.e.* protecting the surface from bond ruptures and avoiding the exposure of reactive nascent surfaces; or saturating the exposed dangling bonds and reducing the surface reactivity by passivation.

Interfacial adhesion can be reduced by covering the surfaces with inert layers that interact through weak van der Waals forces, that do not influence much the energy barriers to be overcome for lateral motions [112]. Indeed layered materials as graphene and transition metal dichalcogenides, as MoS_2 [113–115], have long been used as solid lubricants. If the layer binds chemically to the surface, it saturates at least a part of the surface dangling bonds. Therefore, the surface passivation by layers adsorption renders the surface less reactive and hinders the formation of bonds across the interface, causing a decrease of the interfacial adhesion and of adhesive friction [103, 116].The interfacial commensurability affects the sliding properties of physically-interacting surfaces. It has been shown for example that xenon monolayers slippage on gold is much higher than on graphene in spite of the same physical nature of the interactions [117]. The different behaviors are due to the different lattice match of the Xe islands formed on the two surfaces at the nanoscale [118].

A quantitative measurement of the interfacial adhesion can be obtained by first principle calculations. Moreover, the potential energy surface (PES) experienced by a slider when moving on a substrate can be constructed by calculating the adhesion for different lateral positions of the two surfaces in contact [120]. The PES provides information on the ideal energy barriers that must be overcome by the sliding surfaces to move along a given direction, and the corre-

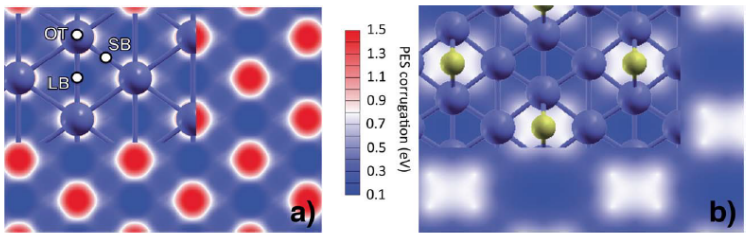

Figure 1.3: Two-dimensional representation of the PES's obtained for the clean (a) and the P-iron interface (P atoms are in yellow) at relative concentration of 0.25. The common energy scale shows the effectiveness of P adsorption in reducing adhesive friction. Image from [119].

sponding forces can be obtained calculating numerically the gradients along that direction. The adhesion and the shear strength calculated from first principles constitute important figures of merit for tribological interfaces [31, 103, 111, 121]. In this way, the effectiveness of several nanocoatings has been understood at the microscopic level. For example, the lubricating properties of graphene, phosphorus and sulfur on steel/iron have been explained by analyzing the role of passivation in adhesion reduction [103, 111, 116, 119, 122]. In particular a theoretical study compared sulfur efficacy to phosphorus. S was found to be around five times more efficient than P in reducing the adhesion and around two times more efficient in reducing the shear strength along the minimum energy path, in agreement with the corresponding coefficients of friction measured in experimental tests. The lubricating mechanism was suggested to be similar for P and S, while the different effectiveness was attributed to the different valence structure of the two elements [111]. These findings have confirmed the efficacy of the iron sulfides and phosphides tribofilms formed from the dissociation of additive molecules, as we mentioned in the previous section (see Fig. 1.3).

Similarly, it has been shown that the ultra-low friction of diamond like carbon (DLC) coatings in humid environments can be attributed to the dissociation of water molecules and to the formation of an H- and OH-terminated carbon surfaces. In the presence of hydrogen H_2 molecules, the passivation is enhanced and superlubricity can be obtained [120, 123–125]. A different mechanism was found for Si-doped DLC surfaces. An experimental work found that the key factor to lubrication in a humid envorinment is the deposition of a water layer of thickness ranging from 1 nm and 4 nm [126]. The deposition of the water layer was related to hydroxyl groups bonded to the Si atoms, detected by means of XPS [127, 128]. The microscopic mechanism was explained by employing *ab initio* MD simulations. Simulations showed that hydroxylation is accelerated by Si dopants: surface silicons lower the dissociation barrier, enhancing the surface reactivity up to five times. The radial distribution function for the $O \cdots H$ bonds showed that surface-molecule bonds had a similar profile to molecule-molecule bonds, suggesting that the adsorbed hydroxyl group participated to the hydrogen bond network of the

water film confined at the interface, anchoring a thin water film to the surface. The increased wettability was related thus to the increased lubricity of Si-doped DLC [97].

In a recent publication Wolloch *et al.* found a direct and more general connection between adhesion, the PES, and interfacial charge density variations. They performed a systematic study of the correlation between charge displacement occurring when an interface is formed and the PES corrugation, scanning a large number of monoatomic crystals and layered materials. They showed that the interfacial charge density and its variation during sliding are the basic physical quantities which determine the adhesion and the frictional forces. This work uncovered the existence of a direct relation between the electronic surface rearrangement and relevant tribological properties of solid interfaces [31].

Despite the relevance of surface passivation in controlling friction, it must be noted that not every kind of passivation automatically provides lubrication. An important counterexample is given by iron oxide: even though the oxidization process passivates iron surfaces, iron oxide surfaces are still subject to very high friction and wear. By means of first principles calculations oxygen and phosphorus adsorption were compared. The different tribological behavior was attributed to the smaller atomic dimension of oxygen, so that despite a similar amplitude modulation of the PES in the two cases, the PES period was found to be much shorter in the case of oxygen, giving rise to higher forces and interfacial shear strength [119].

In this work we will provide new insights about the surface chemical modifications induced by elemental adsorption: in chapter 2 we will show that passivating species should induce specific surface modifications to reduce adhesion and friction. In particular, we will compare the adsorption of sulfur, phosphorus, which provide lubrication, and of nitrogen and oxygen, which do not. Analyzing the different effect on the charge density and on the work function we will suggest an explanation of this major difference. In chapter 3 we will show that the chemical modification of iron surface properties by elemental selenium adsorption provide a strong reduction of the resistance to sliding, due to a particular rearrangement of the charge density at the surface-adsorbate interface. Comparing selenium to phosphorus and sulfur adsorption, we will show its high efficacy as a new possible key element for lubricant additives.

1.4 Triboelectrification in insulators and semiconductors

Tribolectrification is an important phenomenon in friction, contributing significantly to the coefficient of friction [129], but it is not much more understood than friction itself, since it is a very complex phenomenon. First, macroscopic effects originate from rare events, making their theoretical description and experimental observation challenging. Typically the surface charge

density produced by triboelectrification is of the order of $10^{-4}\,\mathrm{C/m^2}$, corresponding to 1 electron per $1000\,\mathrm{nm}^2$ patch of surface. Moreover, this net change does not correspond to a single electronic charge being transferred but, rather, to a little imbalance between a larger amount of charge transferred in both directions across the interface. Second, charging depends strongly on surface morphology. This dependence is observed even for pristine materials in vacuum and it is exacerbated by environmental effects such as water adsorption [130]. A distinction is often made between triboelectric charging occurring during rubbing and simple contact charging, but the distinction may be misleading because what appears to be simple contact on the macroscopic scale actually consists of localized rubbing between nano-asperities. Third, all of the phenomena involved are intrinsically non-equilibrium because neither tribocharging nor discharge appear in equilibrium conditions [131], and both rely on the input of mechanical energy that is rapid compared with charge relaxation times. Fourth, any contact between surfaces typically involves making and breaking of bonds. Tribochemistry has important consequences on tribocharging: the breaking of interfacial bonds has been known for centuries to generate charging and luminescence [132, 133].

There have been many attempts to identify the key factors driving tribocharging. The research has focused mainly on the following aspects: *i*) the role of intrinsic material properties; *ii*) electron transfer upon contact; *iii*) ion transfer; *iv*) tribochemistry. *i*) Investigations on materials properties have focused on work functions, surface hydrophilicity, roughness and hardness among other issues. For example, a number of studies over the past several years have sought to clarify charging mechanisms by adding monolayers, both with electron-withdrawing (halide) and electron-donating (amide) groups, to the surfaces of oxide and polymer materials. These studies revealed that the addition of surface halide groups consistently moves the material toward the negative side of the triboelectric series, whereas added amide groups move the material to the positive side [134–136]. Similarly, it has been shown that by negatively (n)-doping 2D MoS_2 (ordinarily highly negative in the triboelectric series) produces an excess of electrons that can be transferred to another surface upon contact, so moving MoS_2 to a more positive position in the triboelectric series [137]. These studies appear to support the notion that electron affinity drives charge transfer. The different conclusions highlight that different mechanisms may be relevant under different conditions or for different materials.

ii) Models of electron transfer between two metals are relatively straightforward. Metals are characterized by their work functions ϕ, *i.e* the energy required to remove one electron. When two different metals come into contact, electrons flow from the metal with the lower work function to the metal with the higher work function, reaching an equilibrium state when the potential difference due to the accumulated electrons in the higher work function metal exactly cancels the original work function difference. During separation of the metals, electrons would tend to flow back, and in infinite time would return to the neutral equilibrium state.

Finite-time processes, however, do not reach the equilibrium: the electron backflow during separation is opposed by the increase of the distance between the surfaces, and surfaces residual electrons typically remain on the high work function metal. It should be noted that most metals are covered by insulating oxide layers. In those cases the simple work-function model describes triboelectric charging poorly. Tribocharging of insulators is much more difficult to describe in terms of electron transfer. Insulators are characterized by a filled valence band and an empty conduction band, separated by a large energy gap. This bandgap prevents insulators from transferring electrons without a significant energy penalty. Yet insulators charge even more strongly than metals. Several attempts have been made to address the lack of a suitable models for tribocharging in insulators. One approach proposes that defects or surface states provide intermediate states for electrons to bridge the bandgap [130]. More recent approaches involve mechanisms by which interactions between surfaces create a driving force for electrons to transfer. This involves a delocalization of electron wavefunctions due to contact and material strain [138–140]. The kinetic energy of electrons decreases when electron densities and their gradients decrease. The presence of a nearby surface allows electron states on one surface to hybridize with those on the contacting surface, such that the electrons delocalize, decreasing their density and density gradients, thus lowering their kinetic energies. Other atomistic simulations have shown that lattice deformations generate surface dipoles, which produce a net electric field that could drive charge transfer.

iii) More recent experiments have provided evidence that insulators charge metal surfaces through ion transfer [141, 142]. Some materials are composed of molecules that can easily dissociate as ions. It has been showed that, when a counter-surface is paired with the first, triboelectrification results from the transfer of the weakly bound ions to the opposing surface, leaving the strongly bound ions on the first [143, 144]. However, ion transfer appears to be relevant even in the case of materials that cannot contribute mobile ions. In these cases, adsorbed ions coming from the environment are believed to play a role, as it has been proved in the case of polymers [145]. Similarly, isolated metals spontaneously gain and lose charge as humidity is raised or lowered. It has been proposed that atmospheric water can serve as a charge donor or acceptor [146]. It has been also found that charged insulators are found to reversibly transfer charge through the air, which can be attributed to airborne ions [147]. Remarkably, studies have shown that triboelectric charging occurs in systems constructed so that there are no adsorbed ions. In particular, an experiment analyzed triboelectric charging under ultra-high vacuum conditions using a PTFE sample cleaved in vacuum, and found similar charging phenomena as those observed in air [148]. Overall, there appears to be evidence both implicating and excluding adsorbed ions as triboelectric charge carriers.

iv) Contact between surfaces creates stresses that can alter or break chemical bonds, or expose new surfaces to contact. It has long been appreciated that the mechanochemistry

resulting from surface contact can affect charge transfer in multiple ways [149]. Studies have shown that the triboelectric charging of polymer systems leads to formation of radicals, that stabilize proximate electrostatic charge [150]. Kelvin probe force microscopy has also been used to examine the role of tribochemistry in triboelectric charging, revealing the existence of intertwined micron-scale regions (mosaics) of positive and negative charge on triboelectrically charged surfaces [151, 152] . The polarity of charge was attributed to electron transfer from the less electronegative to the more electronegative radical. This has been shown for example in Polyethylene (PE)-Polytetrafluoroethylene (PTFE) contact, where the PTFE is rendered negative and the PE positive [153].

In complex materials, additional mechanochemical effects can occur. Natural rubber is a notable case: it exhibits strong tribocharging when stretched. In fact, mechanical strain can even reverse the sign of charging, as it has been shown for PTFE in contact with stretched rubber [154]. The relation between strain and tribochemical charging has been probed in experiments on a polymer glass subjected to inelastic deformation. These experiments show that inelastically deformed materials exhibit triboelectrical behaviors different from their undeformed counterparts [155]. Finally, a role is played also by surface roughness: this effect may be due to the difference in the concentration of excited species on rough and smooth surfaces [156].

In conclusion, irrespective of the details of charge carriers or mechanisms, it appears clear that tribocharging is not driven by a single dominant factor, but is governed by competing and unstable dynamical processes. With this perspective, in chapter 5 we propose an analysis, by means of DFT calculations, of the high pressure phase structure (electronic and geometric) of PTFE, identifying electronic features that suggest an explanation of its capability to retain charge. In chapter 6 we propose a possible mechanism competing in the charge transfer between silica and diamond, involving both electron and ion transfer. The *ab initio* investigation is supported by experiments that demonstrate the role played by electronic and ionic triboemissions.

Part I

Surface Properties Modification by Atomic Adsorption

Chapter 2

Iron Surface Passivation by Different Adsorbates

2.1 Introduction

[1] Transition metal phosphides exhibit a variety of phases, where the phosphorus networking changes considerably with the concentration. P-P-P angles and P-P distances can span wide ranges of values according to the stoichiometric ratio and the metal framework. These features provide iron phosphides (nano)structures with a large variety of magnetic, catalytic, electronic properties that can be exploited for a myriad of applications [158, 159]. The presence of phosphorus on the surface of iron modifies its interaction with deposited molecules [160, 161], and plays an important role in corrosion protection and heterogeneous catalysis. The segregation of phosphorus at grain boundaries enhances the intergranular embrittlement of iron [162–166], and increases the probability of intercrystalline fractures.[167, 168] Phosphorus is a key element in the composition of extreme pressure lubricant additives used in engine oils [66]. The formation of P-rich iron tribofilms is connected to the friction-reduction and wear-protection properties of steel-on-steel sliding contacts for reasons that are still unclear at the atomic level. Recent gas-phase lubrication experiments combined with *in situ* spectroscopy analysis revealed that the tribofilm produced by phosphite additives on steel is mainly composed by iron phosphide [68], and first principles calculations showed that elemental phosphorus is able to reduce the adhesion and shear strength of iron interfaces [119]. This capability has been reported also for sulphur [31, 111] and graphene,[103, 116] but not for other elements such as oxygen [119]. To provide a physical rationale for these observations is important to understand the phosphorus interaction with the iron surface and compare it with those of other elements.

In the last years several papers have been published reporting results of both theoretical and

[1] Work first published as Ref. [157]

experimental studies on chemisorption of S[169–174], N [175–178], and O[109, 179–185], on the low index surfaces of iron, but no detailed analysis for P adsorption has been reported yet. At the present time it is not known how phosphorus chemisorption may affect the structural and electronic properties of iron surfaces and how relevant to these properties are the interactions between the adsorbed atoms.

Here we report the results of a systematic theoretical study based on Density Functional Theory (DFT) of P adsorption onto the Fe(110) surface at different coverages. For each coverage, we determine the most stable chemisorption site, the adatom-induced modifications in the substrate geometry, the charge density distribution, local density of electron states and work function. The comparison among P, S, O, and N obtained by applying the same theoretical approach, allows us to point out significant trends and differences in the metal passivation. In particular, we consider the competition between the adatom-adatom interaction and the adatom-substrate interaction, and we find that the former tends to prevail in P and S overlayers at high coverages, with impact on processes such as lubrication and embrittlement.

2.2 Computational method

We perform spin-polarized density functional theory calculations using the Quantum ESPRESSO computer program [186]. The exchange-correlation functional is described by the Perdew-Burke-Ernzerhof (PBE) generalized gradient approximation [187]. The ionic species are described by ultrasoft pseudopotentials, the semi-core states (3s and 3p) are included in the valence of the Fe pseudopotential, which thus presents 16 electrons. The electronic wave functions are expanded in plane-waves. A kinetic energy cut-off of 30 Ry (240 Ry) is chosen to truncate the expansion of the wave functions (charge density). This compututational set-up allows us to obtain an accurate description of iron bulk: the calculated lattice parameter, $a = 2.852$ Å, bulk modulus $B = 161$, and magnetic moment, $M = 2.29\ \mu_B$, are in good agreement with the experimental values [188] of $a_{exp} = 2.867$ Å, bulk modulus $B_{exp} = 170$, and magnetic moment, $M_{exp} = 2.22\ \mu_B$.

The Fe(110) surface is modeled by supercells with (2×2) in-plane size, containing an iron slab and a vacuum region of 25 Å to separate the periodic replicas along the z direction. The optimal slab thickness is identified by testing its effects on the calculated adsorption energy and work function. The adsorption energies are found comparable for every considered thickness, from 3 to 11 layers, whereas the work function converges using a 5 layers thick slab. The latter slab thickness is, thus, chosen for the subsequent calculations. A $4 \times 4 \times 1$ Monkhorst-Pack grid is used to sample the Brillouin zone of the supercell [189], and a gaussian broadening is used for the calculation of fractional occupancies, with a smearing width of 0.02 Ry. The

work function is calculated using the effective screening medium method to avoid the effects of spurious electric fields [190] and the partial charges are calculated by means of Bader analysis [191–194].

2.3 Results and discussion

2.3.1 Adsorption energy and geometry

The Fe(110) is not reconstructed, but the break of the translational symmetry along the surface normal leads to small changes in the vertical distances between the first atomic planes. First, we present the relaxation parameters obtained for the clean iron surface, which are compared with the experimental values. We calculated the structural features of bulk iron: we found an interlayer distance $d = 2.017$ Å, in good agreement with the experimental value 2.019 Å[195, 196]. On the Fe(110) surface, the vertical distances d_{ij} between the first i, j atomic layers surface undergo small changes, although the surface is not reconstructed. The relative distance variation is expressed by the quantity $\Delta_{ij} = \frac{d_{ij}-d}{d}$. A negative value corresponds to a contraction of the interplanar distance, *viceversa* a positive value indicates an expansion. The calculated Δ_{12} between the surface and the first plane is -0.32%, while Δ_{23} turns out to be expanded 0.89%.

Figure 2.1 compares the projected density of state (PDOS) of the surface and mid-slab atoms, with the PDOS of a bulk iron atom. It shows that the slab internal plane mimic accurately enough the electronic properties of the bulk calculation.

Once checked the iron slab properties, we studied the adsorption properties. Fig. 2.2a offers a top view representation of the Fe(110) surface, where high symmetry adsorption sites, namely the long bridge (LB), short bridge (SB), and on top (OT) sites, are indicated. The adatom adsorption energies at these sites is calculated for three different coverages, $\theta = 0.25$, $\theta = 0.5$ and $\theta = 1$ monolayer (ML), corresponding to the p(2 × 2), c(2 × 2), and p(1 × 1) adlayers represented in Figs. 2.2b-d. The adsorption energy per atom E_{ads} is obtained as

$$E_{ads} = (E_{slab+na} - nE_a - E_{slab})/n \tag{2.1}$$

where $E_{slab+na}$ is the total energy of the iron surface covered by n adatoms, E_a is the energy of the isolated atom and E_{slab} is the energy of the clean iron surface. The adsorption is energetically favorable if $E_{ads} < 0$. We use the term binding energy to indicate the absolute value of E_{ads}.

The LB site, presenting the highest coordination, turns out to be the most favorable for P adsorption at all the considered coverages. However, the energy difference among the adsorption

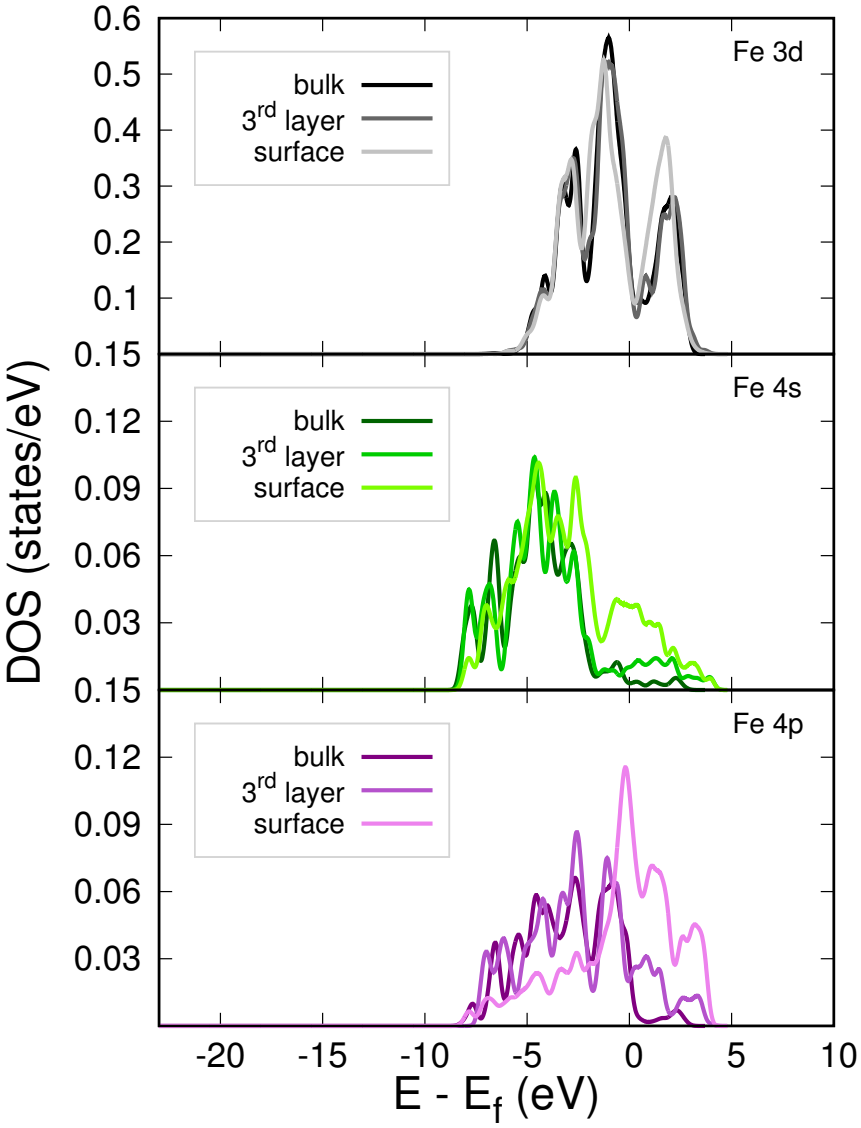

Figure 2.1: PDOS's of clean surface and mid-slab plane iron atoms *vs.* PDOS's of bulk iron.

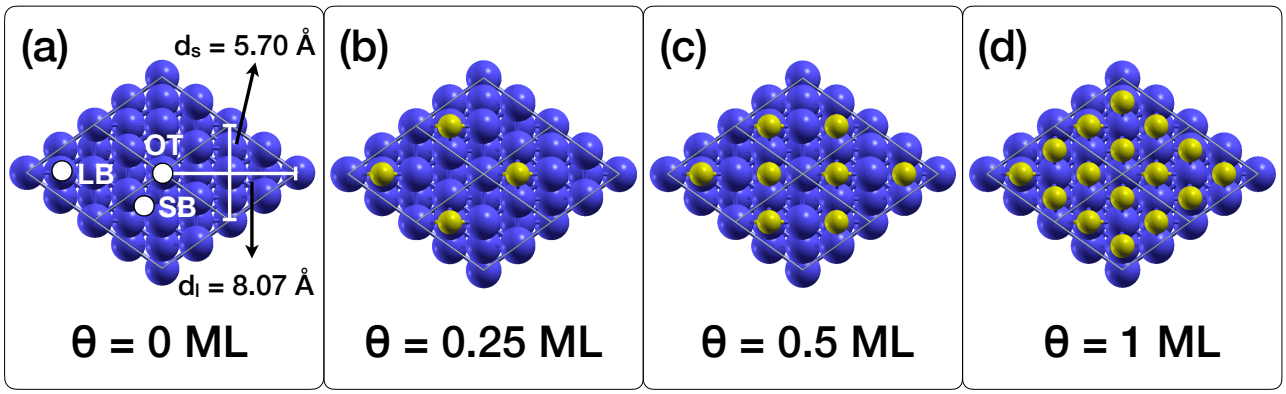

Figure 2.2: Top view of the Fe(110) surface. In panel (a) high symmetry sites are indicated on the clean surface ($\theta = 0$). Panels (b)-(d) show the atom arrangements considered to realize different coverages. P (Fe) atoms are colored in yellow (blue).

adsorption site	coverage (ML)	E_{ads} (eV)
LB	0.25	-5.25
	0.5	-4.92
	1	-4.11
SB	0.25	-4.71
	0.5	-4.36
	1	-3.96
OT	0.25	-4.01
	0.5	-3.92
	1	-3.65

Table 2.1: Adsorption energies per P adatom at the different sites and coverages represented in Fig.2.2

sites reduces by increasing the adatom concentration (see Tab. 2.1a). At $\theta = 0.25$ ML the energy difference between the OT and the LB sites is about 31%, while at $\theta = 1$ ML is 13%.

The P adsorption energy in the LB site is compared in Fig. 2.3b with those obtained for S, N and O adopting the same computational scheme. The binding energies are also reported in Tab. 2.2. We observe that the most favorable coverage for P adsorption is 0.25 ML, which is also the most favorable concentration for the other considered elements, in agreement with previous studies [109, 173, 175].

At $\theta = 0.25$ ML, the P atom is located at a vertical distance $z_A = 1.50$ Å from the iron surface and forms four bonds of $l_{long} = 2.44$ Å and $l_{short} = 2.19$ Å lengths with the surrounding Fe atoms (Tab. 2.2). The surface slightly reconstructs to form four equivalent bonds: the l_{long} is reduced by 2.8% while l_{short} is stretched by 7.2% with respect to the clean surface. Similar changes are observed for S, O and N at $\theta = 0.25$ ML coverage, with larger variations as the vertical distance between the adsorbate and the surface gets shorter (see Tab. 2.2).

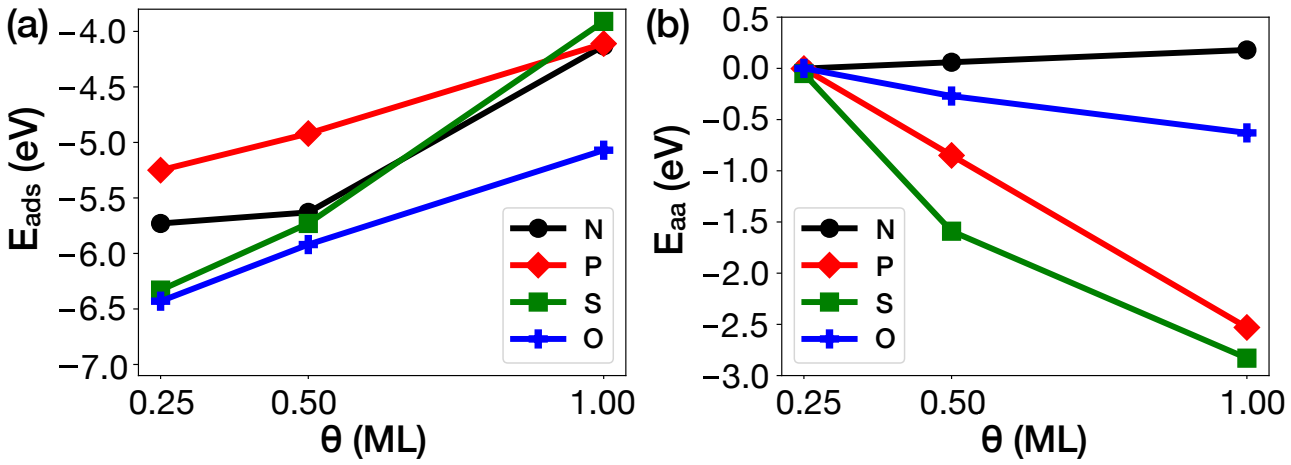

Figure 2.3: Calculated adsorption energies *vs.* coverage for (a) P, N, P, S, O, compared in the LB site; (b) Adatom-adatom interaction energies in isolated layers having the same structure of the deposited layers

As to the iron inter-layer distances, one can notice that while in the clean surface there is an inward relaxation of the order of 0.3%, after P adsorption the d_{12} distance between the first and the second iron layer increases, and the d_{23} distance between the second and the third layer decreases. The changes are very small, of the order of 0.4%, but significant enough to indicate that the strong P-Fe bonds formed upon adatom deposition weaken the Fe-Fe back bonds of the surface metal atoms to the underlying atomic plane. The comparison with the other adsorbates shows similar effects, larger in the case of N and O adsorption. The binding energies of all the elements decreases with coverage, as can be seen in Fig. 2.3a. The extent of such reduction is different for each element: when passing from 0.25 to 1 ML coverage it decreases by 21% for O, 22% for P, 28% for N, and 38% for S. These different trends make the relative energy gain upon

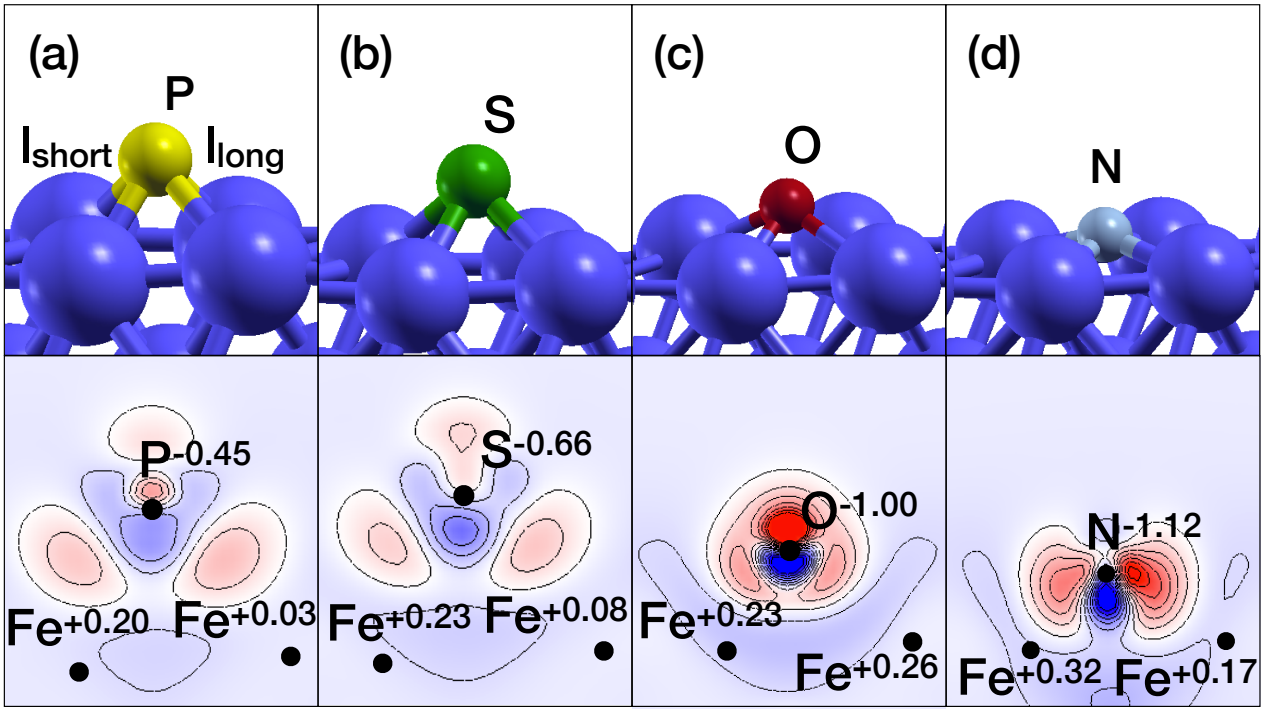

Figure 2.4: Lateral view of the optimized adsorption geometry of P (a), S (b), O (c), N(d) elements at the fourfold LB site. The bottom part of each panel represents the charge density redistribution occurring upon adsorption at 1/4 ML coverage calculated according to Eq. 2.3. The color scale ranges from -0.025 e/Å^3 (blue) to 0.03 e/Å^3 (red)

adsorption to change with coverage: at low coverage P adsorption is less favorable than the adsorption of the other considered elements, while it becomes as energetically favorable as S and N adsorption at high coverage, where O adsorption remains the most exothermic process. The decrease of the binding energy with coverage may be attributed either to a repulsive electrostatic interaction among the adsorbates, as a consequence of charge transfer from the substrate [197, 198], or to an attractive interactions due to the formation of chemical bonds among the adsorbates that weakens the adatom-substrate bonds, as previously suggested for oxygen and sulfur [172, 173, 182].

To clarify this point we calculates the cohesive energy of the deposited layer:

$$E_{aa} = (E_L - nE_a)/n, \tag{2.2}$$

where E_L is the energy of an isolated layer with the same geometry of the adsorbed layer. As can be seen in Fig. 2.3b, the adatom-adatom interaction energy is negligible in the p(2×2) layer, where the shortest adatom-adatom distance is 4.98 Å. While in the P and S cases it becomes attractive and of increasing strength when the distance among the atoms decreases to 4.03 Å and 2.49 Å as in the $c(2\times2)$, and $p(1\times1)$ layers, respectively. This indicates that P-P and S-S bonds are formed at higher coverages, while in the N and O cases covalent interactions among the adatoms are almost absent.

	E_{bind} (eV)	z_A (Å)	d_{12} (Å)	d_{23} (Å)	l_{long} (Å)	l_{short} (Å)	Δq (e/a)	$\Delta\phi$ (eV)
	5.25	1.503	2.019	2.025	2.437	2.187	0.45	0.41
P	4.92	1.575	2.040	2.017	2.489	2.212	0.28	0.63
	4.11	1.830	2.029	2.017	2.723	2.320	0.17	-0.25
	6.33	1.529	2.025	2.025	2.053	2.199	0.66	0.33
S	5.73	1.553	2.053	2.025	2.025	2.173	0.51	0.32
	3.91	1.897	2.038	2.019	2.053	2.373	0.31	-0.54
	5.73	0.573	2.050	2.042	1.961	1.773	1.12	0.13
N	5.63	0.779	2.072	2.046	1.958	1.702	0.99	0.41
	4.13	0.937	2.144	2.023	2.217	1.707	0.67	1.49
	6.43	1.004	2.039	2.022	2.181	1.858	1.00	0.31
O	5.92	1.085	2.047	2.020	2.253	1.842	0.94	0.95
	5.07	1.154	2.056	2.027	2.311	1.850	0.87	2.05

Table 2.2: Binding energy, E_{bind}, geometrical parameters (see definitions in the text), work function change $\Delta\phi$ and partial electronic charge, Δq, calculated for the different adsorbates. For each element the values obtained at three different coverages, namely 0.25, 0.5, 1 ML, are reported in adjacent rows.

The different bonding behavior of the P and S elements with respect to the N and O ones is reflected in the adsorption geometry. While the vertical adatom-substrate distance

z_A increases for all the considered species, the substrate inter-layer distances show different trends. In particular, the spacing between the outermost Fe atomic planes, d_{12}, increases by increasing the P or S concentration up to 0.5 ML, and then decreases. A monotonic increase of d_{12} with the coverage is, instead, observed for N and O adsorption. The picture that can be drawn from these results is that initially the P-Fe (S-Fe) bond is strong enough to induce a progressive expansion of d_{12}, which tends to become close to the bulk value. Upon increasing the coverage, the outward relaxation of the first plane cannot be sustained and the substrate tends to return to values closer to those of the uncovered metal. This indicates a weakening of the adatom-substrate bonds, which is caused by the strengthening of the adatom-adatom bonds. On the other hand, d_{12} shows an almost linear increase as a function of the N (O) coverage, indicating that the weakening of the chemisorption bond is not so significant to reverse the tendency of reducing the back bond intensity. This is consistent with the fact that the bonds among the adsorbed atoms are not relevant in these systems and suggests that the reduction of the adsorption binding energy has to be imputed to lateral repulsive interactions between the adsorbates. The increasing importance of the adatom-adatom interactions passing from low to high coverage has been pointed out for the S/Fe(110) system previously [173]. In the present paper besides extending the conclusion to the phosphorus case, we relate such behaviour to the overlayer energy E_{aa}, and we provide an explanation of the different behaviour of the other adsorbates.

2.3.2 Charge transfer and work function change

To gain further insight into the processes that determine the decrease of the binding energy with coverage, we calculate the electron transfer per atom. Indeed, the analysis of the adsorption energies and geometries reported in the previous section suggests that the ionicity of the chemisorption bond may play the major role in N and O adsorption. Electrostatic interactions are commonly considered more important for electropositive rather than electronegative adsorbates because the latter tend to bond closer to the metal substrate, and therefore are better screened [199]. However, this argument seems here to be relevant at low coverage only, since the vertical distance between the adsorbates and the substrate, z_A, increases with coverage (Tab. 2.2). The partial charges per atom, calculated according to the Bader method [191–194] are reported in Tab. 2.2, and Fig. 2.5a. As with any partitioning of the electronic charge, the magnitude of the charge is less important than its changes. As expected, the electron transfer is always from the iron substrate to the adsorbate. At the low coverage of $\theta = 0.25$ ML it is relatively small for P and S (0.45 e/a and 0.66 e/a), while for O and N it is of the order of one electron per atom (1.00 e/a and 1.12 e/a), see bottom part of Fig. 2.4. These results are consistent with the electronegativity differences between iron and the adsorbates, which in

the Pauling scale is 0.36 in the case of P, 0.75 for S, 1.21 for N and 1.61 for O, indicating an increasing ionicity of the chemisorption bond. It is interesting to notice that the charge transfer decreases with coverage, as can be seen in Fig. 2.5a. Passing from 1/4 ML to full ML coverage, the partial electronic charge on the adatoms decreases consistently for P and S (by 63% and 53%),while for O and N the percentual decreases are smaller (39% and 13%), and the bond ionicity remains high enough to give rise to a significant electrostatic repulsion at distances of the order of one surface lattice constant (2-3 Å) [197, 198]. These different trends can be explained by considering that the increasingly important P-P and S-S interactions is accompanied by a reduction of the electron transfer from the metal to the deposited layer. Conversely, in O and N adsorption, where the adatom-adatom interaction is less relevant, a large charge transfer is also present at high coverage. This transfer gives rise to an electrostatic repulsion among the adatoms which can contribute substantially to the total energy.

The rearrangements of the surface partial charges induced by the adsorption cause a variation of the surface dipole which in turn modifies the work function. The work function calculated for the clean Fe(110) surface, $\phi_0 = 4.87$ eV (as reported in section 2.3.1), is in good agreement with the experimental value of 4.80 eV [200] and with previous DFT calculations [172, 201–203]. It is common practice to relate the change of the work function to the direction and extent of the electronic charge transfer between the adsorbate and the substrate. According to the Langmuir model, successfully used in several adsorption systems [204, 205], a negative charge transfer from the substrate to the adsorbate causes an increase of the work function, while a decrease is found in the case of electron transfer from the adsorbate to substrate. The work function changes, $\Delta\phi = \phi - \phi_0$, due to the adsorption of the considered elements on Fe(1110) are reported in Tab. 2.2, and displayed in Fig. 2.5b. Comparing the changes of $\Delta\phi$ with that of Δq, reported in Fig. 2.5a, it is clear that the work function behavior is more complex than expected according to the Langmuir model. At $\theta = 0.25$ ML, the highest work function change $\Delta\phi$ is induced by P adsorption, even if the partial charge on P is much lower than on N and O. These differences can be partially explained by considering the different adsorption geometry. As shown in Tab. 2.2 the adsorbate-surface vertical distance is $z_A = 0.47$ Å for N and 1.00 Å for O, considerably smaller than the $z_A \sim 1.5$ Å for P and S. Therefore,f the dipoles induced by the adsorbed atoms are screened more efficiently by the metal electrons for N and O than for the other adsorbates [199]. Increasing the coverage to 0.5 ML, the adsorption distances of N and O increase respectively by 35% and 8%, reducing the efficiency of the screening and allowing the work function value to increase. Conversely, z_A of P and S does not change much, preventing significant variations in $\Delta\phi$.

The situation changes significantly at monolayer coverage where N and O show the largest positive variation of the work function, while P and S give negative $\Delta\phi$ values, similar to those due to electropositive adsorbates. The work function stops increasing when the covalent

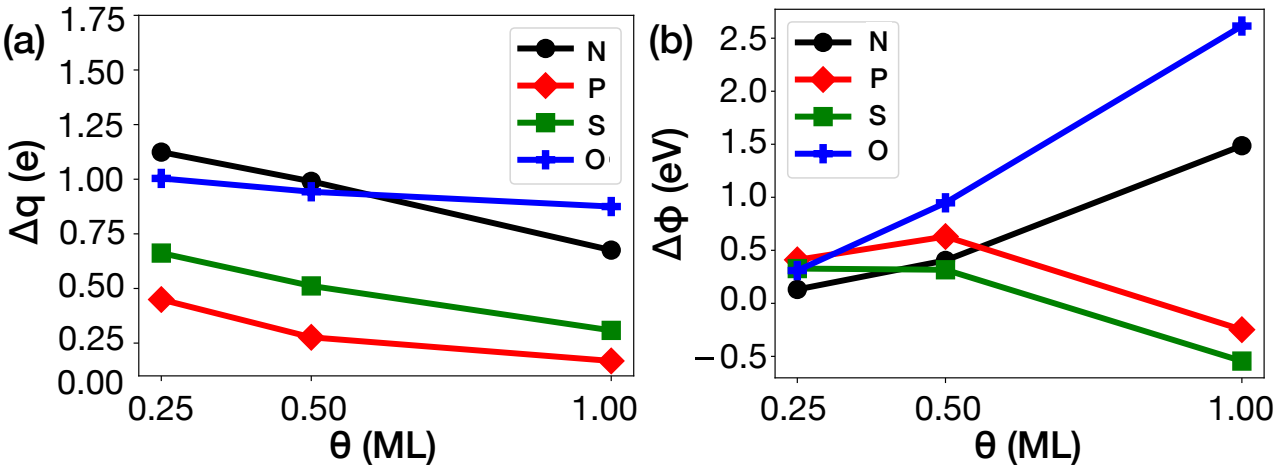

Figure 2.5: Calculated partial charges transferred from the metal surface to the adsorbed atoms at different coverages (a); work function change induced by the chemisorption (b).

interactions between the adsorbates become important. For P this happens at half monolayer where the distance d_{12} between the surface and the first underlayer reaches its maximum value. Indeed, in the P and S cases the variation of $\Delta\phi$ with coverage follows that of d_{12}, which has a maximum at half monolayer. The occurrence of a work function decrease in presence of a negative charge transfer from the substrate to the adsorbate has been found in several cases and explained with simple considerations based on the sign of the charge transfer or the difference in electronegativity [206–209], which are not sufficient to explain the results obtained here. The work function behaviour can be understood only by analyzing the surface dipole that depends both on the details of the charge distribution and the modifications of the atomic positions induced by adsorption. To this purpose we analyzed the charge density displacement induced by the adatom adsorption:

$$\Delta\rho(\mathbf{r}) = \rho_{ads/sur}(\mathbf{r}) - \rho_{ads}(\mathbf{r}) - \rho_{sur}(\mathbf{r}), \tag{2.3}$$

where $\rho_{ads/sur}$ is the charge density of the asdorbate system, ρ_{ads} is the charge density of the isolated adlayer, and ρ_{sur} is the charge density of the clean surface. From this quantity one can define the dipole variation induced by the adsorption as:

$$\Delta p(z) = \int_{z_0}^{z} z\Delta\rho(z)dz, \tag{2.4}$$

where z_0 is the center of the slab. By performing the integration up to half the length of the unit cell one obtains the total induced dipole moment Δp, which is expected to be proportional to the change of the work function $\Delta\phi$, according to the accepted theoretical description [209]

At 1/4 ML the largest change in the electron density distribution occurs in the interface

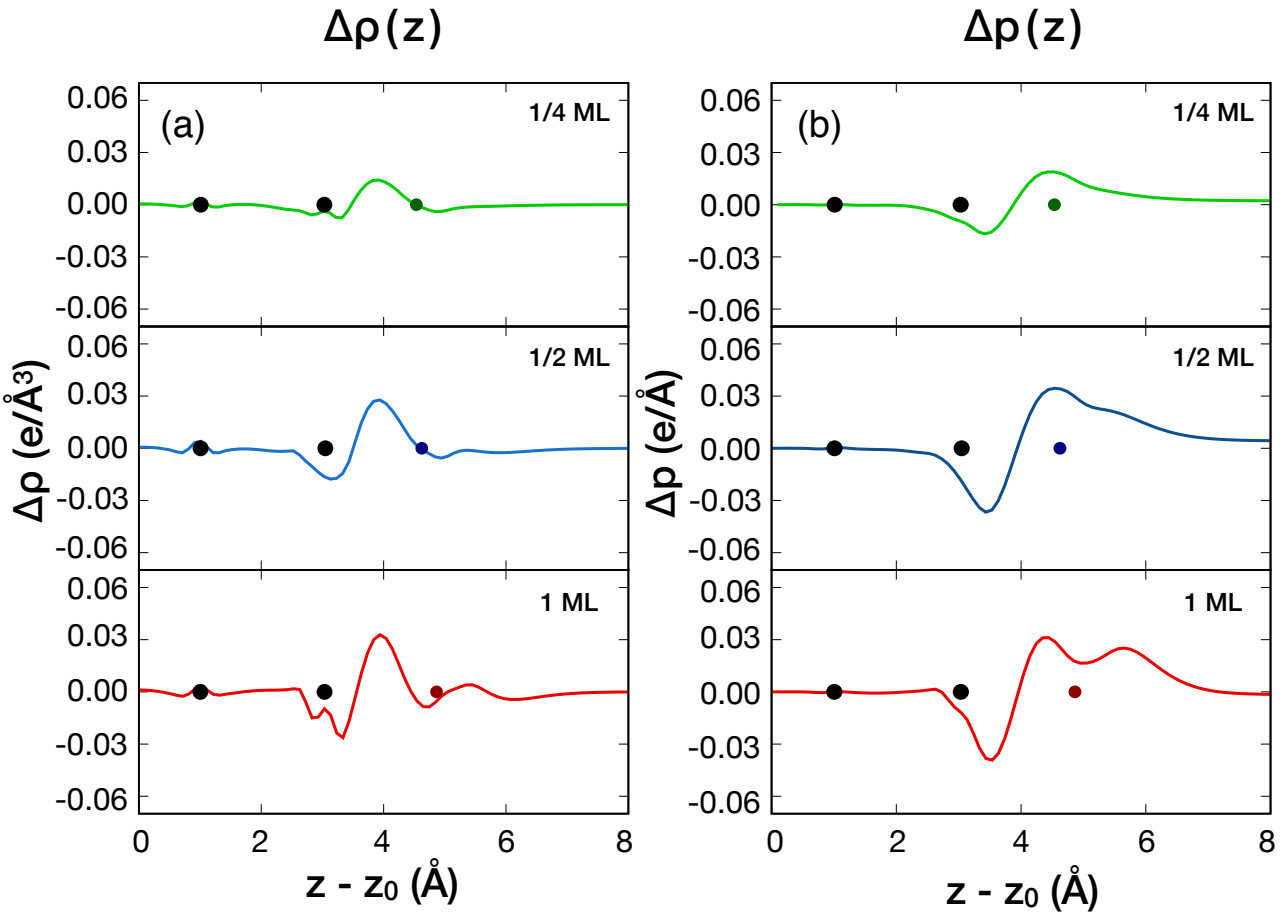

Figure 2.6: (a) Planar average of the charge density displacement induced by P adsorption at different coverage. (b) Corresponding surface dipole modification induced by the adsorption. Colored (black) dots indicate the positions of the adsorbed (iron) layer planes along the surface normal.

between the adsorbed atom and the iron surface, where $\Delta\rho(z)$ shows a maximum slightly closer to the adsorbed layer, while a small charge depletion occurs on the topmost Fe layer and just above the adsorbate. At 1/2 ML the main peak is more pronounced and slightly shifted toward the substrate, while charge on the surface atom is considerably reduced. At 1 ML the main peak is surrounded by two significant density reductions, on the surface and close to the adsorbate, while a charge accumulation is found in the vacuum outside the interface, followed by a further depletion. This complex charge rearrangement causes the dipole variation of Fig. 2.6b. The results obtained by integrating $\Delta p(z)$ up to the middle of the vacuum along z are plotted for all the considered adsorbate systems against the corresponding work function changes $\Delta\phi$ in Fig. 2.7. We obtain the expected linear correlation between Δp and $\Delta\phi$:

$$\Delta\phi = k\Delta p \tag{2.5}$$

with $k = 157.4$. The difference with the value $k = 180.95$ given in Ref. [209] may be imputed to the complex atom rearrangement that we observe in our systems.

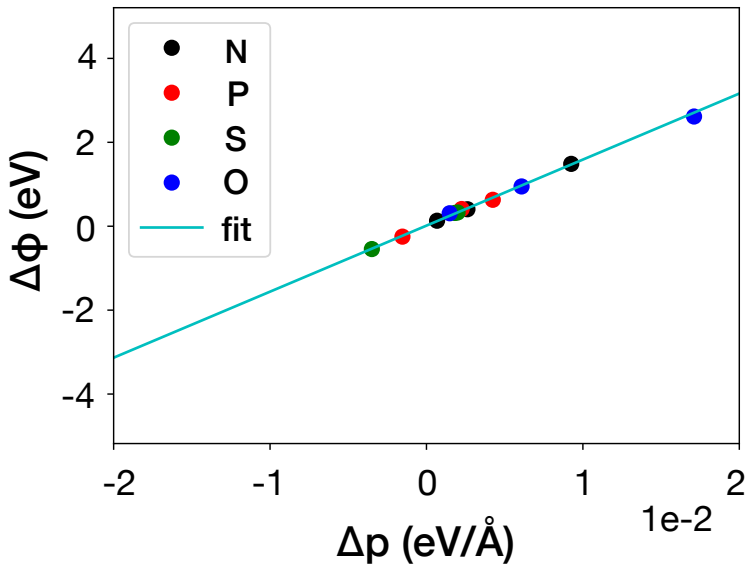

Figure 2.7: Change in the work function versus total adsorption induced dipole moment for all the adsorbates under consideration.

2.3.3 Chemical bonding in P chemisorption

Now the changes in the substrate and adsorbate electronic structure due to adsorption are analyzed. The evolution of the characteristic features of the PDOS with coverage provides a further, clear signature of the P-P covalent bonds that are formed at higher adatom concentra-

tion. Figure 2.8a shows the modifications induced by the adsorption in the PDOS on the 3d, 4s, 4p states of Fe and 3s,3p states of P. DOS's are obtained by summing the spin up and spin down local densities of states. The 0.25 ML (a) and 1 ML (b) coverages are considered.

The P 3s and 3p energy levels for the isolated (2×2) P layer correspond exactly to the isolated atom states, with the 3p level half filled and the 3s state well below E_F, indicating a negligible P-P interaction. After adsorption, the 3s state is split in a lower peak and a continuum band extending around the Fermi level, while the single 3p peak is replaced by a broad band of states, with a larger number of filled states. These modification are entirely due to the P-Fe interaction, as P-P interactions are absent at this low coverage. The shape of the PDOS on the the Fe states reveals a more complex picture than in the Newns-Anderson model, usually adopted as a theoretical explanation of chemisorption at low coverage [210, 211]. We observe the formation of a chemical bond between phosphorus states and iron 3d band. The antibonding states, mainly of d character, produce the structures above E_F, while the bonding states, mainly of 3p character, are located in the range between 2 eV and 5 eV below E_F. The 4sp free electron bands determine the broadening and the shifting of the adsorbed atom levels, while the chemical interaction between the adsorbate levels and the 3d band produces bonding states in the lower part of the d band and antibonding states in the upper part, in agreement with the model [210, 211]. However, the chemisorption effects on the 3d and on the 4sp iron states are of comparable importance: the adsorption causes a drastic reduction of the surface partial DOS near E_F, a significant increase between -2 and -6 eV, and the appearance of a peak around -10 eV.

The analysis of the partial local DOS's of the second iron layer (reported in Figure 2.9) highlights the variation of the electronic structure in the substrate. A significant reduction of the 4sp states contribution above E_F can be noted, with a corresponding increase of the filled states. The 3d states cover an energy range larger than the clean surface, with antibonding structures around 4 eV and bonding structures near the lower edge of the band. This seems to indicate that, even at low coverage, a substantial change in the bonding between the surface and the first sublayer takes place after the adsorption. Figure 2.8b displays the PDOS relative to 1 ML P adsorption. At this coverage, both the P 3s and 3p states show a large broadening extending from -15 eV to 5 eV already in the isolated ML. This clearly points out the existence of a P-P interaction leading to the formation of a P band. The formation of such a band has consequences on the P-Fe interaction. After the adsorption, 3p P states as well as 4sp iron states above E_F significantly reduce, while at the same time the formation of a broad tail of states from -6 eV to -15 eV takes place. Moreover, the width of the central 3d peak reduces while the DOS between -2 eV and -6 eV increases, with significant contributions from 3d iron and 3p phosphorus orbitals. While at low coverage P-Fe interaction is due mainly through their 3p-3d levels, in this case 3s, 3p levels are hybridized by P-P interaction. The bonding is formed

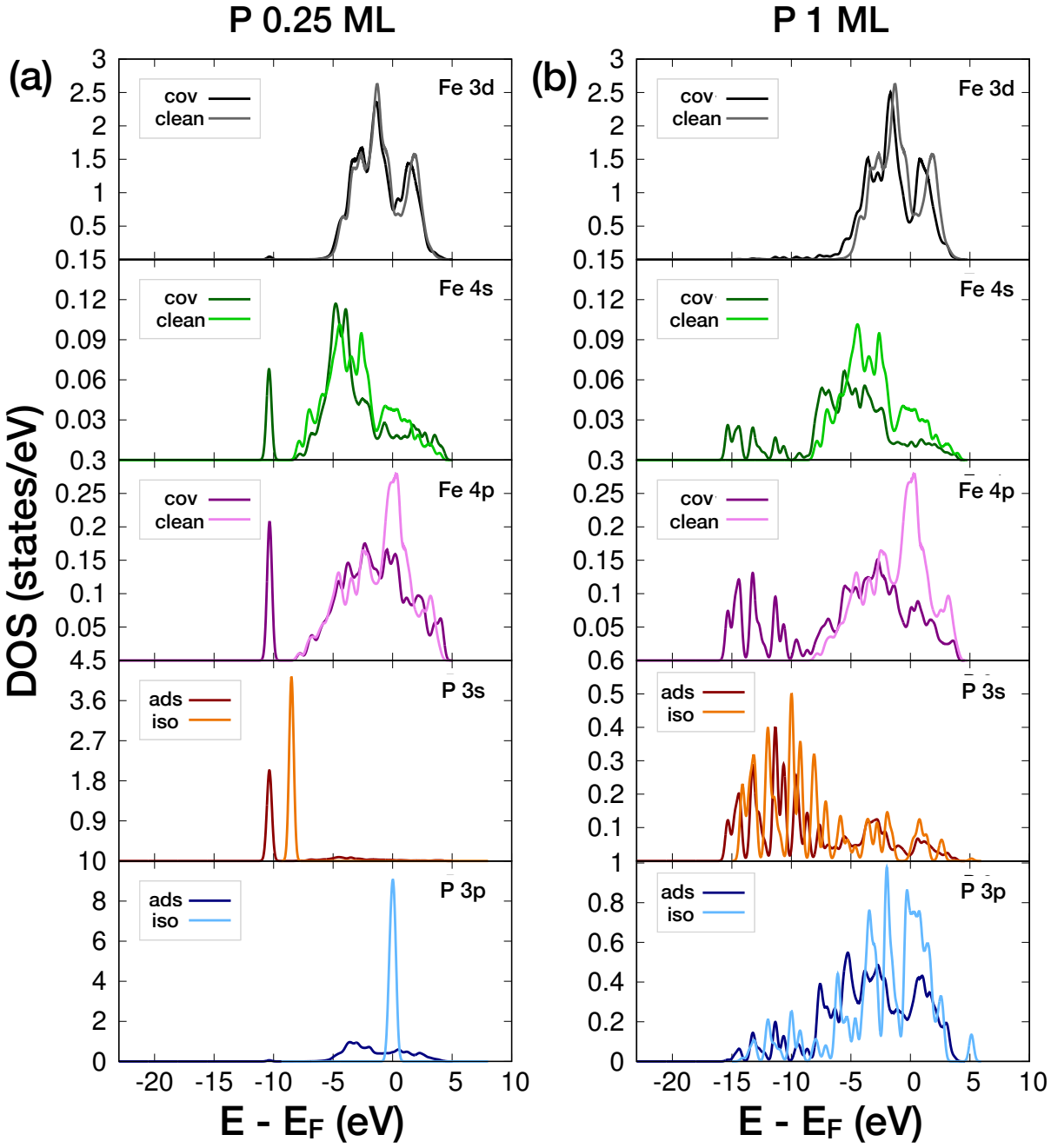

Figure 2.8: Modifications of the PDOS on the valence P and Fe states induced by the adsorption of (2×2) (a) and (1×1) (b) layers of phosphorus. cov: partial local DOS of the covered iron surface; clean: partial local DOS of the clean iron surface; ads: partial local DOS of the adsorbed layer; iso: partial DOS of the isolated layer.

through both the states, and the 4sp band is reshaped accordingly. As a consequence, P-Fe bonds are weakened by the increasing importance of P-P interaction. The partial DOS's of the second layer, reported in Figure 2.10, reveals the significant effects induced by the adsorption in the metal bonding.

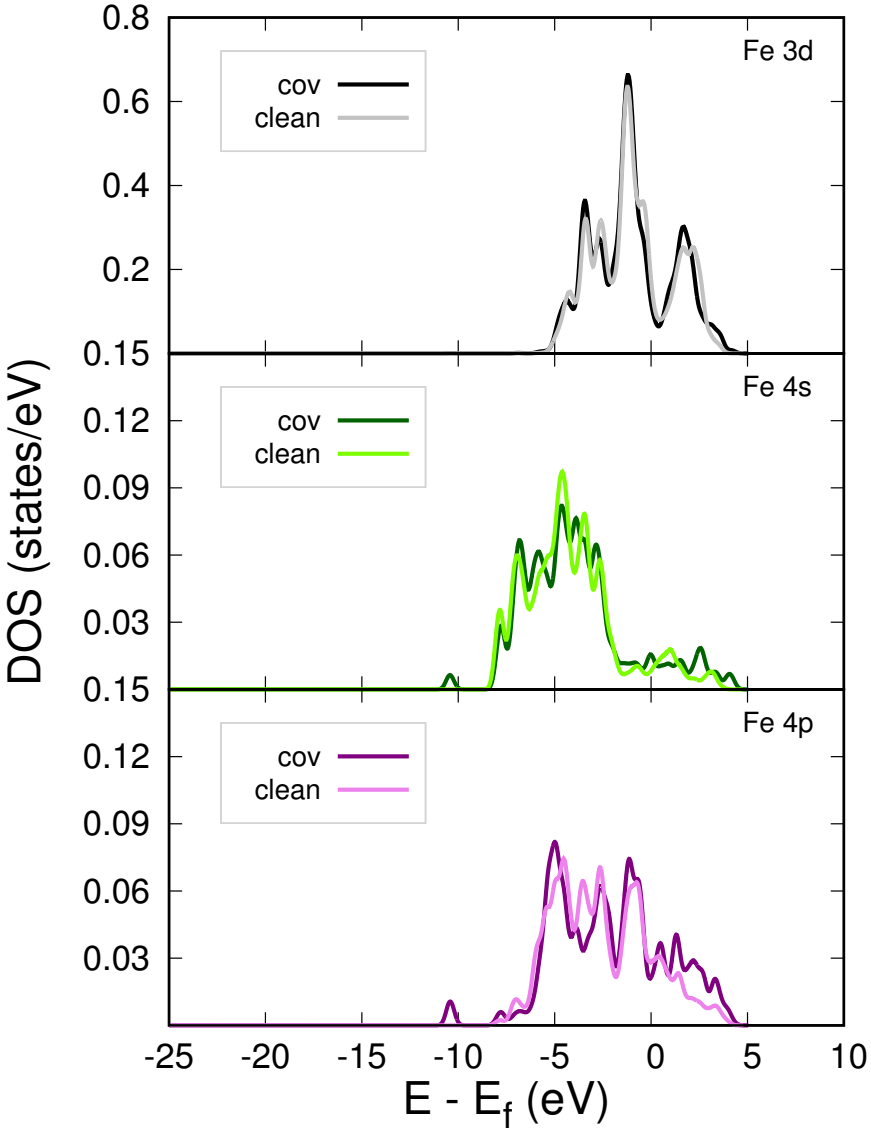

Figure 2.9: PDOS's of the first underlayer iron atoms, at coverage $\theta = 1/4$ ML coverage.

2.4 Conclusions

We study, for the first time to our knowledge, P adsorption on the Fe(110) surface by means of density functional theory calculations. A detailed discussion of the modifications induced by

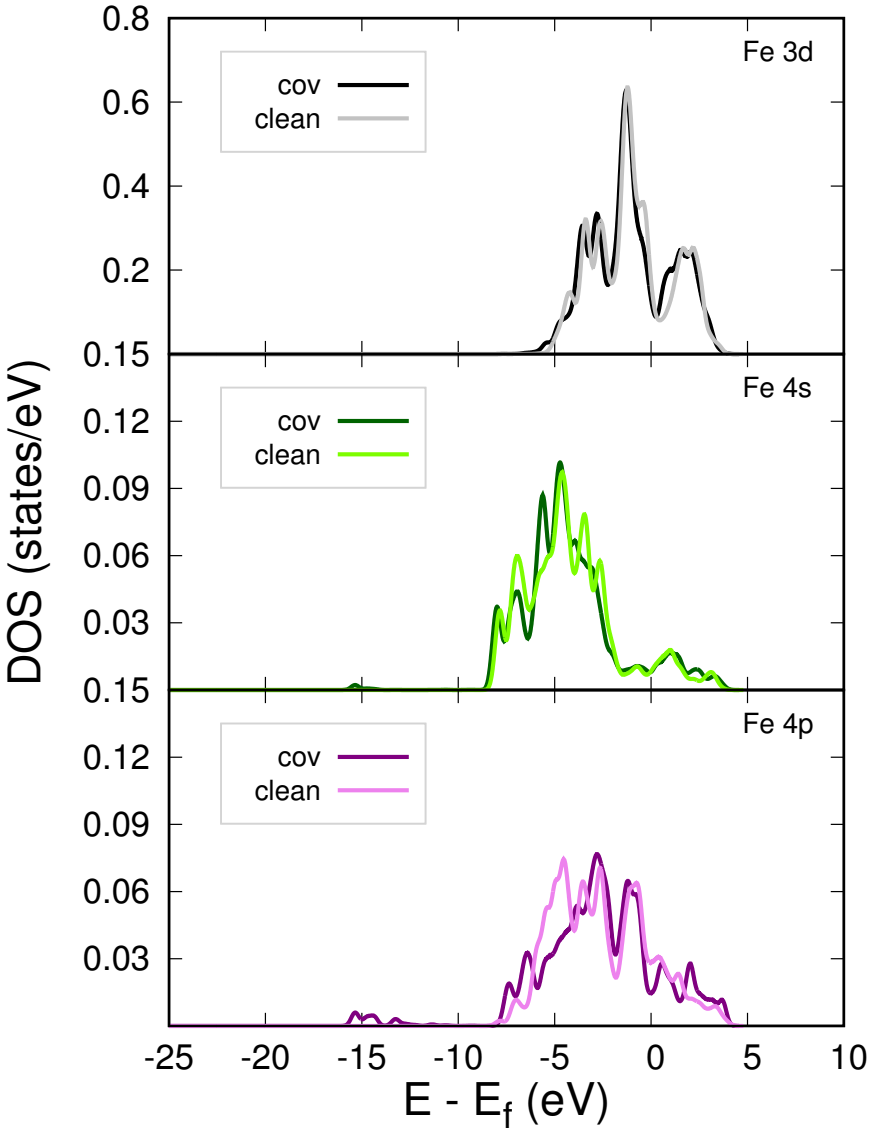

Figure 2.10: PDOS's of the first underlayer iron atoms, at coverage $\theta = 1$ ML coverage..

phosphorus on the substrate electronic and structural properties is provided. A comparative analysis of the chemisorption of P, S, N, and O is also performed as a function of coverage. We find that the most favorable adatom concentration corresponds to 1/4 ML in all the considered cases. However, the decrease in chemisorption energy with coverage has a different origin for the P, S adlayers with respect to the O, N ones, being caused by an increased adatom connectivity in the first case and by electrostatic repulsion in the second case.

The formation of strong chemical bonds among the P (S) adsorbates at high concentration is quantitively described by calculating the adatom-adatom interaction energy and the PDOS. The presence of such interconnected P (S) overlayers is found to cause an anomalous reduction of the metal work function. While a work function reduction in the presence of negatively-charged adsorbates has been observed before, the mechanism responsible for this phenomenon, which is related to changes in interlayer distances, has not been pointed out before.

The formation of a network of covalent P-P (S-S) bonds at high coverage here documented and characterized, is key at understanding the origin of the adhesion and friction reduction observed when P (S)-rich iron tribofilms are formed at sliding steel interfaces [111]. Such understanding may be relevant for preventing iron/steel embrittlement and for designing lubricant additives.

Chapter 3

Friction Reduction on Iron/Iron Interfaces by Elemental Adsorption

3.1 Introduction

[1] To reduce the economic impact of friction (see Introduction), in the last decades an intense research activity has been devoted to the development of novel lubricant materials. These studies have been prompted especially by the discovery of new experimental techniques like Atomic Force Microscopy (AFM) [20] and more in general Scanning Force Microscopy (SFM) [213, 214], which provide single asperity contact, allowing measurements at the nanoscale. These techniques have lead to extraordinary technological advances and to new fundamental understanding of friction at the microscale. However, even by means of the most advanced techniques, most of the essential tribological quantities cannot be directly accessed experimentally, like the interfacial work of adhesion and shear strength, as well as the contact pressure distribution. They can only be inferred using continuum or semi-continuum contact mechanics models, which are known not to hold at the atomic level [87, 88]. An accurate determination of these quantities is nonetheless of fundamental importance, because they govern friction at the atomic scale: the work of adhesion γ determines the energy per unit area needed to separate the paired surfaces, while the ideal interfacial shear strength τ, which corresponds to the static friction force per unit area, represents the ideal maximum resistance to sliding of an interface along a given direction. First-principle density functional theory (DFT) calculations can provide direct and accurate estimates of the interfacial work of adhesion and shear strength. The calculated quantities are *ideal* because they are obtained for undefected interfaces at zero temperature, but their knowledge is nevertheless useful as they set upper limits for the resistance to cleavage and shear stresses of a material, which is relevant both for applications and for general

[1] Topic first discussed in Ref. [212]

understanding of the intrinsic material behavior [103, 120, 121, 125, 215–217]. The starting point for the first principles determination of tribological properties is the construction of the Potential Energy Surface (PES) experienced by a sliding interface. The general method to calculate it is explained in the first chapter, in section 1.3. Previous studies by our group, performed by means of this approach, have shown that, when adsorbed on steel or iron surfaces, phosphorus [119] and especially sulfur [111] remarkably reduce adhesion and ideal shear strength, acting as effective lubricants. Due to their chemical properties, these elements passivate the metal surface and hinder the formation of chemical bonds across the interface. This is in agreement with the embrittlement observed in iron and steel passivated by these elements: the segregation of S and P at the grain boundaries weakens the metal-metal bonds, causing the material failure [157, 162, 163, 165, 166, 168]. Selenium has been shown to behave similarly to P and S when dissolved in iron: it undergoes the same segregation process causing the grain boundaries embrittlement [218–220]. Se is indeed similar in electronic structure to S, as they both belong to the chalcogens group, thus a similar effect on iron/iron interfaces should not be surprising. Despite these similarities, the lubricating effect of selenium on iron/steel has never been studied before, to our knowledge. Here we apply *ab initio* DFT calculations to study the adsorption of Se on the Fe(110) surface, and analyze its effects on the interfacial adhesion and ideal shear strength. The comparison with P and S, as well as with the clean iron surface, in terms of surface electronic properties and their effects on surface passivation and interface tribology, allows us both to emphasize the notable Se properties, and to understand general characteristics that an element should possess to effectively lubricate iron and steel interfaces. Such understanding is relevant for designing new lubricants, such as environmental-friendly additives for engine oils.

3.2 Computational methods

We perform the calculations by means of spin-polarized DFT calculations, using the Quantum ESPRESSO computer package [186]. The exchange-correlation functional is described by the Generalized Gradient Approximation, with the Perdew-Burke-Ernzerhof parametrization (PBE) [187]. The ions are described by ultrasoft pseudopotentials (PP's), with the iron PP including semi-core 3s and 3p states to provide a more accurate description of the electronic structure. The wave functions are expanded in plane waves, with a cut-off of 30 Ry (240 Ry) for the kinetic energy (electron density). These parameters guarantee a good description of bulk iron: the calculated lattice parameter $a = 2.852$ Å, bulk modulus $B = 161$ GPa, and magnetic moment, $M = 2.29\ \mu_B$, are in good agreement with the experimental values [188] of $a_{exp} = 2.867$ Å, $B_{exp} = 170$ GPa, and $M_{exp} = 2.22\ \mu_B$. We model the Fe(110) surface using a

supercell with (2×2) in-plane size and a slab of 5 iron layers. The optimal slab thickness is determined converging the surface energy and the work function, accordingly to the procedure described in detail in Ref. [157]. A 25 Å vacuum region is inserted in the simulation cell to separate the periodic replicas along z. The Brillouin Zone of the supercell is sampled by a $4 \times 4 \times 1$ Monkhorst-Pack grid [189]. The fractional occupancies are calculated using a gaussian broadening, with a smearing width of 0.02 Ry. The adsorption energy per atom E_{ads} is calculated as

$$E_{ads} = (E_{slab+na} - nE_a - E_{slab})/n \tag{3.1}$$

where $E_{slab+na}$ is the total energy of the surface with n adsorbates, E_a is the energy of the isolated adatom and E_{slab} is the energy of the clean metal surface. A negative adsorption energy is energetically favorable.

The interfaces are modeled by mating two iron slabs. Figure 3.1 offers a top-view scheme of the (2×2) cell used to model the Fe(110) surface (in blue) covered by a 1/4 ML of adatoms (in yellow). An identical surface should be imagined sliding on it. To construct the PES, the adhesion energy between the two surfaces is calculated in different relative lateral positions. In particular, the top surface is laterally shifted so that its adsorbed atom is positioned over the high symmetry points of the bottom surface. We consider 5 high symmetry points per (1×1) cell: long bridge (LB), three-fold (TF), short bridge (SB) and on top (OT) site, plus an intermediate (INT) point, positioned between the long bridge and the on top sites. The numbers 1, 2, 3 identify the non equivalent quadrants of the (2×2) supercell. The considered locations sum up to a total number of 13, for symmetry reasons, as the the fourth quadrant is equivalent to the third, as shown in Figure 3.1. For every lateral position i the adhesion energy is computed as $\gamma_i = (E_i^{interface} - 2E_i^{surface})/A$, where A is the planar area of the (2×2) supercell.

In every calculation the external layer in the bottom slab is kept fixed, while the external layer in the top slab and the adsorbed atoms are allowed to relax only in the vertical direction. The adhesion energies computed in the 13 high symmetry points are then replicated in every equivalent site of the orthorhombic (2×2) cell and interpolated according to the procedure described in Ref. [217] to obtain the interfacial PES. The PES is then used to calculate gradients, *i.e.* frictional forces per unit area, along any arbitrary direction α: $\tau_\alpha(x, y) = -\nabla_\alpha \gamma(x, y)$ (as it is done in Fig. 3.7). The ideal interfacial shear strength along α is calculated as: $\tau_\alpha = |\min(\tau_\alpha(x, y))/A|$. The interfacial charge displacement $\Delta\rho(z)$ is calculated as the planar average of the difference between the electronic charge of the interface and the charge of the isolated slabs, where the atoms position are kept in the same configuration as in the interface [31, 103]:

$$\Delta\rho(z) = \frac{1}{A} \int_A (\rho_{interf}(x, y, z) - \rho_{top}(x, y, z) - \rho_{bot}(x, y, z) \mathrm{d}x\mathrm{d}y \tag{3.2}$$

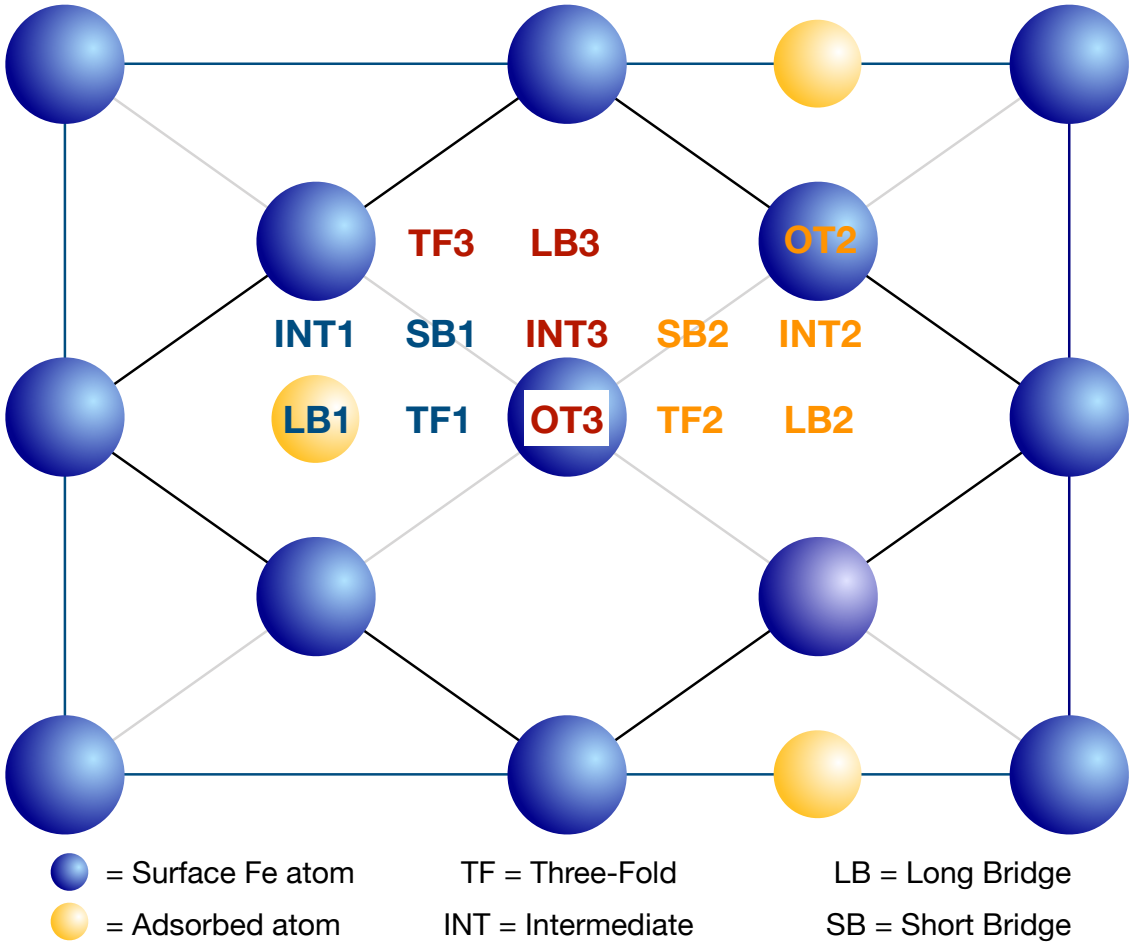

Figure 3.1: High symmetry and their intermediate points in the bcc(110) (2×2) supercell with a 1/4 ML coverage adsorbed layer.

3.3 Results and Discussion

3.3.1 Selenium adsorption on Fe(110) surface

Prior to interface calculations, we study the adsorption of selenium on the Fe(110) surface at different coverage in order to optimize the surface structures to be mated in the interface and understand the nature of the Se-Fe interaction. We consider 1/4, 1/2 and 1 monolayer (ML) coverages. By comparing the Se adsorption energy in the considered high symmetry sites, we identify the 4-fold LB as the most stable configuration at every considered coverage. This result is in agreement with previous studies [221], and common to other elements such as sulfur, phosphorus, oxygen and nitrogen.[157, 173, 175, 181]

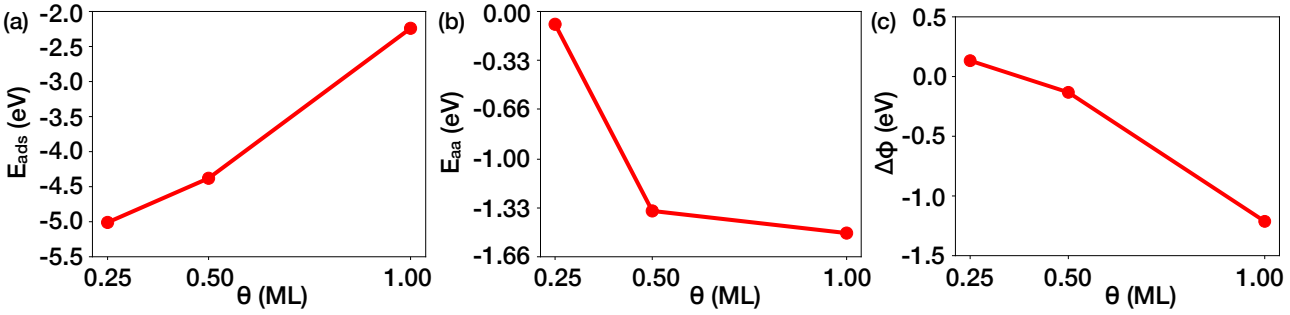

Figure 3.2: Calculated (a) adsorption energy per atom; (b) Se-Se interaction in the isolated layer with the same geometry as the deposited layer; (c) Se induced work function change with respect to the clean surface, as a function of coverage.

Figure 3.2a shows that the adsorption energy calculated in the LB site decreases in absolute value with the coverage, coherently with what we have seen in chapter 2.3. This reduction is mainly due to the increase of the adatom-adatom interaction inside the layer E_{aa}, calculated as: $E_{aa} = \big(E_L - nE_a\big)/n$ [157]. As for the adsorption energy, a negative value means an attractive interaction that stabilizes the layer with respect to the isolated atoms. Here E_L is the energy of an isolated layer of Se atoms with the same spatial configuration as the adsorbed one. This Se-Se attraction increases with coverage (Fig. 3.2b), indicating that at large coverage the interaction among adsorbates becomes stronger, while the adsorption becomes weaker. This suggests that Se-Se intralayer interaction becomes dominant over the surface-adsorbates interaction as the coverage increases. This mechanism results in a screening of the metal substrate. It can be revealed analyzing the work function change induced by the adsorption, given by the relation $\Delta\phi = \phi - \phi_0$, where ϕ (ϕ_0) is the work function of the covered (clean) surface. The work function change is proportional to the surface dipole [199, 206–209] through the relation: $\Delta\phi = k\Delta p$, where k is a proportional factor. $\Delta\phi$ as a function of coverage is shown in Figure 3.2c. At 1/4 ML coverage, $\Delta\phi$ is slightly positive, while it becomes negative at 1/2 and especially at 1 ML, which indicates an inversion also in the sign of the surface

dipole change. The increasing adsorbate coverage modifies the charge transferred across the surface/layer interface. In a previous work we found that $\Delta\phi$ increases with coverage, if the adsorbates do not bind together strongly [157]. Contrariwise, if the adsorbates can bind together covalently, the charge transferred to the adsorbed layer reduces, per atom, with coverage. This causes a work function drop and explains the weakening of the surface-layer interaction. In particular, we can see that $\Delta\phi$ becomes negative already at 1/2 ML, whereas an analogous decrease occurs only at 1 ML with P and S adsorption [157, 173]. This behavior has important consequences on the tribological properties, as we shall see in the following sections. Finally it should be considered that Se atomic radius is larger than P and S. This causes a larger steric hindrance and a more significant Pauli repulsion among the adsorbates at high coverage, that renders the full Se ML unstable, with half of the atoms detaching from the iron surface. Consequently, the calculation at 1 ML coverage is performed at fixed atomic positions. This finding is consistent with the experimental observation that Se saturation at grain boundaries occurs at half ML [218, 220].

3.3.2 Interfacial adhesion and electronic structure

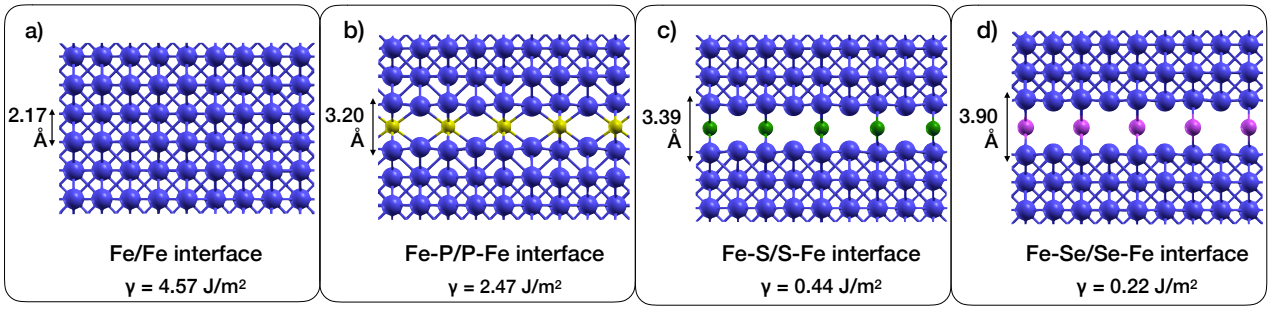

Figure 3.3: (a) Fe/Fe, (b) Fe-P/P-Fe, (c) Fe-S/S-Fe, (d) Fe-Se/Se-Fe interfaces. The snapshots show a side view of the geometrically optimized configuration of the interfaces at the equilibrium separation, with the adatoms positioned in the LB1 and LB2 adsorption sites defined in Fig. 3.1.

Interfacial adhesion

Selenium-covered surfaces are mated to form an interface, as described in the method section. Each of the two slabs is covered by a 1/4 Se ML, the most favorable coverage. The atom adsorbed onto the bottom (top) surface is located in the LB1 (LB2) position represented in

Figure 3.1. Once the surfaces are paired, the interface geometry is optimized and its lowest energy configuration is found. The relaxed configuration is shown in Figure 3.3: the interfacial adatoms bind to both the facing surfaces, forming a c(2×2) configuration, corresponding to a 1/2 ML coverage on each surface. Figure 3.3 shows, for comparison, the minimum energy configurations of the P- and S-covered interfaces. The amplitude of the separation between the iron surfaces is shown in Table 3.1, together with the adhesion energy. The separation induced by Se atoms (3.9 Å) is larger than that caused by S ($\sim$ 3.4 Å) and P (3.2 Å) atoms. As the interface is widened, the adhesion energy is reduced as well, although not proportionally: P induces a reduction by a factor of 2, while S and Se makes it drop by more than an order of magnitude.

adsorbed species	adhesion energy γ (J/m^2)	interface separation z_{eq} (Å)	PES corrugation $\Delta\gamma$ (J/m^2)	ideal shear strength τ_{MEP} (GPa)
clean	-4.57	2.02	1.74	10.19
P	-2.47	3.20	1.35	5.48
S	-0.44	3.39	0.46	3.68
Se	-0.22	3.90	0.13	1.13

Table 3.1: Adhesion energies, surface-surface distances, PES corrugation and ideal shear strength of the various covered interface elements covering the iron surfaces. The adhesion energies and the surface-surface distances are referred to the minimum configuration, shown in Fig.3.3

The effect of the adsorbates on the surface-surface interaction can be clearly seen by looking at the Perpendicular Energy Profiles (PEP) reported in Figure 3.4. The PEP is obtained calculating the adhesion energy between the paired surfaces at different, fixed distances (dots in Figure 3.4), and interpolating the curve with splines (solid lines). The curves display immediately the effectiveness of the additives: the depth of the minimum decreases from the clean interface to the Se-intercalated interface, where it is almost vanishing.

Density of States

The remarkable adhesion reduction can be explained by considering the modifications of the electronic properties induced by the adsorption. We have seen in the discussion of the adsorption properties, that at 1/4 ML the covalent bonds inside the layer are almost absent, while at 1/2 ML coverage they start to weaken the surface-layer interaction [157, 173, 221].

The Density of States (DOS) of the clean iron interface is compared with the passivated interfaces (Figure 3.5). The energies are referred to the Fermi level E_f. The iron 3d level is located between -9 and 3 eV. Its structure is modified most significantly between -9 and -5 eV, as shown on the right side in the zoomed panel of Figure 3.5. The DOS modifications induced

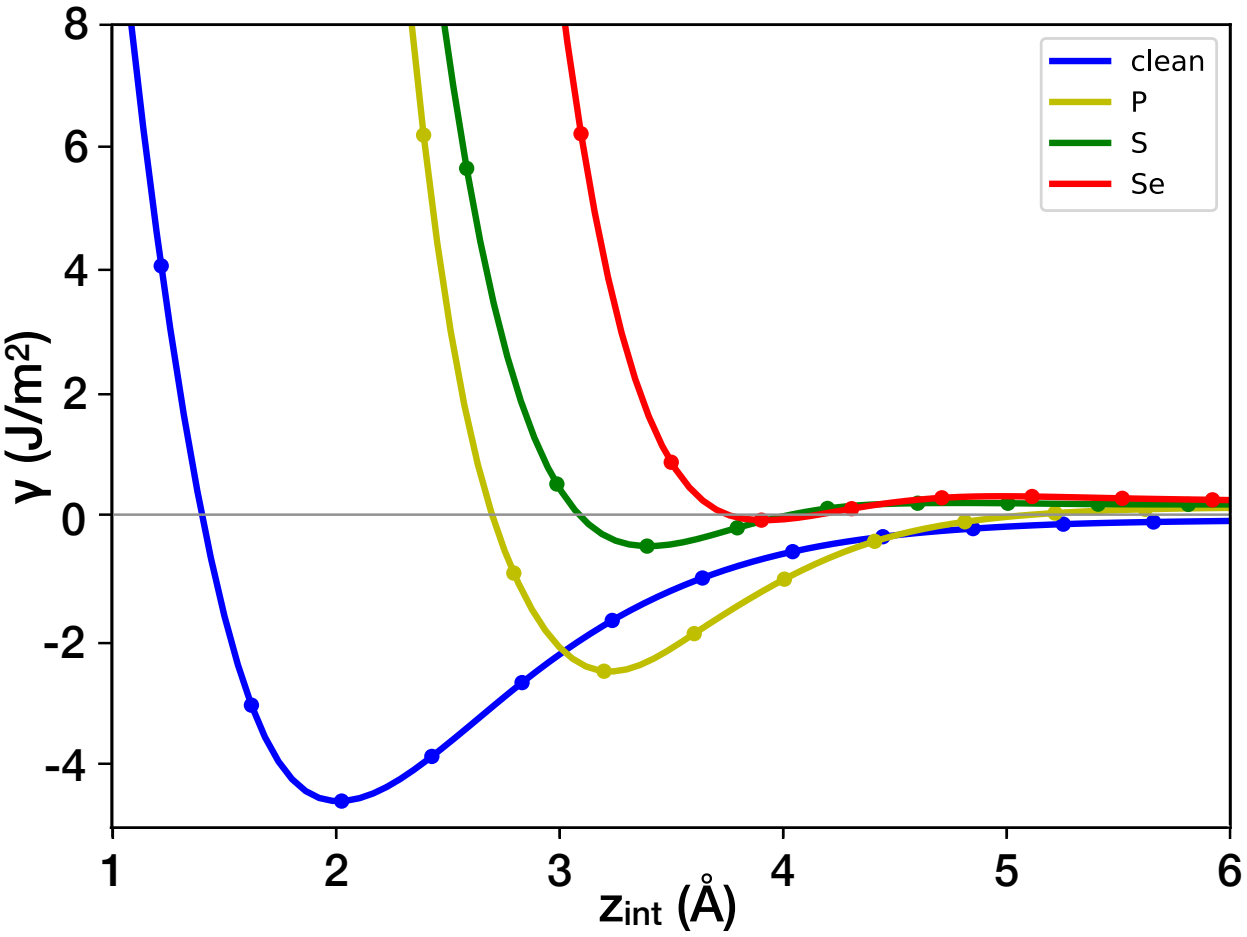

Figure 3.4: Interaction energy as a function of the surface separation. The dots represent the energies calculated from first principles, while the continuum line is obtained interpolating with splines.

in this energy interval are due to the interaction between Se (P, S) 4p (3p) level and the iron 3d band, contributing to the layer-surfaces interaction, as it has been thoroughly shown in previous works [157, 173, 221]. We note that the modification induced by S and Se atoms is almost overlapped, coherently with their similar valence structure.

Another significant modification can be observed for energies lower than -10 eV (bottom panel of Figure 3.5), where broad bands corresponding to Se (P, S) 4s (3s) level are visible. The bands broadening can be entirely attributed to the adatom-adatom interaction, as there are strong evidences in literature that the distribution of the s level is not modified by the interaction with the metal surface [157, 173, 221]. This is also in complete agreement with what we have shown here about Se adsorption. We have observed that the intralayer interactions increase with the coverage, with a consequent weakening of the surface/layer interaction. This provides a first insight into the influence of the interface chemistry on the tribological behavior. In particular, we observe a major difference between phosphorus s level on one hand and S, Se on the other. P 3s band is broader and much closer in energy to E_f than Se and S ones, whose s levels are almost overlapped. This is consistent with the observation that S and Se have a similar valence structure. More importantly, this suggests that the large difference in the adhesion of the Fe-P/P-Fe interface on one hand and Fe-Se/Se-Fe and Fe-S/S-Fe interfaces on the other should be mainly attributed to the chemical bonds across the interface. The slightly more consistent reduction caused by Se can be attributed to its larger steric hindrance and thus to the wider Se-induced interface separation.

Charge displacement across the interface

To obtain additional insights into the electronic properties relevant to the adhesion, we analyze the charge displacement occurring when the interface is formed from the two separated surfaces. Indeed it has been shown that there is a direct correlation between the charge that is accumulated between two mating surfaces and their adhesion [31]. The planar average of the charge displacements, as defined in the method section, are shown in Figure 3.6 for all the considered interfaces. In the clean iron interface (3.6a), where the adhesion is high (Table 3.1), a consistent charge accumulation is visible at the middle of the interface: the charge originally spilling out the isolated surfaces is transferred from the near-surface regions to the interlayer region to form bulk metallic bonds. The presence of P (3.6b), S (3.6c), and Se (3.6d) adsorbates hinders the charge accumulation inside the interface, with a consequent reduction of the adhesion. The accumulation peaks that appears between the adsorbate layer and each metallic surface are much lower, as well as the charge depletion on the surface iron atoms. This smaller charge rearrangement is consistent with the weaker interaction between the passivated surfaces. Moreover, the electronic charge is depleted around the adsorbed layer, which is again

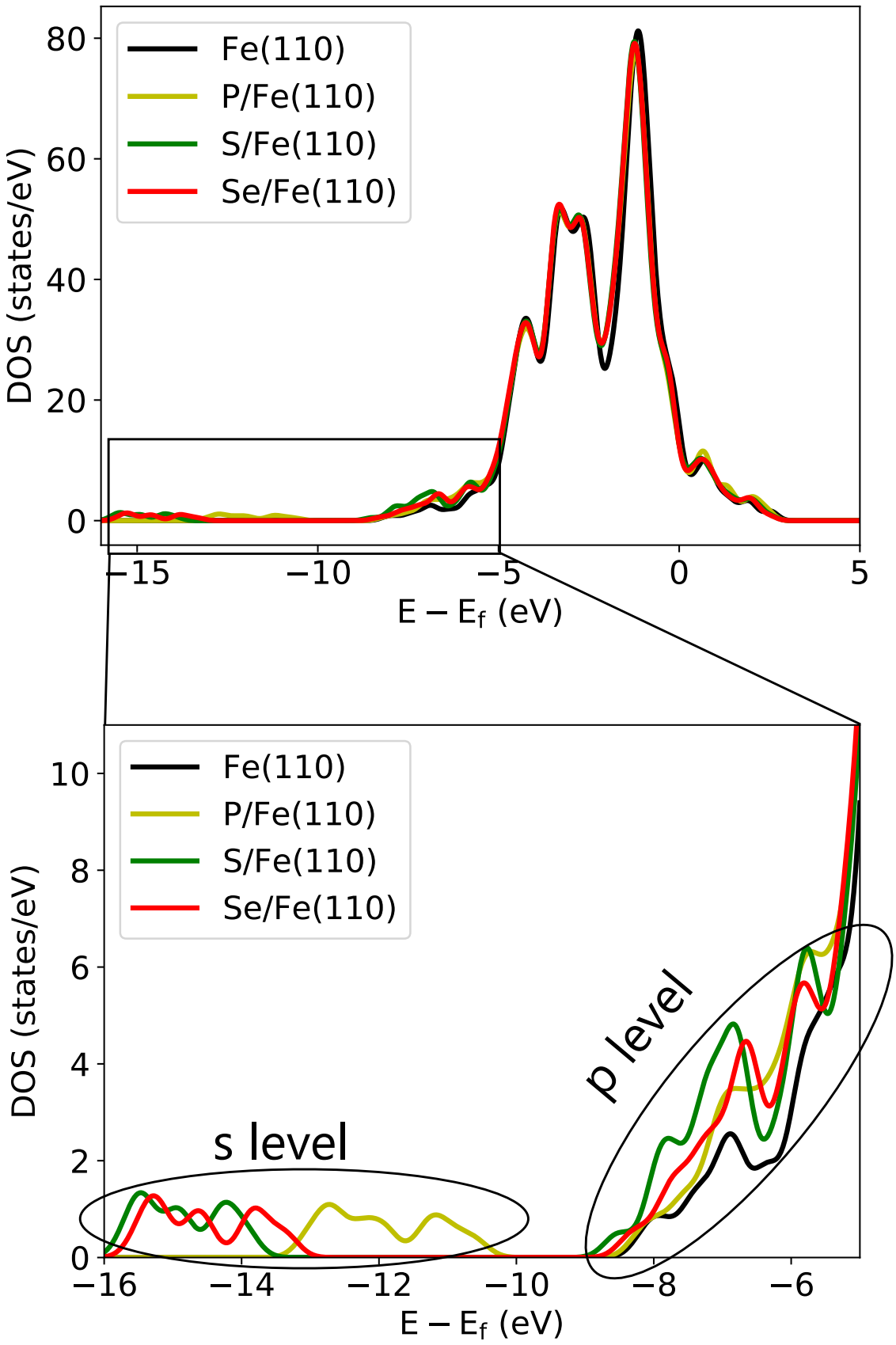

Figure 3.5: Comparison among the total DOS's of the iron/iron interface, clean and with different additives. The bottom panel shows a zoom between -16 and -5 eV, to highlight the modifications induced by the valence electrons of the adsorbed atoms.

consistent with the formation of an adatom-adatom covalent-like interaction that screens the the metal-metal interaction: the electrons are shared among the atoms of the adsorbed layer, preventing the charge transfer from the metal to the additives. Thus, passing from 1/4 to 1/2 ML the charge transferred per atom decreases, which results in a net charge depletion.

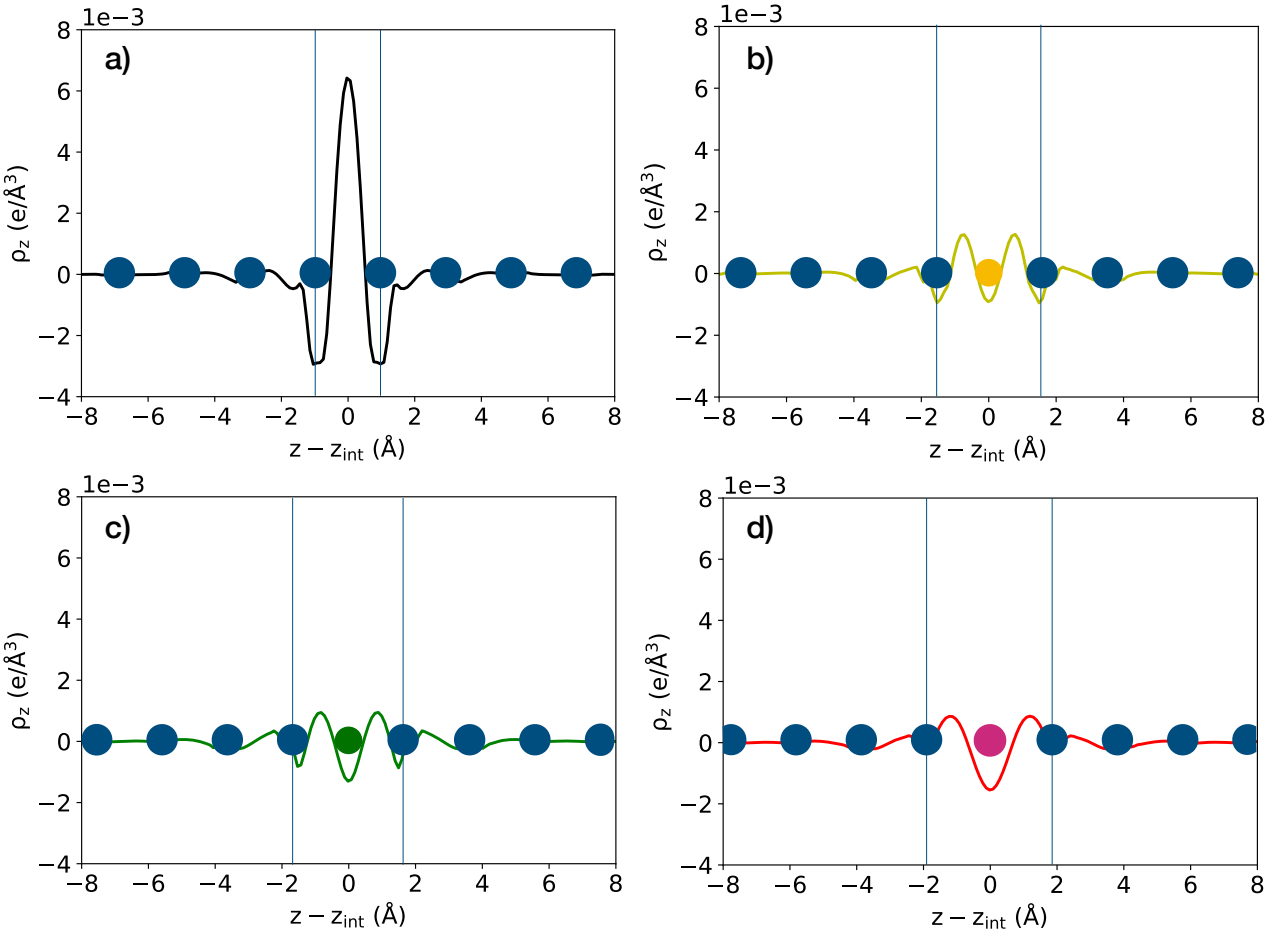

Figure 3.6: Planar average charge of the charge displacement for the (a) clean Fe/Fe interface, (b) Fe-P/P-Fe, (c) Fe-S/S-Fe, (d) Fe-Se/Se-Fe interfaces. Blue circles indicate the iron planes along the interface normal, while yellow, red and pink circles represent respectively the P, S and Se adsorbate layers.

3.3.3 Effects of selenium on iron tribological properties

To fully characterize the adhesive friction of an interface, the knowledge of the adhesion energy is not enough. What determines the frictional forces is, in fact, the variation of the adhesion energy as a function of the relative lateral position of the two surfaces in contact. We, thus, compute the PES according to the procedure described in the Methods section. The PES corrugation corresponds to the highest energy barrier that can be encountered during sliding,

and the derivative of the PES profile along a specific direction gives the intensity of the frictional forces appearing during sliding along that direction. The results are shown in Figure 3.7. It appears immediately evident that the additives reduce significantly the PES corrugation, $\Delta\gamma = \gamma_{max} - \gamma_{min}$, as indicated in each plot. In particular, the Se passivation makes the PES become almost flat: the corrugation $\Delta\gamma_{Se}$ being more than one order of magnitude lower than $\Delta\gamma_{Fe}$ and $\Delta\gamma_P$ and three times lower than $\Delta\gamma_S$. Even though surfaces in relative motion are unlikely to pass through the energy maxima, the PES corrugation is nonetheless a significant figure of merit because it gives a quantitative estimate of the maximum amount of energy that can be dissipated during sliding.

The path with the highest statistical weight is the minimum energy path (MEP), where the sliding barrier is the lowest. We calculate the MEP by means of the improved zero temperature string method algorithm [222, 223], already employed successfully by our group in the systematic study of homogeneous interfaces [217]. The calculated MEP's are represented by yellow lines on the PES's of Figure 3.7. The discontinuities in the Fe-Se/Se-Fe MEP are due to the very low corrugation, which causes some interpolation errors. From the MEP gradient it is possible to obtain the force acting along the MEP during sliding and we consider the most negative value, which represent the maximum resistance to sliding, as representative of the ideal interfacial shear strength [120]. The computed values are reported in Table 3.1.

We find that all the considered adsorbates reduce considerably the ideal shear strength at the interface.[2] Indeed both S and P are key elements for anti-wear, extreme-pressure additives in engine oils. Gas phase lubrication experiments combined with in-situ spectroscopic analysis have shown that organo-sulfur (phosphorus) additives can effectively lubricate steel-on-steel contacts by forming iron-sulphide (phosphide) tribofilms. First principles calculations, where iron interfaces containing S (P) atoms are used to model the tribofilm, are thus representative of the real situation. It is interesting to notice that first principles calculations are not only able to predict the lubricating effect of the tribofilms, but also to indicate that iron-sulphide is more effective than iron-phosphide in reducing friction, as observed in the experiments [111]. This means that the chemical interactions at nano-asperity contacts govern the frictional behavior of the system at the macroscale, and first principles calculations are very powerful investigation tools as they can describe such chemical interactions very accurately.

Here we predict that Se reduces the ideal shear strength much more effectively than S and P, with nearly one order of magnitude reduction with respect to the clean iron. This improvement is striking, being very close to the reduction induced by graphene [103], which is well known

[2]The values slightly larger but consistent with previous findings in literature [111]. This is probably due to the different number of iron layers here considered in the iron slabs, 5 against 3, and to the higher number of high symmetry points used here for interpolating the PES's: we consider also the three-fold and the intermediate points, that allow us to provide a more accurate evaluation of the PES and of the MEP.

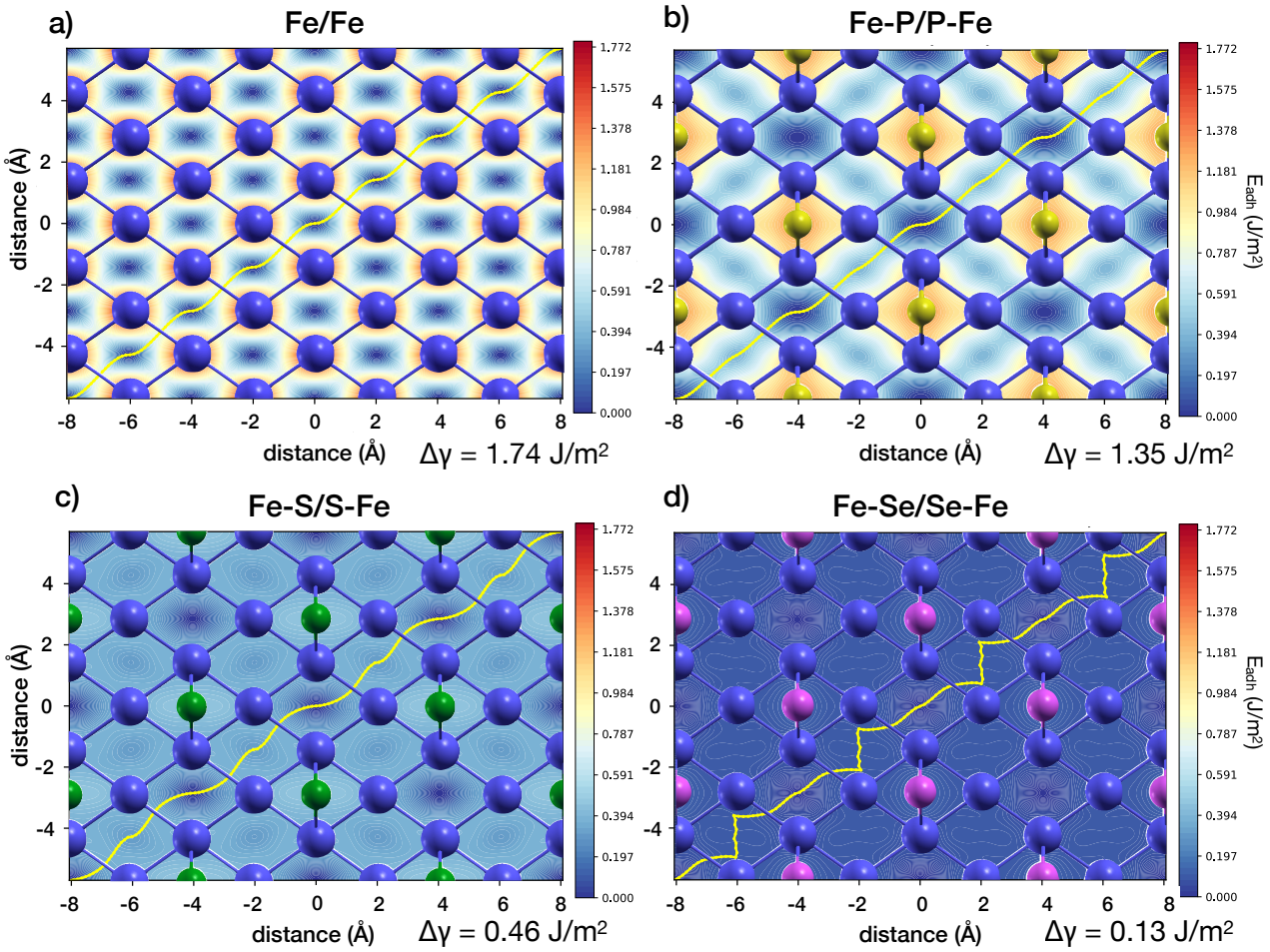

Figure 3.7: Calculated PES's for (a) the clean iron interface, (b-d) passivated interfaces. The work of adhesion is indicated by a common scale ranging from the absolute minimum of the Fe interface, which is set to zero and colored in blue, to the maximum corrugation in red, which again is observed in the clean interface. The corrugation of each PES is indicated on the bottom right of every figure. The yellow lines identify the calculated minimum energy paths.

for its remarkable lubricant propertie [224, 225]. This findings suggest Se as promising element for lubricant materials used for friction reduction in iron or steel contacts.

3.4 Conclusions

We perform a first principles study of the effects of selenium on the adhesive friction of iron interfaces. In the first place Se adsorption as a function of coverage is analyzed. We find a decrease of the adsorption energy and a drop of the work function. This behavior is related to the formation of covalent interactions among the Se atoms of the adsorbed layer as the coverage increases. These interactions weaken the surface-adsorbates binding, as found also for P and S [157, 173]. We, then, present a detailed analysis of the electronic properties of iron interfaces containing Se atoms and compare to those containing P and S elements, as well as to the clean iron surface. We find that the Se adsorbate screens the interaction between the paired metal surfaces, reducing the adhesion energy, similarly but more effectively than S and P. This is accompanied by a friction reduction, as revealed by the calculated potential energy surface that present very low energy barriers along every sliding direction, especially along the minimum energy path. The ideal interfacial shear strength is reduced tenfold with respect to the clean iron surface. A comparison with phosphorus and sulfur, which also segregate at iron grain boundaries [162, 163, 165, 166, 168, 218–220], reveals that Se is able to reduce the interfacial shear strength more effectively (by three times) than P and S. This suggest that Se-based lubricants may have superior properties as lubricant materials for iron and steel. We propose a model explaining how metal passivation can result in interface lubrication: when the adsorbates are able to form covalent bonds among each other, the formation of inert layer on the mating surfaces is key to weaken the metal-metal interaction, preventing the formation of chemical bonds across the interface and leading to a significant friction reduction.

Moreover, the results concerning Se suggest that lubricant additives able to form an iron-selenide tribofilm could be very effective in reducing friction.

Part II

Tribochemical conversion of hydrocarbons to carbon nanocoatings

Chapter 4

Tribochemical conversion of methane to graphene on sliding interfaces

4.1 Introduction

Tribochemical reaction films, known in literature as tribofilms, are very typical of all interacting surfaces that are in relative motion [226], as we have seen in chapter 1. These films commonly result from a chemical or catalytic response of sliding surface to the reactive gases or liquids present at sliding contact interface [45]. One of the most notable examples is the formation of a phosphate tribofilm as a result of tribochemical reactions occurring between sliding surfaces and ZDDP additive in engine oils [52], which is extremely important for long life or reliability of the components. Likewise, a dramatic reduction of friction (i.e., from 0.6 to 0.003) in ta-C and CN_x type carbon coatings in hydrogen environment is due to a tribochemical reaction between surface carbon atoms and hydrogen creating a fully hydrogen terminated or passivated top surface layer that diminishes adhesion and hence friction during sliding [4]. Overall, the making and breaking of such tribofilms dominate friction and wear, influencing the durability and frictional performance of all moving mechanical systems.

Besides these liquid and gaseous species, all kinds of solid lubricants are available [227, 228] for controlling friction and wear. In addition to the traditional graphite, molybdenum disulfide, and boron nitride, many researchers have confirmed that low-dimensional nanomaterials like fullerenes [229], graphene [230, 231], nanotubes [232], and nano-onions, are also very effective in reducing friction and wear [233]. One major drawback is that mainly because of their finite thickness or volume, these solids films eventually tend to wear out, and thus high friction and wear prevail again.

Here we report tribochemical conversion of methane (CH_4) to graphene, nano-onion, and disordered carbons on sliding surfaces of VN-containing Ni coating under atmospheric pressure

and at room temperature. We show that these catalytically active coatings enable in-operando extraction of graphene and other carbon nanostructures continuously from CH_4 and thus providing extraordinary protection against wear and lowering friction. Although there are not many moving mechanical assemblies that operate in CH_4, it is a major constituent of natural gas for power generation and fueling in transportation systems. There many moving parts operate in natural gas, including pistons and seal packs of reciprocating natural gas compressors in pipelines, refueling stations, and the fuel injectors of natural gas powered engines [234]. Therefore, the results of our study are not only scientifically significant but also have the capacity of positively influencing these fields by leading to more efficient, durable, and cost-effective industrial practices. In particular, enabling hydrocarbon molecules of natural gas to provide a composite carbon tribolayer on a self-replenishing or self-healing manner is very attractive.

4.2 Materials and Methods

Test materials[1] used in this study included coated steel balls rubbing against coated flats made from AISI 52100-grade through-hardened ball bearing steel (nominal hardness, 58-62 Rockwell C). Prior to the deposition of Ni-containing VN coating, Ar-sputter ion etching is conducted to remove the surface contaminants. Subsequently, a V bonding layer (120 nm thick) was deposited first on the steel substrate, using a dual magnetron sputtering system. The nanocomposite coatings were deposited from high-purity targets (V 99.95%, Ni 99.99%). For example, to prepare the VN-Ni nanocomposite coatings containing $\sim$ 9.5% (atomic percentage) of nickel, 4,000 W (9 W/cm^2) and 225 W (5.1 W/cm^2) were applied on V and Ni targets, respectively. The substrate temperature was kept constant at 325 $\circ$C. The total working pressure was fixed at 0.4 Pa in a mixture of Ar/N_2 (120 sccm/80 sccm, respectively). As the next step, a crystallographic phase analysis was performed of the composite coatings (about 1 μm thick) using an X-ray diffractometer (Bruker D2 Phaser) that uses the monochromatized Cu K_α radiation. The hardness and elastic modulus of the coatings were measured by a nano-indenter (Hysitron Triboindenter TI-950) with a Berkovich diamond probe. Different loads (0.5 mN to 12 mN) were used to evaluate the hardness/elastic modulus as a function of the penetration (hc) in order to avoid the influence of the substrate mechanical properties. The Oliver-Pharr [235] method was used to calculate the hardness and the elastic modulus of the coatings. The surface roughness of the as-received and coated surfaces was measured by a Bruker Contour GT white light 3D profilometer.

Sliding experiments were carried out with a high-vacuum tribometer using a ball-on-disk setup, in which a stationary steel ball (9.5 mm in diameter) was pressed against a rotating

[1]The experimental tests were performed by the group of Dr. Erdemir at Argonne National Laboratory

disc (50.8 mm and 6.35 mm thick) under mean Hertz pressures of $\sim 0.6\,\mathrm{GPa}$. Both coated and uncoated balls were tested against the coated/uncoated steel flats in the presence of atmospheric pressure methane at room temperature. The sliding contact surfaces of ball and flat specimens had a nominal surface roughness of $0.02\,\mu\mathrm{m}$ RMS. Prior to the tribological tests, all test samples were cleaned by acetone and isopropanol solvents in an ultrasonic bath for 5 minutes. The pure methane gas was bled into the vacuum chamber after evacuating it down to 10^{-4} Pa levels until reaching 0.9 atm ($\sim 91\,\mathrm{MPa}$). The experiment was carried out at room temperature. The normal load on top of the stationary ball was 2 N (which would create a peak Hertz pressure of $\sim 0.6\,\mathrm{GPa}$), and the sliding speed was 0.1 m/s, so that the rubbing surfaces would have been under severe contact conditions at all times. The total sliding distance accumulated during the tests was 360 m. The friction force generated between the sliding ball and flat surfaces was continuously monitored and recorded throughout the tests using a data acquisition system and later converted to the friction coefficients for the entire test cycle. The wear volumes on the ball and disk samples were assessed with the help of optical microscopy; specifically, the wear scars and tracks were imaged by an Olympus STM6 microscope. The amount of wear was calculated by using the standard wear volume equations based on the wear scar diameter measured by the microscope. The tribofilms were analyzed by confocal Raman microscopy (inVia Reflex, Renishaw, Inc.) using appropriate light sources with a wavelength of 633 nm to determine the nature of the tribo-chemical films that formed on the rubbing surfaces during sliding. The Raman instrument was calibrated with an internal silicon reference, and the spectra were recorded in the range of $1000 - 2000\,\mathrm{cm}^{-1}$. Highly oriented pyrolytic graphite (Ted Pella, lacey carbon) was used as a reference.

Density functional theory calculations were performed within the generalized gradient approximation in the Perdew-Burke-Ernzerhof parametrization [187]. The ionic species were described by ultrasoft pseudopotentials, and the electronic wavefunctions expanded in plane waves [186]. A kinetic energy cutoff of 25 Ry (200 Ry) was used to truncate the expansion of the wavefunctions (charge density) on the basis of test calculations on the bulk properties of the considered materials. The static calculations were performed by means of periodic supercells containing a vacuum region 15 Å thick and a slab with (2×2) in-plane size and three-layers thickness. The in-plane size of the cell was increased to a $(4 \times 3\sqrt{3})$ cell, corresponding to 24 atoms per layer, in dynamic calculations. Although nickel is known to be ferromagnetic, we did not consider the spin polarization to avoid a dramatic increase of the computational workload of the ab initio molecular dynamics simulations, where the reaction paths are mainly governed by the mechanical stresses applied. This computational choice is also justified by previous works on C/CH_x chemisorption and CH_4 dehydrogenation on Ni [236–238].

Ab initio molecular dynamics simulations were carried out in the Born-Oppenheimer scheme using a home-modified version of the program included in the Quantum Espresso package [186]

that allows the user to simulate tribological conditions. In particular, a constant load and a constant relative velocity of the two surfaces have been modeled. We control the temperature of the two sliding slabs (excluding the translational motion), while leaving the temperature of the intercalated molecules free to evolve.

4.3 Results

4.3.1 Friction and Wear Performance

Details of the coating deposition procedure, structural, chemical and mechanical characterization of resultant coatings, as well as the tribological test methodology and conditions are provided in the appendix section A of this chapter (see Figures A.1-A.3). Under the test configuration illustrated in Figure 4.1a, the friction coefficient of a steel ball sliding against the steel flat in CH_4 goes up very quickly to a value of 1.2 and remains relatively constant until the end of the two hour long test (Figure 4.1b). When the same test is repeated with a VN-Ni coated test pair, the friction coefficient is reduced by nearly 50%. More remarkably, the wear volume loss on the coated ball side is reduced by more than two orders of magnitude (245 times, see Figs. 4.1b,c), going from $7.7 \times 10^{-12}\,\mathrm{m}^3$ when steel *vs* steel surfaces are tested (Figure 4.1c) down to $3.14 \times 10^{-14}\,\mathrm{m}^3$ for VN-Ni *vs* VN-Ni test case (Figure 4.1d). The wear damage on the uncoated 52100 steel flat is also very extensive, as a very wide and deep wear groove forms. Conversely, the wear damage is hard to discern on the VN-Ni-coated flat side(Figure 4.1e).

4.3.2 Characterization of Sliding Surfaces

Upon close examination of the sliding surfaces of VN-Ni-coated test pairs with a microscope, blackish wear debris particles or patches can be noticed at or near the rubbing surfaces of both the ball and flat surfaces, as highlighted with the rectangles in Figs. 4.1d,e. Also in Figure 4.1f, the Raman spectra of these black deposits display a signature that overlaps with the D and G bands of crystalline graphite, used as a reference). These results suggest that the blackish debris particles detected on and around the rubbing surfaces have a structural chemistry that is similar to the reference material graphite. Overall, the results in Figure 4.1 clearly show that the VN-Ni coating provided much lower wear in CH_4, and this improvement was most likely due to the formation of a carbon-rich tribofilm derived from the CH_4 gas during sliding experiment (Figure 4.1a).

We analyze a portion of the debris particles from the area highlighted with the rectangle in Figure 4.1 placing it on a copper grid for transmission electron microscopy (TEM). The TEM images in Figure 4.2 show two major types of debris: graphene with carbon nano-onions

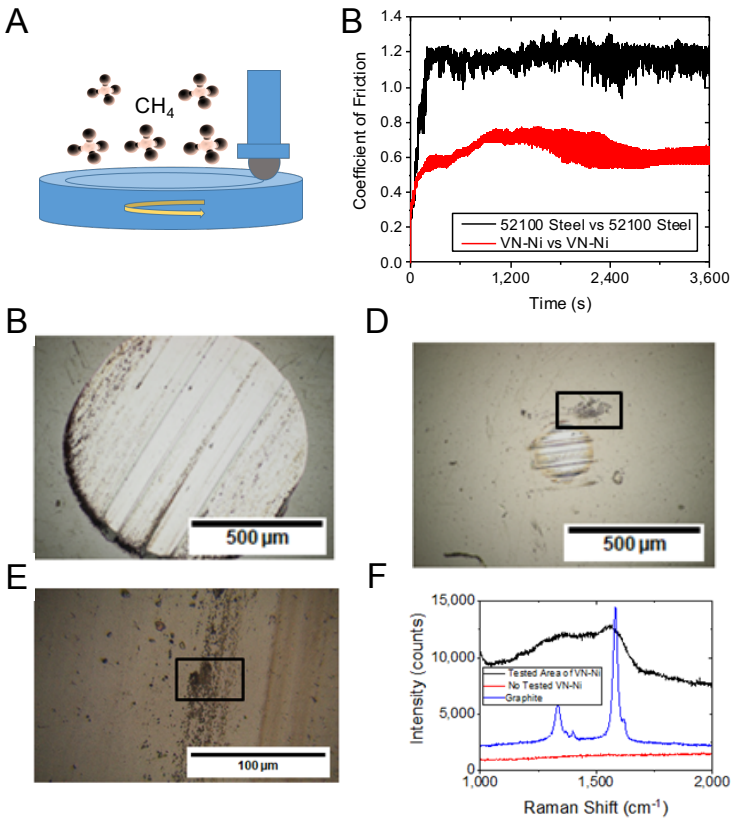

Figure 4.1: Comparison of friction and wear behaviors in ball-on-flat tests. (a) Schematic illustration of test method and environment. (b) The friction coefficient of uncoated AISI 52100 steel sliding against the same material compared with that of VN-Ni-coated AISI 52100 steel sliding against the same material in 960 bar CH_4 gas. (c) Size of wear scar formed on uncoated AISI 52100 steel ball in CH4. (d), Size of wear scar formed on VN-Ni-coated AISI 52100 steel ball in CH_4. (e) SEM image of wear track on VN-Ni coated surface with blackish wear debris layer. (f) Raman spectra obtained from the are denoted with a black rectangle showing broad D and G bands located in the same position as the ones corresponding to the graphite used as a reference.

(Figs. 2a,b,c) and an agglomeration of numerous nanoparticles wrapped by highly disordered graphitic carbon (Figs. 4.2d,e). The first type is mainly a large graphene sheet ranging from 500 nm to several micrometers in size, as shown in Figure 2a. High-resolution transmission electron microscopy (HRTEM) showed that the graphene sheets are composed of a single layer (Figure 4.2b) to about 10 layers (Figure 4.2c). Single-layer graphene is confirmed by an HRTEM image at broken edges (see Figure A.7). Carbon nano-onions with diameters of 5 to 10 nm were scattered on the graphene sheet, as highlighted in Figs. 4.2b,c, throughout the examined area. These carbon nano-onions are hollow in the center, and no other crystalline form of carbon structure is observed. Compositional analyses by energy-dispersive X-ray spectroscopy (EDS) and electron energy-loss spectroscopy (EELS) show that the nano-onions are composed

of graphene with a small amount of Ni and V (see Figure A.7). The small amounts of Ni and V could act as catalysts for the growth of graphene and carbon nano-onions.

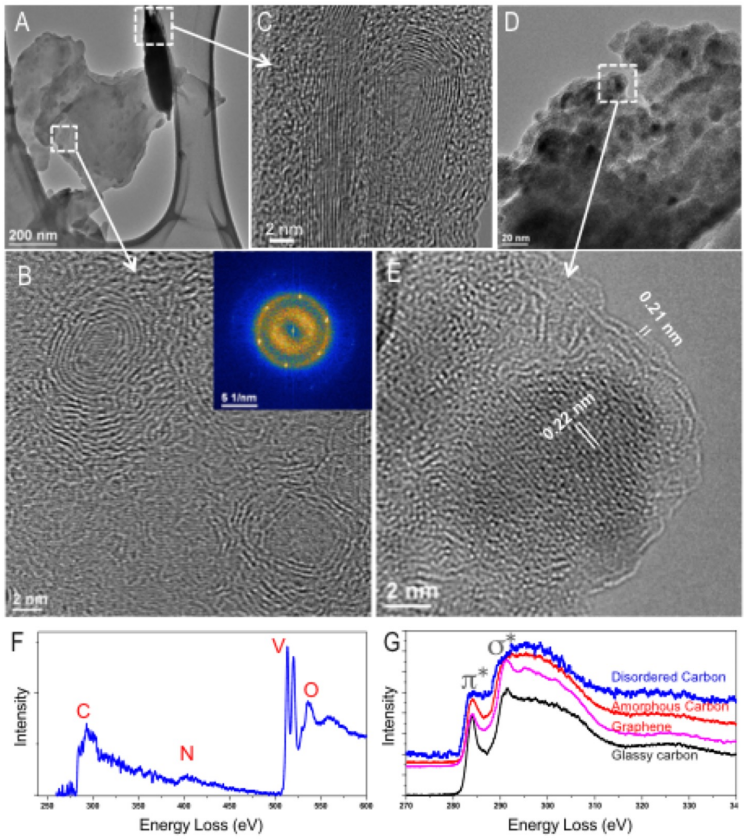

Figure 4.2: TEM study of debris particles. (a) Low-magnification and (b) HRTEM images of large graphene sheet with scattered carbon nano-onions. **C**, TEM image showing side view of carbon nano-onions attached on graphene sheet (about 10 layers). (d) Low-magnification and (e) HRTEM images of agglomerated nanoparticles wrapped with highly disordered carbon. (f), EELS spectrum from agglomerated debris showing almost no N. (g), EELS spectra of carbon K-edge of disordered carbon, compared with glassy carbon (standard), graphene taken from image(**B**)b), and amorphous carbon on the TEM grid.

4.4 Discussion

Results presented above demonstrate that the VN-Ni coating is able to convert CH4 into graphene, carbon nano-onion, and disordered carbon, all of which are known for their favorable anti-friction and -wear properties [229, 230, 233]. Specifically, friction was reduced by 50%, and the wear was reduced by a factor of 245. As is evident from Figure 4.1b, the reduction in friction is not as dramatic as in wear. This is mainly due to the incomplete coverage of sliding surfaces with a continuous layer of graphene and other carbon forms. Specifically, due

to their very soft nature, they are prevented from thickening into a continuous tribofilm under the influence of high contact pressure and shear forces exerted on them. Instead, they are ejected from the interface and accumulated around the edges of the wear scar and track as highlighted with rectangles in Figs. 4.1d and 4.1e. Further, the shear properties of graphene and other carbon nanostructures are not as favorable in nitrogen and methane.

It can be deduced that Ni and VN, which are the key constituents of the coating, are most likely acting as catalysts for the tribochemical conversion of CH_4 into graphene, nano-onion, and disordered carbon. Indeed, such carbon structures were only found in and around the sliding contact areas. Ni is used extensively in the synthesis of graphene, nanotubes, and nano-onions by chemical vapor deposition (CVD) at high temperatures [239], and the specific steps involved in the catalytic conversion of hydrocarbon gases into graphene by CVD method using Ni and other metals are well-documented [240–243]. These studies have suggested that partially filled Ni d-orbitals enable it to adsorb hydrocarbon molecules and to facilitate their dehydrogenation. Liberated carbon atoms are free to migrate throughout the surface (as well as into the bulk) and eventually come together to form the planar sheets of carbon as in graphene [239]. Vanadium and its nitrides are also well-known to have strong catalytic activity especially in the de-hydrogenation of hydrocarbons and ammonia [244–246]. In our case, there was no similarity to the traditional CVD synthesis route, rather a situation involving two VN-Ni coated surfaces pressed against one another in relative motion in the presence of CH_4 at ambient pressure and temperature. Yet, these rubbing surfaces were able to extract graphene and other carbon nanostructures in a continuous manner from the methane gas and thereby enable ultra-high resistance against wear.

Because of the very complex nature of the physical, chemical, and tribological events taking place at a sliding contact interfaces, understanding of the exact mechanisms by which graphene, carbon nano-onion, and disordered graphitic carbons are derived from CH_4 on VN-Ni is rather challenging. In particular, determining time and spatial resolutions of events leading to the formation of such carbon nanostructures is deemed impossible with currently available tribological methods. However, it is conceivable that under the tribological contact configuration shown in Figure 4.1a and conditions described in section A, *i.e.* a high-pressure mechanical shearing action combined with transient high flash heating of real contact spots [247], the tribochemical extraction of such carbon nanostructures from CH_4 may become feasible. Specifically, the high-pressure rubbing action continuously creates nascent surface atoms of the catalyst Ni, which enhances catalytic and tribochemical activity towards methane in the surrounding environment. As mentioned above, both Ni and V are well-known catalysts used previously in the synthesis of graphene and carbon nanotubes by high-temperature CVD methods [240–243]. They lower activation energy for dissociative extraction of carbon from methane and hence facilitate the formation of such carbon materials.

4.4.1 Ab Initio Molecular Dynamics Investigation

We conduct from *ab initio* molecular dynamics (AIMD) simulations, to provide further insight into the atomistic mechanisms that govern the tribochemically induced formation of carbon nanostructures.

First, we evaluate the catalytic capability of the Ni and VN substrates in promoting the CH_4 dehydrogenation. The results of this study, reported in section A.2 (Figures A.8,A.9), are in agreement with the literature in the case of Ni [236–238, 248], while we are not aware of any previous study for VN. The reaction energies calculated for methane dissociation on Ni(111) and VN(100) surfaces, which are the most stable surfaces for these materials, correspond to 0.02 eV on and 0.89 eV, respectively. Therefore, at ordinary conditions, the full dehydrogenation reaction, $CH_4 \longrightarrow C_{ads} + 4H_{ads}$, is not energetically favorable. However, the molecular confinement, the mechanical stresses applied, and high temperatures present at the tribological interface are able to promote the dehydrogenation reaction at a very high rate, as shown by the AIMD simulation described in the following.

In AIMD simulations both electronic and ionic degrees of freedom are taken into account. This approach is essential to obtain an accurate description of the chemical processes occurring under conditions of enhanced reactivity. The first set of simulations aimed at identifying the mechanisms of carbon release from CH_4 molecules, while subsequent simulations, where the concentration of interfacial carbon was increased, were aimed at monitoring in real time the formation of carbon nanostructures assisted by mechanical stresses.

The initial system configuration, shown in Figure 4.3a, contained a concentration of CH_4 molecules such that the number of C atoms corresponded to 25% of the Ni interfacial atoms. The temperature of the Ni surfaces is kept constant at 1000 K, while the intercalated molecules are left free to evolve without any temperature control. A normal pressure of 5 GPa is applied, and the upper surface is moved at a constant velocity of 200 m/s along the $[11\overline{2}]$ direction. The dehydrogenation process starts immediately after the beginning of the dynamic simulation (Figure 4.3a): H atoms detach from CH_4 molecules as soon as they come into contact with the clean Ni surfaces. This result indicates that molecular dissociation, which is energetically unfavorable at the open surface, can be easily promoted at the tribological interface, as previously found for water molecules confined at diamond interfaces [30, 97, 249] and organophosphorus additives at iron interfaces [122]. The simulation then indicated H diffusion into the Ni bulk, which leads to an increase of carbon concentration at the interface. This is consistent with the above-described experimental observation of newly formed carbon nanostructures almost H free. After $\sim 2\,\mathrm{ps}$, around 20% of the H atoms had been expelled from the interface and diffused into the bulk. At the same time, more than half of the carbon atoms were adsorbed on the surfaces, where they tend to capture other C atoms, forming small hydrocarbon groups,

C_nH_x with $n \leq 2$ (Figure 4.3b). After ~ 3 ps from the beginning of the simulation, the interfacial concentration of H atoms decreased by more than 50% with respect to the initial value, and all the C atoms present at the interface become bonded either to surface Ni atoms or to other C atoms in short carbon chains, C_n with $n \geq 2$ (Figure 4.3C). Reactive carbon intermediates, C_n, have been also identified during the thermal decomposition of CH_4 on Ni(111) by the in-operando technique of near-ambient-pressure X-ray photoelectron spectroscopy [250]. Not observed were Ni_2C reconstruction and other carbide structures, which are often found during graphene growth on Ni(111). The origin of some differences with the structures observed during graphene growth may be related to the presence of a counter-surface: the coordination of molecular fragments during the decomposition process is always higher at the interface than at the open surface and this may *e.g.* limit the subsurface diffusion of carbon.

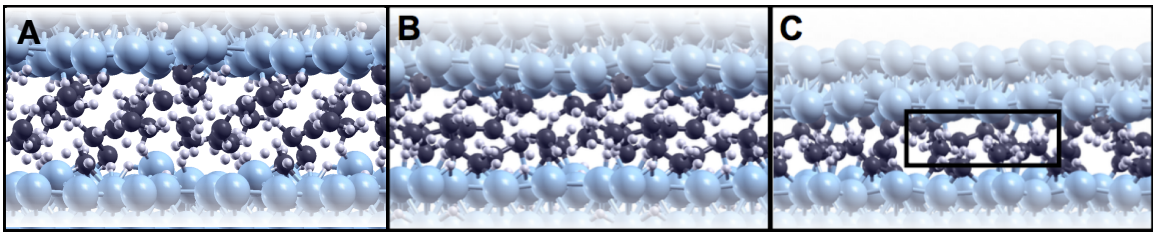

Figure 4.3: AIMD simulation of methane molecules confined at Ni interface during sliding. (a) Side view of the initial system configuration. (b) Snapshot acquired after 2 ps of AIMD at constant load and shear velocity: the molecules started dissociating and H atoms diffusing below the surfaces. (c) After 3 ps most of the H atoms were expelled from the interfacial region, and carbon-carbon bonds started to form. An adsorbed four-carbon chain is highlighted with a rectangle.

Figure 4.4 shows two snapshots acquired during AIMD simulations containing increased concentrations of C atoms, corresponding to 50% (a) and 100% (b) coverages of the Ni interface. In a first stage, we observed the formation of carbon chains the length of which increased during the simulation until every interfacial C atom had been included into a chain branch (Figure 4.4a). The chains become cross-linked, forming a disordered low density film. The applied load and shear smear out this film, reducing more and more its thickness. During this rubbing process, the carbon atoms change their hybridization and start to form planar rings that constitute the first seeds for graphene growth. Indeed, we observed the formation of a graphene flake upon further increase of C coverage (Figure 4.4b). The shift of the peak of the C-C radial distribution functions $g(r)$ from ~ 1.43 Å to ~ 1.47 Å (Figure 4.4c), clearly indicates the rehybridization from sp to sp^2 that accompanies the structural change from interconnected carbon chains to 2D structures. The similarity of the $g(r)$ function calculated for the Figure 4.4b structure (green continuum line), which also presents a second peak, and the $g(r)$ calculated for an undefected graphene layer commensurate to the Ni(111) surface (blue dashed-dotted

line) provides a further evidence that graphene is being formed during the simulation under the tribologic conditions. Recently, it was shown that carbon-based tribofilms can also be derived from a variety of carbon-based liquids including synovial fluids that lubricate joints, poly-alpha olefin (PAO) which is a base oil used in the making of synthetic lubricants, and palm methyl ester (PME) which is a biodiesel fuel extracted from palm oil. Specifically, it was reported that a graphitic tribofilm forms on the rubbing surfaces of metal-on-metal (MOM) hip replacements (which are made of cobalt, chrome and molybdenum) [251], MoN-Cu coatings [252] lubricated by a PAO oil, and AISI 304 stainless steel lubricated by PME [253]. MOM is thought to derive graphitic tribofilm from protein molecules through the catalytic effects of Co and Mo. While in the cases of MoN-Cu and AISI 304 stainless steel, Cu and Ni present in their structures, respectively, are believed to help in the extraction of carbon-rich tribofilms from the PAO and PME molecules.

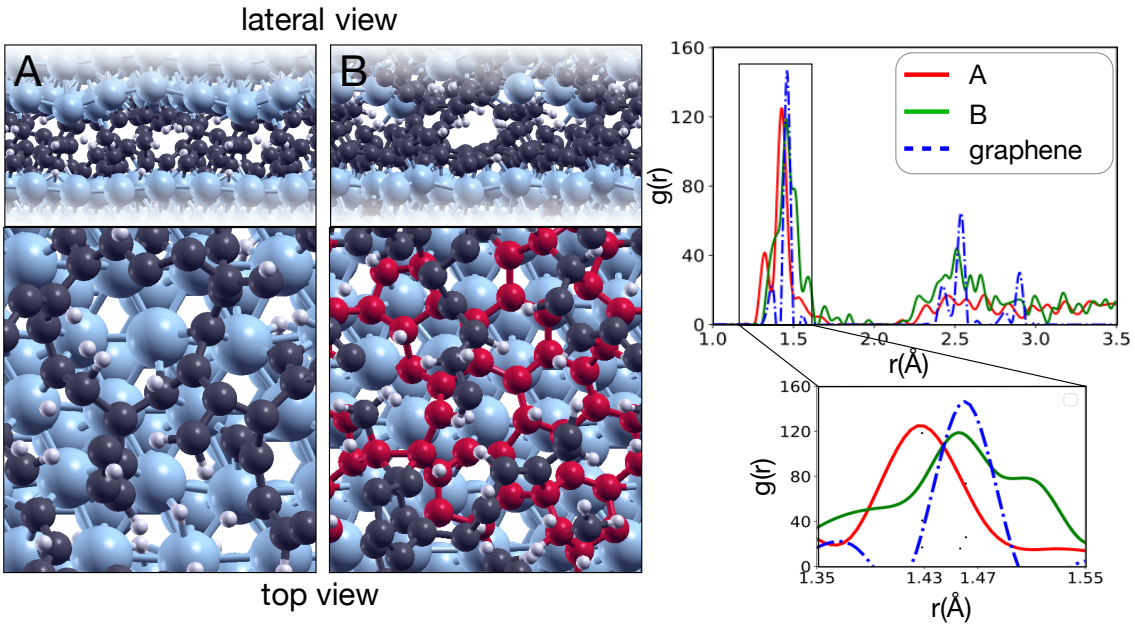

Figure 4.4: First stages of tribologically induced graphene formation. Snapshots acquired during AIMD simulations of dehydrogenated methane molecules confined at Ni interfaces in concentrations corresponding to (a) 50% and (b) 100% coverages of the Ni interface. A. In a first stage the C atoms bind to each other in interconnected chains that form a disordered, low density film. B. The load and shear stresses applied promote the rehybridization of C atoms and the formation of sp^2 planar structures as the graphene flake highlighted in green. (c) The corresponding radial distribution functions for C-C bonds are represented by red and green lines, respectively, while dashed-dot blue line indicates the radial distribution function of an undefected graphene layer commensurate with the Ni(111) surface.

4.5 Conclusions

The results demonstrate that tribochemistry plays a major role in the friction and wear behavior of sliding surfaces. Specifically, under the high-pressure shearing condition described in this study, VN-Ni coating can convert CH_4 molecules into graphene, nano-onion, and disordered graphite, which in turn reduce friction (by as much as 50%) and wear by two to three orders of magnitude (see Figure 4.1). High catalytic reactivity of Ni and Cu in the composite coatings promotes tribochemical conversion of CH_4 to a carbon-based tribofilm consisting of graphene, nano-onion, and disordered carbon. Transmission electron microscopy (Figure 4.2) shows that graphene is preferably formed on and around the VN-Ni clusters, while nano-onions and highly-disordered graphite were scattered throughout the carbon tribofilm. Ab initio MD simulations (Figs. 4.3, 4.4, A.8-A.9) reveal the mechanism by which carbon nanostructures are extracted from CH_4 molecules. The simulations show that the conversion of CH_4 to 2D graphene and nano-onions occurs by a catalytic process involving first the dehydrogenation of CH_4 on Ni followed up by C atoms forming chains of an amorphous carbon network of low atomic density. Under the influence of high contact pressure and shear forces, some of the amorphous carbon network sandwiched between the Ni surfaces undergoes rehybridization and subsequent conversion to sp^2 planar structures. These newly formed sp^2-bonded hexagonal rings nucleate the first graphene flakes. Once such graphene-rich tribofilms are formed on sliding surface, wear is reduced dramatically, by more than one order of magnitude [103, 116, 253]. Overall, this study demonstrates the critical role of tribochemistry in the extraction of low-shear, highly protective carbon tribofilms from CH_4, that can provide a remarkable reduction of friction and wear.

Part III

Mechanisms Governing Triboelectrification in Polymeric and Solid Insulators

Chapter 5

Structural and Electronic Properties of Polytetrafluoroethylene in Its High-Pressure Phase

5.1 Introduction

[1] PTFE is the most used polymer for a number of technologies which require specific mechanical, electrical, chemical and thermal properties. It is widely used for its low friction and wear, chemical inertness, resistance to adhesion, hydrophobicity and biocompatibility. Nowadays, PTFE is the most popular insulating polymer for triboelectric applications, such as harvesting devices [7, 8]. These are based on contact-induced electrification effects by which certain materials become electrically charged after they come into frictional contact with a different material [129, 141, 142, 255–260]. Despite thousands of years of research on triboelectrification, the phenomenon is still being studied and debates still arise over aspects of the mechanisms behind it [261]. Recent studies, for example, disputed the unidirectional transfer of charge by showing a mosaic distribution of charge [42, 259, 262], that is likely due to mechanochemical reactions [263]. In addition to triboelectric technologies other industrial applications employed PTFE as material for components such as sliding [264] and dry bearings [265] and Teflon beads [266] and for all of them PTFE experiences high pressure conditions. It is known that PTFE properties are based on the interaction of fluorinate carbon species, where the fluorine high electronegativity generates quite polar C-F bonds. Moreover, the presence of fluorine significantly influences intermolecular interactions which are consistent with high thermal and chemical stabilities [267]. To better understand these properties, obtaining a clearer understanding of the electronic structure of PTFE is mandatory. Despite the fact that several com-

[1] Work first published as Ref. [254]

bined experimental and theoretical studies [268–278] and various calculations [279–286] have been reported, the most important characteristics regarding the structural and electronic nature of this polymer, in particular, under high pressure conditions for discussing the electric and electronic properties could not be clearly determined. For instance, previous first-principles studies on the structural characterization of the PTFE focused only on its hexagonal crystal structure [281]. Therefore, there is a lack of information regarding the monoclinic and orthorhombic crystal structures which exist at high pressure conditions. The electronic properties were, instead, previously defined only for single chain [271, 278, 286] lacking information on the electronic interactions between the chains. PTFE, consisting wholly of carbon (C) and fluorine (F), shows a peculiar polymorphic behavior involving three unique crystalline phases. The two crystalline phases at low pressure and temperature are usually denoted as form II consisting of helical chains containing 13 CF_2 in 6 turns and stable at temperatures lower than 19 $^{\circ}C$ and form IV consisting of helical chains contain 15 CF_2 in 7 turns and stable at temperature between 19 and 30 $^{\circ}C$. These phases have been studied extensively and are relatively well understood [287–289]. The third phase, called form III, observed above $\sim 0.65\,\mathrm{GPa}$, consists of zigzag planar chains and it is stable at temperatures higher than 30 $^{\circ}C$ up to the melting point of 33 $^{\circ}C$ [290]. Spectroscopic data indicated that at pressures above 0.65 GPa the molecules untwist from the low pressure helical conformation to the planar zigzag conformation of phase III [291]. X-ray diffraction measurements on form III have indicated a monoclinic structure [292], whereas another X-ray study [272] has indicated a structure similar to that of orthorhombic polyethylene (PE). An additional study [293], which adopted a range of pressures between 0.95 and 5.2 GPa at 300 K found that from a pressure of 2 GPa onwards a monoclinic crystal structure coexists with an orthorhombic crystal structure. Here, we present insights into structural and electronic properties of PTFE in its high-pressure phase by a first-principles approach. In our study phase III plane zigzag chains containing 8 CF_2 units are packed in a monoclinic and orthorhombic crystal structure and three different exchange-correlation functionals (PZ, PBE and PBE-D) are compared. Crystal structure parameters, atomic positions, bond lengths, bond angles, cohesive energy density and binding energy are calculated and compared with literature values. The optimized structures are then used to determine the electronic states and the charge density distribution within the crystal.

5.2 Computational Details

Density Functional Theory (DFT) as implemented in the Quantum ESPRESSO package was used to perform first-principles calculations to describe the structural and electronic properties of PTFE bulk. We adopted and compared results from i) local density approximation

(LDA), with the Perdew-Zunger (PZ) exchange-correlation functional [294], ii) general gradient approximation (GGA), with the Perdew-Burke-Ernzerhof (PBE) exchange-correlation functional [187, 295], iii) and the same PBE functional corrected by a dispersion term (PBE-D) to model the long range van der Waals (vdW) interactions. The dispersion term was introduced using semi-empirical Grimme method [296] which is characterized by two parameters, scaling parameter and vdW cut-off radius. This dispersion term was tuned to obtain accurate structural parameters and to reproduce experimental binding energy values. The atomic species were described by ultrasoft pseudopotentials and the electronic wave functions were expanded in plane-waves. The structural and electronic properties were analyzed with the focus on high pressure (above 0.65 GPa), at which it is known that PTFE assumes a zigzag chain conformation 46 in coexisting orthorhombic and monoclinic crystal structures [272, 285]. Therefore, we considered and compared the PTFE properties of these two different configurations. In addition, the outcomes of orthorhombic structure analysis allowed us to make a direct comparison with the results of the same structure of PE [277, 297] another polymer which is extensively used due to similar electronic properties. The PTFE stem was first optimized by performing an energy convergence test. The isolated stem was studied by introducing a vacuum of 30 Å on each side of the stem, to prevent any interaction between the periodic replicas. We found an optimal length of 8 CF_2 monomers. The optimized stem was then employed for the structural properties analysis. The calculations for monoclinic structure were performed on a 2×1 cell to obtain the same degrees of freedom as in the unitary orthorhombic cell and provide an accurate comparison between the two geometries (Figure 5.1a, b). Monkhorst-Pack grids [189] with $(2 \times 2 \times 4)$ and $2 \times 3 \times 4$ k-points sampling were used to sample the Brillouin zone of the monoclinic and orthorhombic cell, respectively. The electronic properties were calculated using the optimized crystal structures and the partial charges of the atoms were computed by means of the Bader analysis [191–194].

5.3 Computational Details

5.3.1 Structures Optimization

An initial optimization of the lattice structures was conducted to provide a good description of the two high pressure configurations of the PTFE. The structure of the two cells and the stem used for the calculations is shown in Figure 2. The long horizontal edge and the short vertical edge of both monoclinic and orthorhombic cell are indicated by the lattice parameters a and b, respectively (Figure 5.1a, b), and the stems length is defined by the parameter c (Figure 5.1c). The angle of the monoclinic cell is indicated by the parameter γ (Figure 5.1a). In the orthorhombic configuration, PTFE stems are tilted by a setting angle with respect to

the b axis (Figure 5.1b).

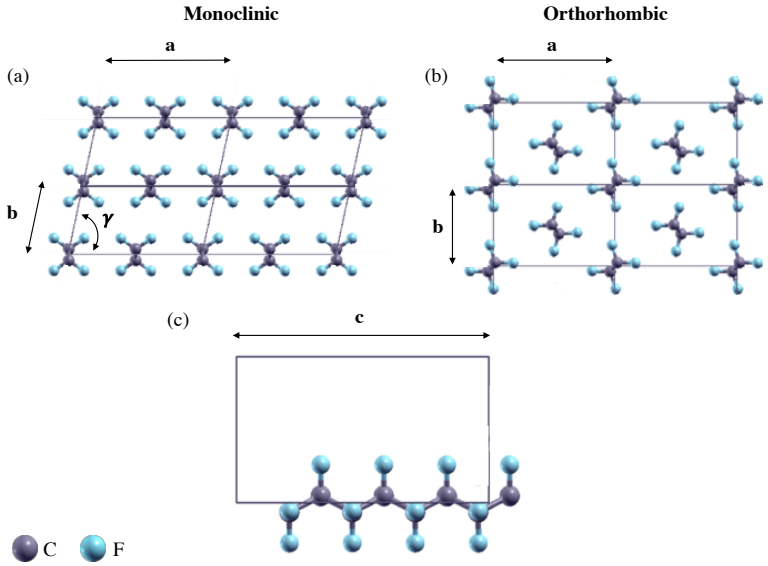

Figure 5.1: PTFE configurations at high pressure (a) monoclinic structure and (b) orthorhombic structure and (c) length of the PTFE stem.

The following steps were adopted to identify the convergence cut-off for the plane-wave expansion and optimize the two cells structure. Firstly, the cells parameters were set as found in literature [298]. Then the structures were relaxed, varying the lattice parameter c, while performing a convergence test on the cut-off. For each cut-off, the energy values at c were fitted by the Murnaghan equation of states [299] to find the minimum energy configuration. Although the Murnaghan equation of states is limited in the way it describes non-elastic behavior, in the case of PTFE, far away from the equilibrium, we strongly believe that it is suitable to describe a configuration close to the equilibrium. We found an optimum cut-off value of 40 Ry (320) for the wave functions (electron density). Using the obtained cut-off and the equilibrium value of c, we then optimized the lattice parameters a and b for both cells, and γ for the monoclinic cell, using the same fitting procedure. Table 5.1 shows the parameters values of the optimized structures, together with the intramolecular bond lengths and angles, Cohesive Energy Density (CED) and binding energy E_b per monomer. For PBE-D the scaling parameter of the vdW correction was tuned to a value of 0.42 to reproduce a CED consistent with the experimental data.

In both monoclinic and orthorhombic cells, a and b parameters are adequately described by PZ and PBE-D functionals, whereas they are overestimated by PBE. This was expected due to the fact that PBE overlooks long-range interactions, and this is also confirmed by the significantly low CED. The stem length, c, estimated by PZ is, as expected, lower compared to that obtained using PBE and PBE-D, because PZ generally overestimates the interaction

	Monoclinic				Orhorhombic			
	PZ	PBE	PBE-D	exp.	PZ	PBE	PBE-D	exp.
a Å	9.64	10.10	9.79	9.5036[283]/9.0435/8.5238/9.4438[285]	8.54	9.14	8.70	8.73[269]
b Å	5.17	5.60	5.15	5.05[283]/5.29/5.08/5.03[285]	5.79	6.14	5.94	5.69[269]
c Å	10.38	10.65	10.61	10.48[283]	10.38	10.64	10.61	—
γ [deg]	104.7	102.4	101.8	105.5[285]	—	—	—	—
setting angle [deg]	—	—	—	—	42/40	37/38	37/38	35[285]
C-C Å	1.56	1.59	1.58	1.541[283]	1.55	1.58	1.58	1.541[269]
C-F Å	1.34	1.36	1.36	1.344[283]	1.34	1.36	1.36	1.344[269]
C-C-C [deg]	112.9	114.0	113.7	116.6[283]	112.9	113.9	113.8	—
F-C-F [deg]	109.5	109.0	109.3	109.5[283]	109.5	109.0	109.1	108.5[269]
CED[N/cm^2]	309.9	15.6	194.2	185[270]	229.2	31.0	194.3	185[270]
E_b eV	0.097	0.014	0.081	—	0.120	0.007	0.083	—

Table 5.1: Summary of the crystal structure parameters (a, b, c and γ), atomic positions, setting angle, bond lengths, bond angles, cohesive energy density (CED) and binding energy (E_b) of the optimized monoclinic and orthorhombic structure and experimental literature values.

energies. This is also reflected in the smaller backbone C-C-C angle and in the higher CED. Likewise, PBE and PBE-D underestimate the backbone angle. We attribute this discrepancy to the intermolecular interactions, absent or at least different in nature in the previous studies that adopted single chain or hexagonal cell [283, 284]. The C-C and C-F bond lengths as well as the F-C-F angle are well described by all the functionals. In the orthorhombic cell the setting angle is slightly overestimated by PBE-D and PZ, while significantly overestimated by PBE. Finally, the last row of Table 5.1 shows that the binding energy between the two stems is similar for both monoclinic and orthorhombic cell. Therefore, we can confirm the coexistence of the two structures. Overall, we can conclude that PZ overestimates the short-range interactions and PBE completely overlooks the intermolecular interactions. Instead, PBE-D characterizes correctly both short and long-range interactions, providing an accurate description of all the parameters. It can, therefore, be considered the functional which better describes the structural properties of PTFE in the high-pressure configurations.

5.3.2 Electronic Properties

To provide insights into the electronic properties of both the monoclinic and orthorhombic PTFE structures we began by calculating the charge density distribution and the partial charges of the atoms. The outcomes show the transfer of electronic charge from carbons to fluorines inside the monomers which is due to the difference of electronegativity between the two atoms (7.86 - fluorine, 2.14 - carbon). The partial charges do not differ either between PZ, PBE and PBE-D functionals, or between the orthorhombic and monoclinic structures; the fluorines in the CF_2 monomer accumulate ~ 0.86 electron charge, while carbon loses ~ 1.72 electron charge. We, then, calculated and compared the band structure of the two considered cells for each adopted functionals. The monoclinic and orthorhombic band structures for each functionals

are shown in Figure5.2a,c, respectively.

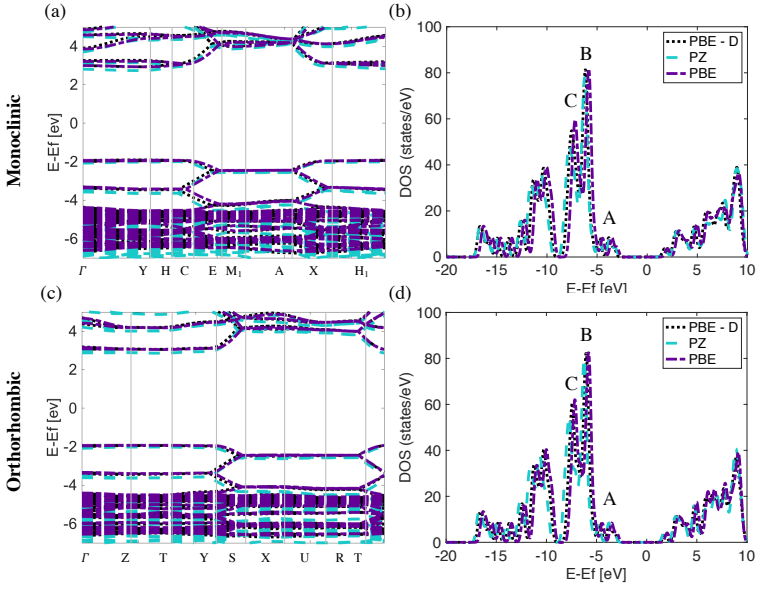

Figure 5.2: Band structure and DOS's of (a) and (b) monoclinic structure for PZ, PBE and PBE-D functional and (c) and (d) orthorhombic structure for PZ, PBE and PBE-D functional.

For both monoclinic and orthorhombic structures and for each employed functional the band gap is estimated around 5 eV, in good agreement with experimental measurements ($\sim$ 6eV) [275, 276]. However, the calculated value is lower when compared to previous theoretical studies ($\sim$ 8 eV) [281] and experimental UPS and optical measurements ($\sim$ 10eV) [271]. This difference between theoretical (DFT) and experimental values was expected because of the well-known band-gap problem of LDA and GGA in the calculation of the insulating band gap [300]. Overall, both valence and conduction bands dispersion does not differ significantly between the functionals and the cells structure adopted. In particular, for each functional and structure the band gap is direct, and little dispersion is observed at the highest occupied bands. Figure 5.2b, d show the total Densities of States (DOS's) of the monoclinic and orthorhombic structure, respectively, for all the employed functionals, with the energy values in abscissa related to the Fermi energy. The peak A derives from the two highest occupied bands of Figure 2a, c which correspond to the C-C interactions. B and C, instead, derive from the high-density bands which correspond to the C-F interactions. This agrees with previous theoretical studies on single chain in which it is suggested that the highest occupied bands are mainly derived from the interaction between the C2p and F2p levels [268]. The obtained DOS's profile aligns with previous studies reported in Ref. [283].

To observe the spatial configuration of both valence and conduction band additional analysis was conducted by calculating the charge density of the highest valence state and of the lowest conduction state. Figure 5.3 shows the results obtained with the adoption of PBE-D functional.

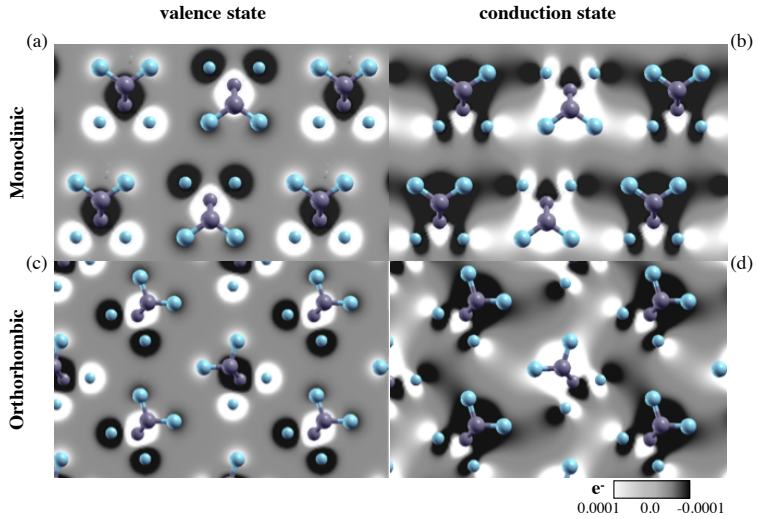

Figure 5.3: Spatial distribution of charge of (a),(c) the highest valence state for monoclinic and orthorhombic structure, respectively and (b),(d) the lowest conduction state for monoclinic and orthorhombic structure, respectively.

The charge density distribution of the valence (left panel) and conduction (right) state for both monoclinic and orthorhombic structure are shown in the top and in the bottom panel, respectively. The charge distribution of the valence state (Figure 5.3a, c) is localized inside the PTFE stem. Inversely, the charge distribution in the conduction band is delocalized along the entire length of the chain and positioned around the C-F bonds (Figure 5.3b, d); this aligns to previous experimental findings [277]. Moreover, in the conduction state an interchain charge density can also be noticed.

The observed spatial distribution of the conduction state is like that observed in the same kind of study on PE [277], where it is reported a clear inter-chain character. In that study the delocalization of the charge has been related to the formation of localized surface states inside the band gap, which allow electrons to be acquired and retained [277]. Based on this, additional studies on the surface electronic properties of PTFE will be conducted to explore its surface properties and their implications for interfacial interactions and the control of *e.g.* adhesion, wettability and triboelectrical response.

5.4 Conclusions

In this study, we used a first-principles approach to give, for the first time, insights on the structural and electronic properties of PTFE in its high-pressure phase. We confirmed that, at high pressure the PTFE at form III (zigzag planar) coexists in orthorhombic and monoclinic crystal structures.

1. The optimization of the lattice structures and the comparisons of the energy values obtained by adopting three different exchange-correlation functional (PZ, PBE and PBE-D), show that the PBE-D functional better describes the structural properties of PTFE in the two high-pressure configurations.

2. The addition of a dispersion term to model the long-range van der Waals interactions to the PBE functional overcomes the inability of PZ to estimate the short-range interactions and the failure of PBE to estimate intermolecular interactions.

3. The analysis of the electronic properties on the optimized structures reveals that an electronic charge transfers from carbons to fluorines inside the monomers. The charge is rearranged inside the stem and tends to concentrate around the fluorine atoms.

4. The band gap is estimated around 5 eV, which is comparable with some experimental findings but less with other previous theoretical and experimental studies because of the limits of the gradient-corrected (LDA/GGA) to calculate the insulating band gap. For both monoclinic and orthorhombic structure, the band gap is direct. Additional investigation of the band structures shows that the dispersion of both valence and conduction bands is not significantly affected by the functionals and cells structure adopted. The further DOS's calculations perfectly align with previous UPS and optical experimental analysis.

5. By focusing on the PBE-D functional calculations it can be seen that charge distribution of the valence state is localized inside the PTFE stem and instead the conduction band is delocalized along the entire length of the chain and between the chains. The inter-chain character of the conduction state reported here is like the inter-chain character reported by similar study on PE. This suggests that, as for the PE, surface states might be generated on PTFE surface.

Chapter 6

The Influence of Triboemission on Tribocharging Mechanism

6.1 Introduction

[1]The term tribocharging refers to the transfer of charge between rubbing components. A wide range of factors influences the transfer and the generation of charge, at macroscopic and atomic level. For instance, material stress can cause bond scission that result in a rearrangement of the charge of the surface and the release of ions and electrons [255]. The importance of tribocharging has led to the development of new nanoscale techniques and theoretical analysis [301] to study this phenomenon and better understand its fundamental mechanisms. In industry, tribocharging is employed in many applications including sliding [264] and dry bearings [265], pharmaceutical [10, 11], space [302] and green energy harvesting [8, 303] and it has the potential to be at the forefront of technological innovations. In particular, in lubricated contacts in the formation of boundary films and in certain cases in their degradation tribocharging and a phenomenon known collectively as triboemission they have been suggested as playing a key role. Triboemission consists of emission of charged particles such as electrons, protons, positive and negative ions and also acoustic emission that occur when hard, solid surfaces are rubbed together[141, 142, 260, 304–308]. If a lubricant is present, these particles may promote chemical reactions that lead to both degradation [309], and formation of protective films on the surface of components [52]. Previous studies, on tribocharging effects, have shown the occurring of various tribochemical reactions during wear due to contact potential differences on the worn surfaces [310]. It has been found that the electrical potential of the materials can differ due to tribologically generated phase transformed regions and that nanoscale wear causes chemical and structural changes to the material surfaces [311, 312]. Under lubricated conditions the

[1]This work is currently in press on Tribology Online

voltage of the surface induced by frictional contact was found dependent on the movement of charge and influencing the friction and the type of wear [313, 314, 314]. Other studies have reported the influence of combination of tribocharging and triboemission in both dry and lubricated contacts [315–317]. These studies showed that lubricating oil molecules are excited and decomposed by the emission of electrons accelerated by the tribocharging-electric filed both inside and outside of the sliding contact.

Despite years of research these two phenomena are not yet well understood because of the limits of experimental techniques at atomic level and because of lack of theoretical studies. This study aims at elucidating the underlying mechanisms of tribocharging and triboemission by combing experimental and theoretical methods. A recently developed measurement system is used to obtain information of the charging of the silica and emission events during the sliding of a simulate asperity contact. A theoretical approach based on first-principles methods is, instead, used to provide insights into the contribution of contact-induced electrification to the charging of the surface.

6.2 Research Methods

6.2.1 Experimental Method

The experimental part of this study[2] was conducted by using a unique high vacuum in-house built tribometer [306, 307, 318], schematically represented in Figure 6.1. It consists of: *i*) a system of microchannel plates (MCPs, i.e. arrays of electrons multipliers), coupled with a phosphor screen to detect and visualize the emission, respectively; *ii*) a loading system comprising of a dead-weight arrangement and a diamond tip of radius 100 μm to produce the sliding contact; *iii*) and a PCS Instruments encoder device used to record the rotation of the disc. A high-speed camera located above the experimental setup was used to record the emission as they appeared on the phosphor screen. In addition, simultaneously with the emission detection, an electrometer coupled with a 10×5 mm metal sheet electrode attached underneath the specimen was used to inductively measure the accumulation of the charge on the specimens.

The tests were conducted in vacuum conditions at a pressure of $\sim 10 - 3$ Pa. The detection of negative particles (i.e. 10-85% of 0.01-50 keV [319]) was obtained by applying 1.5kV, and 5kV to the input MCP and output MCP, respectively, with the phosphor screen being grounded. A sliding velocity of 50 mm/s and a load of 0.5 N were set for all the tests. The encoder, the frame rate of the high speed camera and the electrometer acquisition were synchronized at 125 Hz. The specimens used were silica amorphous discs (diameter of 46 mm and a thickness of 6mm). Prior to each test the discs were cleaned with toluene followed by isopropanol in an ultrasonic

[2]The experimental tests were performed by Dr A. Ciniero at Imperial College London

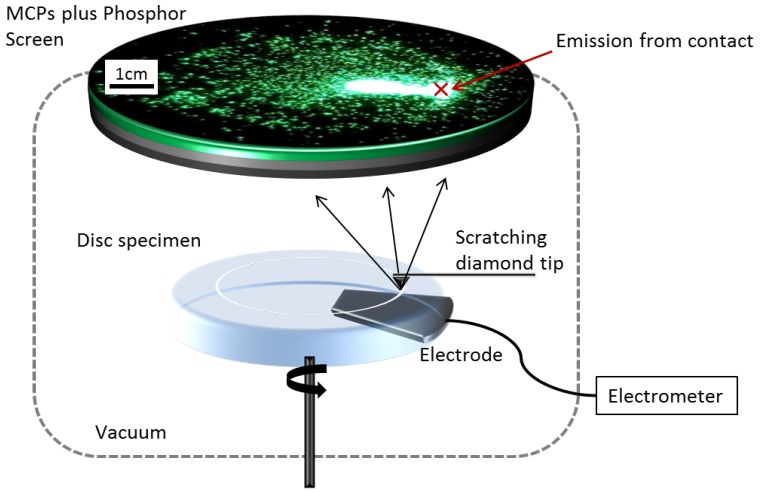

Figure 6.1: Schematic of the high vacuum tribometer.

bath (15 minutes for each chemical). The surface analysis of each specimen was conducted by using an optical profiler.

6.2.2 Computational Method

The theoretical part of this study was conducted by employing first-principles calculations based on Density Functional Theory (DFT) as implemented in the Quantum ESPRESSO [186] package to describe the transfer of the electrons between silica and diamond. We adopted local density approximation (LDA) as parameterized by Perdew-Zunger (PZ) [294] to describe the exchange-correlation term. The kinetic energy cut-off of the plane wave expansion was set to 35 Ry. An orthorhombic cell of $9.83 \times 17.03 \times 35.00$ Å dimensions including a vacuum region of 10 Å and gamma-point centered Monkhorst-Pack k-point grid [189] was used in all the calculations. The dimension of the system can be considered big enough to take in account the silica amorphous correlation length (4-8 Å [320]) and to mimic bulklike features of the respective slabs. The silica bulk was prepared by classical MD in a periodic $9.83 \times 17.03 \times 10.79$ Å cell with 48 O and 96 Si atoms. The variable-charge interatomic potentials used for the classical MD simulation are the charge-optimized many-body (COMB) potential for Si/SiO2 [321] as implemented in the Large-scale Atomic/Molecular Massively Parallel Simulator (LAMMPS) software [322]. The initial α-quartz structure was heated from 300 K to 3000 K for 100 ps at a constant temperature and pressure allowing the shape and the size of the simulation box to change. The silica melt was then maintained at 3000K at a constant box volume for 100ps to ensure a complete melting. The silica melt was then quenched at 300 K for 100 ps [323]. The final density and cohesive energy of the amorphous silica thus obtained are $2.36\,\mathrm{g/cm^3}$ and -19.22 eV in agreement with experimental measurements [324]. The average values of Si-O and

O-O bond length and O-Si-O bond angle obtained are 1.57 Å, 2.71 Å and 106.5°, respectively. These are in agreement with experimental values of 1.6 Å, 2.6 Å and 109.28° [325].

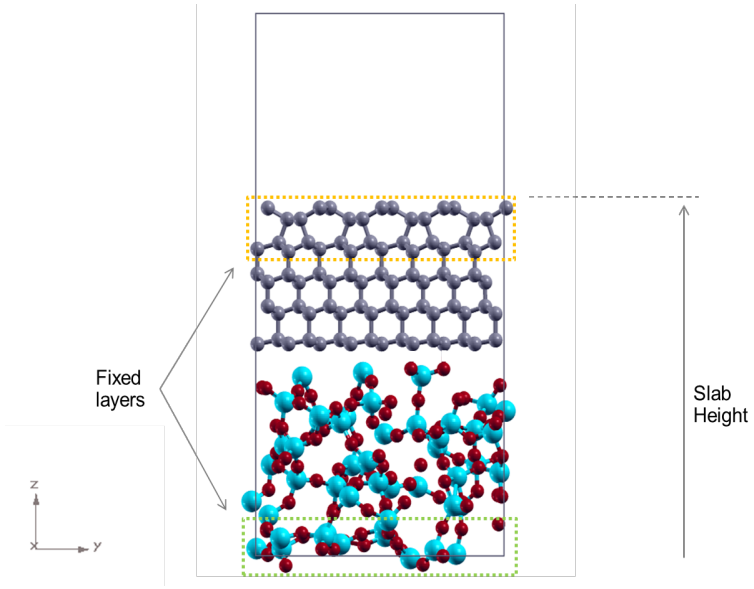

Figure 6.2: Orthorhombic cell, (4×7)-C(111) Pandey reconstructed slab and amorphous SiO_2 slab.

The diamond slab was constructed from (4×7)-C(111) surface, with the vacuum side Pandey reconstructed, resulting in a slab of 320 carbon atoms distributed on five bi-layers, corresponding to a thickness of 8.77 Å. This geometry consists of planar zig-zag carbon chains extended at different quotas. The outermost chain displays C-C length of 1.44 Å, instead the lower chain is characterized by C-C bond length of 1.5 Å, corresponding to that associated with sp^3 coordination [326]. While the other horizontal C-C bonds have same length (in consistency with the literature which reported no dimerization on the chains [327–329]), the C-C bonds below the top bilayer are characterized by an alternation of shorter and longer length. The Pandey reconstruction was chosen because of its most stable termination not only of the (111) surface but also of all the low-index diamond surfaces. At the interface, instead, the diamond slab was cut perpendicular to the [111] direction, generating unreconstructed C(111) surface, allowing the carbon atom dangling bonds to interact with the silica surface. The size of the diamond slab was chosen in order to minimize the mismatch with the silica. The two slabs were placed together at a distance of ~ 2 Å with the silica amorphous slab at the bottom and the C(111) slab above as shown in Figure 6.2, the atoms were allowed to relax to achieve the equilibrium configuration which resulted in a total slab height of 22.25 Å.

In order to simulate the variation of the distance between the two surfaces that occurs during sliding the two slabs were separated by moving the upper slab in discrete steps along the z direction and letting the system to relax after each step [330]. For the atomic relaxations

the top two bi-layers of the C(111) and the SiO_2 atoms up to 3.45 Å in the z direction were kept fixed at bulklike distance, whereas the intermediate atoms were allowed to fully relax. The separation of the slabs was initiated from the equilibrium and to simulate a realistic separation only the topmost rigid C(111) layers were moved in discrete steps of 0.1 Å in the positive z direction.

6.3 Results and Discussion

6.3.1 Experimental Outcomes

Charge and emission measurement during sliding test without fracture

Sliding tests where no fractures were observed on the surface (an example is shown in Figure 6.5d) generate positive charge of the surface and low negative emission. The cumulative value of the charge of the surface and the cumulative value of the average intensity of each phosphor screen image are plotted as function of the time in Figure 6.3a.

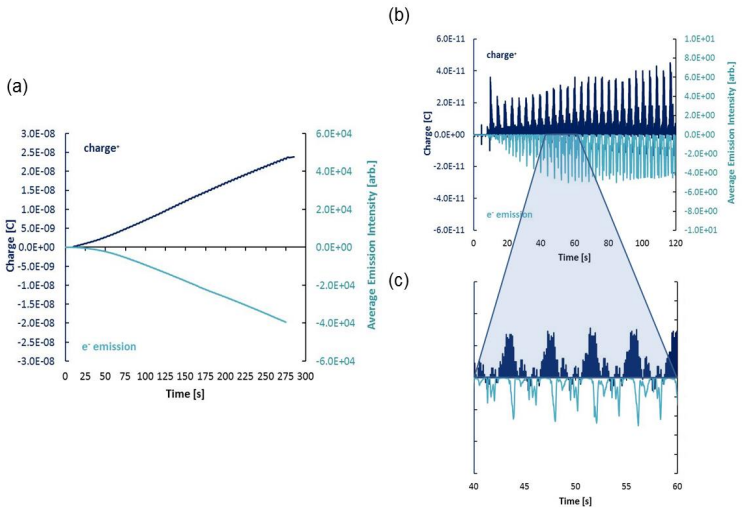

Figure 6.3: (a) Average intensity of each phosphor screen image and surface charge vs. time (cumulative values); (b) Average intensity of each phosphor screen image and surface charge *vs.* time, (instantaneous values), (c) Zoom of the period between 40 and 60 s, during sliding test without fracture.

The surface charge measurements and the simultaneously average of emission intensity show a correlation between charging and emission. It can be seen that the silica charges positively while the intensity of the emission increases over time in accordance with the triboelectric series [331–333] and previous studies [36, 261]. Observations of the resulting linearity of surface

charge and the emission intensity curve leads to the conclusion that the emission of negatively charged particles contributes to the positive charging of the silica specimen.

The discretization of both charge and emission measurements is presented in Figure 6.3b. This shows that both the charge and the emission intensity are characterized by numerous high peaks which begin to occur simultaneously at the start of the sliding. These results support the theory that emission is due to the wearing of the surface as previously observed [317, 334–336] and that in turn the wear influences the charge of the surface. A clear correlation between the charge and the average emission intensity is evident when observing the zoomed in Figure 6.3c. Here, a correspondence can be seen between peaks of positive charges and peaks of negative emission. This again suggests that negative particles leaving the specimen result in an increase of positive charge on its surface. The periodic repetition of the charge signal and its negative peaks may be caused by the non-uniformity of the surface due to wear and by the fact that the glass specimens used in these experiments were not made from a uniform single crystal but were instead amorphous materials containing random defects [257, 337]. These charge measurements agree well with recent studies about the non-uniformity of the charge of the surface during contact [42], the transfer and re-transfer of electrons and the transfer of material between the surfaces in contact [255, 338].

Charge and emission measurement during sliding test with fracture

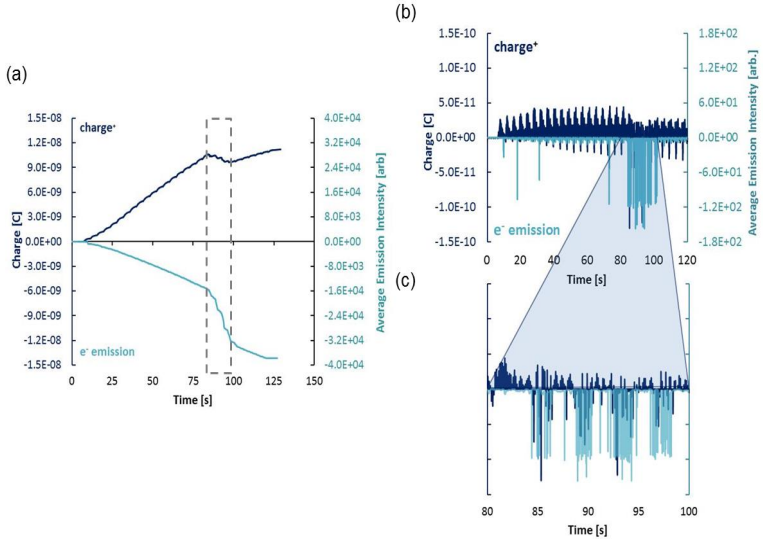

Figure 6.4: (a) Average intensity of each phosphor screen image and surface charge *vs.* time (cumulative values); (b) Average intensity of each phosphor screen image and surface charge vs. time (instantaneous values), (c) Zoom of the period between 80 s and 100 s, during sliding test with fracture

In tests when fractures were observed on the sliding surface, the comparison between surface

charge and the average intensity of the emission reveals a different trend. Figure 6.4a shows the accumulation of charge on the surface and the cumulative average emission intensity of each phosphor screen images as a function of time. Initially, as expected, the surface charges positively due to the emission of negative particles. However, in the period between $\sim 80\,\mathrm{s}$ and $\sim 100\,\mathrm{s}$, the sudden increase of the emission results in the abrupt drop of the charge suggesting an inversion of the surface charging. When comparing the instantaneous values of the charge of the surface with the instantaneous values of the emission intensity during fracture (Figure 6.4(c)) a correspondence between peaks of negative charge and peaks of negative emission can be noticed. This suggests that, unlike the case of sliding without fractures, even if significant negative emission is detected, the particles escaping the surface during fracture are mainly positively charged. This causes the negative charging of the silica surface, in contrast with the triboelectric series predictions. To analyze the cause of this unexpected change of emission intensity, the phosphor screen images were evaluated. During the highlighted period of Figure 6.4, the phosphor screen revealed emission events of different intensity, shape and size compare to the emission events recorded at the beginning (Figure 6.5a) and at the end (Figure 6.5c) of the test. An example of these images is shown in (Figure 6.5b). The events are brighter and extensive. The subsequent scans of the surface, an example of which is reported in (Figure 6.5e) showed fractures at the areas where this type of emission was detected, suggesting that high emission intensity events occur at the moment when the tip causes fracture of the surface.

The analysis of the wear track in case of fracture reports an average depth and width of $14\,\mu\mathrm{m}$ and $89.87\,\mu\mathrm{m}$, respectively which is, indeed, significantly higher than the depth and width of the wear track in case of sliding without fracture ($\sim 0.19\,\mu\mathrm{m}$ and $\sim 36\,\mu\mathrm{m}$, respectively).

The experimental outcomes show that the emission of negative particles due to the rubbing contributes to the positive charging of the silica specimen. Conversely, during the occurrence of fracture, the emission generated causes the silica to charge more negatively, suggesting that this emission consists mainly of positive particles. Overall, it can be suggested that both tribocharging and triboemission are influenced by the wear and that the emission of charged particles influences the charging of the surface.

6.3.2 Theoretical Outcomes

In both the experimental tests reported above silica specimens have been subjected to conduct-induced electrification. The contribution of this is here investigated theoretically by examining the difference of charge density at the interface. This is calculated via equation 3.2.

Figure 6.6a,b shows such charge-density differences at the interface between C(111) and amorphous SiO_2, respectively. It can be noticed a significant electron charge accumulation at

the C(111) side of the interface which results in a loss of electron charge at amorphous SiO_2 interface side. To observe how the charge is displaced across the interface, the charge-density difference is integrated in the xy planar dimensions. The resulting $\rho_{diff}(z) = \int \rho_{diff}\,\mathrm{dxdy}$ along the z axis is shown in Figure 6.6c for a limited region around the interface, where the zero indicates the diamond surface. This shows a significant depletion at the silica interface side and a transfer of charge towards the diamond slab.

This analysis supports the outcomes of the sliding test reported in the previous sections. In particular, it confirms that, also at atomic level, silica loses electrons, *i.e.* charges positively, when in contact with diamond. Moreover, it gives insights into the electronic properties of contact-induced electrification. The influence of the sliding to the charge transfer was simulated by separating the two slabs using discrete steps of 0.1 Å, starting from the equilibrium configuration. The comparison of the integrated charge density difference at the interface between three different slab heights (22.25 Å (equilibrium), 23.25 Å and 24.25 Å), the total charge of the silica slab and the binding energy between the C(111) slab and SiO_2 slab during the separation are reported in figure 6.7a,b,c, respectively.

The comparison of the charge density difference (Figure 6.7a) shows that the separation of the C(111) slab from the amorphous SiO2 slab results in an higher transfer of electrons from the silica slab to the diamond slab compare to the equilibrium configuration. In support of this, the calculation of the Bader charges [191–194] of the $SiO:2$ slab reports a decrease of the total charge with the increase of slab height (Figure 6.7b). This is in agreement with the experimental outcomes which show an accumulation of positive charge on silica specimens over the time.

The evaluation of the binding energy between the two slabs shows a decrease of energy with the increment of the slab height (Figure 6.7c). This is consistent with the analysis of the bond lengths of the atoms at the interface which reports a significant stretch compare to the equilibrium configuration. On average, Si-O bond length in the last step is of about 1.86 Å thus 0.18 Å longer than the bond length at the equilibrium; instead C-C bond length is of about 1.65 Å, 0.08 Å longer than the equilibrium length. Also for the C-Si and C-O bond a stretch of 0.38 Å and 0.04 Å is calculated, respectively. The elongation of the Si-O and C-Si bonds favors the transfer of the charge from the C(111) slab to the $SiO:2$ slab, which is in agreement with the charge density difference shown in Figure 6.7a. The reduction of the binding energy and the stretching of the bond lengths might also promote the escape of some of the electrons located at the interface. Moreover, the significant elongation of the Si-O bond lengths suggests a probable break of the bonds and a consequent removal of silica layers from the silica slab. This will give addition information about the mechanism behind tribocharging, in particular about the role of material transfer and how this affects the charge of the surface.

6.4 Conclusions

The study here reported gives insight into the mechanisms behind tribocharging. Results of the influence of the emission of charged particle due to the rubbing and results of the influence of contact-induced electrification are obtained by a combined experimental and theoretical approach. Sliding tests on silica specimens rubbed with a diamond tip carried out by using a unique in-house built tribometer, showed that silica specimens charge positively during the sliding in case no fractures occur. In particular, the linearity between the positive charging of the silica and the emission of negative charges showed that the silica charges more positively as more electrons leave the surface. Contrarily, if fracture occurs the surface charged negatively, suggesting the emission of positive charged particles. Overall, the experimental outcomes showed that the surface is subjected to a non-uniformity of the charging which is due to the type of wear and the structure of the material.

The contribution of the contact-induced electrification to the charging of the surface was evaluated by employing first-principles methods. The transfer of electron charge from the amorphous SiO_2 slab to the C(111) slab was clearly shown by the analysis of the charge density difference at the interface. The isosurfaces showed the accumulation of charge at the C(111) slab interface and the loss of charge at SiO_2 slab interface. The transfer charge analysis of the simulated sliding showed, in agreement with the experimental outcomes, an increase of the transfer of the charge from the SiO_2 slab to the C(111) slab with the increase of the slab height. This was supported by the Bader charge analysis which resulted in a reduction of the total charge of the silica slab, the reduction of the binding energy between the two slabs and the elongation at the interface of the Si-O and C-Si bond lengths. This last outcome, in particular, suggested the possibility of breaking of the bonds and material transfer from the silica to the diamond surface.

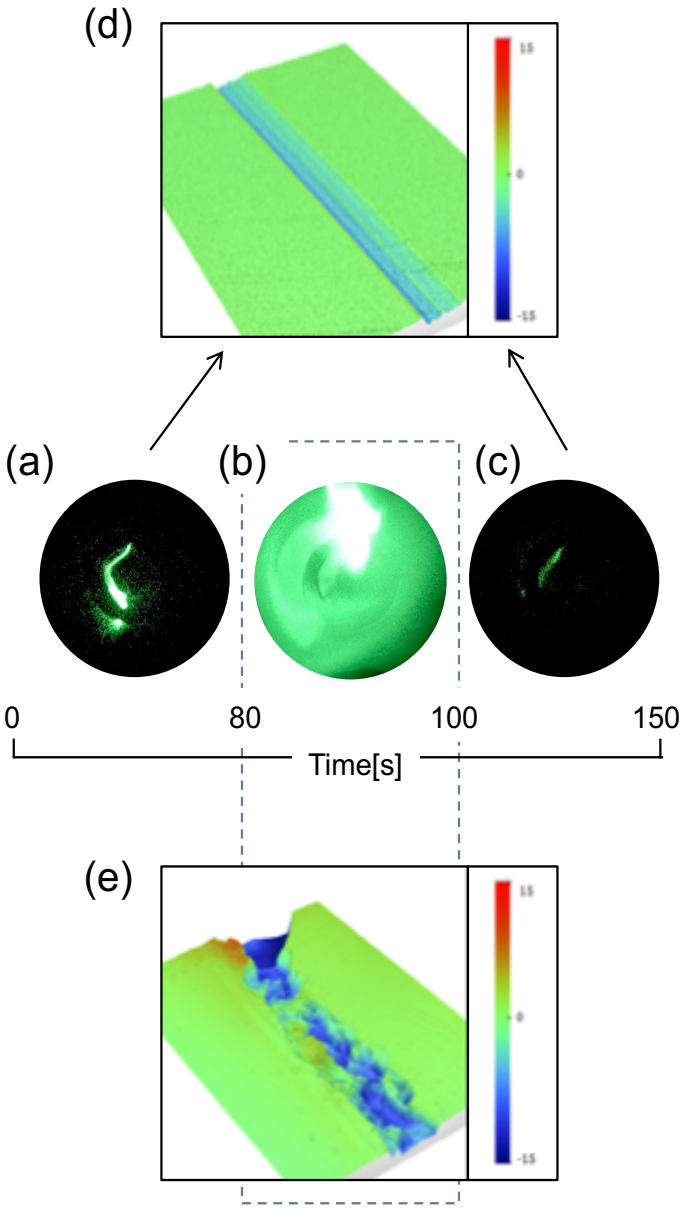

Figure 6.5: Triboemission events (a) at the beginning, (b) during fracture and (c) at the end of the test; White Light Interferometry (WLI)WLI scan of the surface at (d) rubbing area (e) at fracture area.

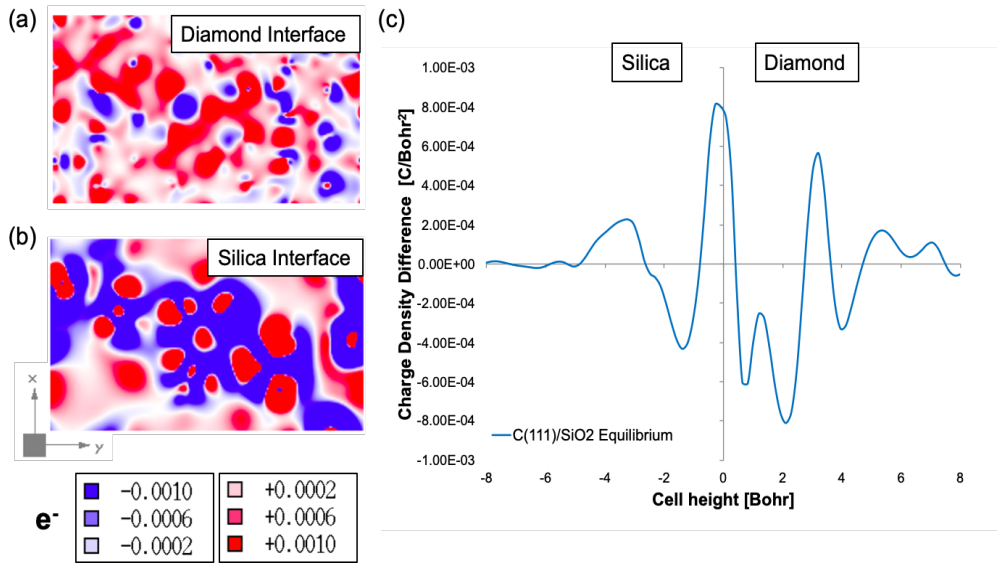

Figure 6.6: Charge density difference isosurfaces at (a) C(111) interface and at (b) amorphous SiO_2 interface; (c) Integrated charge-density difference along cell height.

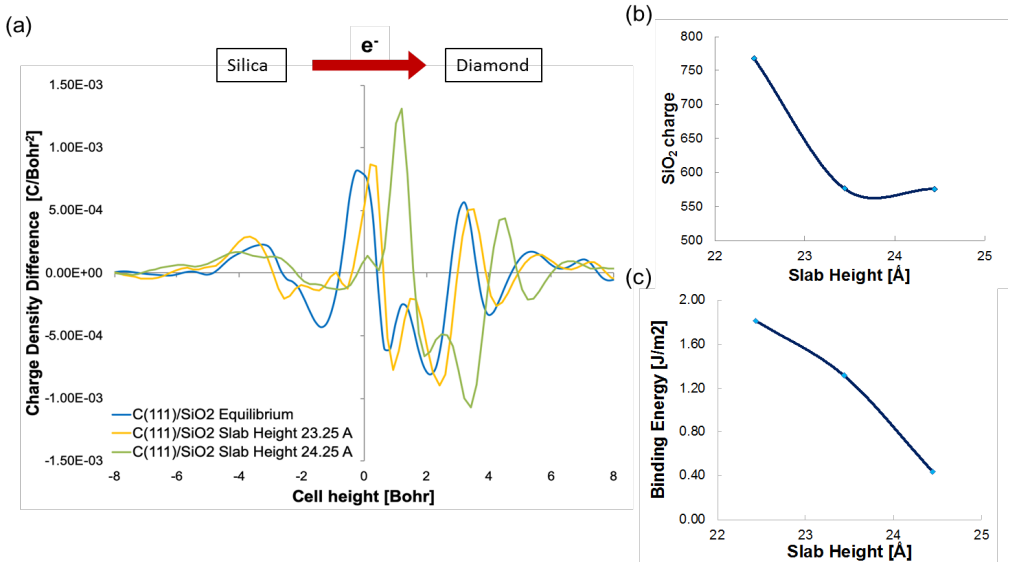

Figure 6.7: (a) Integrated charge-density difference along the cell height for free different slab heights; (b) Bader charge measurements of SiO_2 slab *vs* slab height; (c) Binding energy between C(111) slab and SiO_2 slab *vs* slab height.

Chapter 7

Concluding remarks

The aim of this thesis is to provide insights into three different problems related to the microscopic understanding of frictional phenomena, by means of first principles DFT calculations: Part I is devoted to the study of the effects of surface chemical modification on adhesive friction; in Part II describes how tribochemical reactions can convert hydrocarbon molecules into graphitic films ; Part III is focused on the microscopic mechanisms of charge transfer and triboelectrification.

The main results are summarized in the following:

- Phosphorus is the main functional element of many lubricant additives, its presence at iron surfaces is critical for a range of tribological processes and applications. However, phosphorus adsorption on iron had never been studied experimentally or theoretically. In chapter 2 we study the adsorption of phosphorus on Fe(100), the most stable iron surface. A systematic comparison among P, S, N, and O uncovers a peculiar behavior of the P and S species: attractive adatom-adatom interaction at high coverage lead to the formation of two-dimensional overlayers that reduce the metal reactivity and work function. This effect is important in iron embrittlement and especially for the functionality of P- and S-containing additives included in lubricant oils. These results have been described in the following article:

  Fatti, G., Restuccia, P., Calandra, C., & Righi, M. C. (2018). *Phosphorus adsorption on Fe (110): An ab initio comparative study of iron passivation by different adsorbates.* The Journal of Physical Chemistry C, 122(49), 28105-28112.

- In chapter 3 we take advantage of these findings to predict for the first time to out knowledge that selenium can effectively lubricate iron/iron interfaces. The adsorption properties of Se on the most stable iron surface are studied and the metal-adsorbate interaction are characterized, and the tribological properties of the Fe-Se/Se-Fe interface

are investigated and compared to those of Fe-P/P-Fe and Fe-S/S-Fe interfaces. The charge rearrangement at the interface and the density of states reveals the formation of strong covalent interaction network inside the Se adsorbed layer that weaken the metal-metal interaction, providing superior lubricating properties than P and S. This work has been presented in the following article:

Fatti, G., & Righi, M. C. (2019). *Selenium Chemisorption Makes Iron Surfaces Slippery.* Tribology Letters, 67(4), 125.

- The calculation of ideal shear strengths and adhesion of solid interfaces has been implemented in a workflow for high-throughput screening, which has been described in the following paper:

  Restuccia, P., Levita, G., Wolloch, M., Losi, G., Fatti, G., Ferrario, M., & Righi, M. C. (2018). *Ideal adhesive and shear strengths of solid interfaces: A high throughput ab initio approach.* Computational Materials Science, 154, 517-529.

- Recent experiments performed at the Argonne National Laboratory demonstrated that the tribochemical conversion of methane to graphene, nano-onion, and disordered carbons on the sliding surfaces of Ni provides two to three orders of magnitude reduction in wear and $\sim$ 50% reduction in friction compared to those of the uncoated steels. By means of *ab-initio* molecular dynamics simulations we elucidate the mechanisms involved in the tribochemical conversion of methane to carbon-based nanostructures. The simulations show that the conversion of CH_4 to 2D graphene and nano-onions occurs by a catalytic process involving first the dehydrogenation of methane on Ni followed up by the formation of an amorphous carbon-chains network of low atomic density. Under the influence of high contact pressure and shear forces, the amorphous carbon network sandwiched between the Ni surfaces undergoes rehybridization and subsequent conversion to graphene-like planar structures. The work has been described in the following article:

  Ramirez, G., Eryilmaz, O., Fatti, G., Righi, M.C., Wen, J., & Erdemir A. *Tribochemical Conversion of Methane to Graphene and Other Carbon Nanostructures on Sliding Surfaces.*, submitted to Materials Today Nano

- Polytetrafluoroethylene (PTFE), commercially known as Teflon, is one the most effective insulating polymers for triboelectric applications, due to its capability to acquire, retain and eventually re-supply negative charge. . In chapter 5 we study the electronic properties of the high-pressure phase of PTFE, as triboelectric technologies are usually subjected to high pressure. We explain the capability of PTFE to attract negative charge by showing its electronic states. In particular the charge distribution of the lowest conduction band

is delocalized along the entire length of the chain. The intra-chain character of charge distribution reported here suggests that PTFE has the ability to acquire negative charge.

This work has been described in the article:

Fatti, G., Righi, M. C., Dini, D., & Ciniero, A. (2019). *First-Principles Insights into the Structural and Electronic Properties of Polytetrafluoroethylene in Its High-Pressure Phase (Form III).* The Journal of Physical Chemistry C, 123(10), 6250-6255.

- In chapter 6 we study the contact electrification occurring in a diamond-silica rubbing experiment mediated by charge emissions. By means of a unique vacuum measurement system that enables to measure surface charge variations while simultaneously recording triboemission events during the sliding of a diamond tip on silica specimens,the tribocharging and triboemission behavior are linked and analyzed in relation to the surface wear. *Ab-initio* simulations describe the contribution of contact-induced electrification to the charging of the surface. The transfer charge analysis of the simulated sliding showed, in agreement with the experimental outcomes, an increase of the transfer of the charge from the SiO_2 slab to the C(111) slab with the increase of the slab-slab separation. The charge transfers increases with the reduction of the binding energy between the two slabs and the elongation of the interface bonds. This last outcome confirms that material and charge transfer are strictly related. This work has been presented in the following paper:

  Ciniero, A., Fatti, G., Righi, M. C., Dini, D., & Reddyhoff, T. (2019). *A Combined Experimental and Theoretical Study on the Mechanisms Behind Tribocharging Phenomenon and the Influence of Triboemission.* Tribology Online, 14(5), 367-374.

Future perspectives

- In the first part we identify the key electronic properties of a passivating overlayer that provide lubrication, uncovering in hid way the origin of the good tribological performance of sulfur and phosphorus, which are elements commonly used in commercial lubricant additives. Selenium is proposed for the first time as an efficient alternative in a possible new lubricant additive. The study is focused on iron surfaces and on selected adsorbates. The next step would be to generalize the systematic study to different surfaces, materials and adsorbates. This may be achieved by implementing an high-throughput approach that would allow to screen the highest possible number of substrate materials and adsorbed elements.

- In the second part we show that it is possible to obtain self-replenishing carbon nanocoatings from the tribocatalytic conversion of methane at nickel sliding surfaces. The study might be developed by *i*) generalizing to different hydrocarbon molecules; *ii*) determining what physical conditions favor the dehydrogenation of hydrocarbons, in order to provide a better understanding of the tribochemical processes. For example, it would be interesting to understand the role played by normal forces and shear forces separately, by molecule concentration and by confinement. Moreover, a deeper characterization of the electronic states would add valuable insight to the tribochemical process.

- In the third part of the thesis we investigate the microscopic mechanisms of triboelectric charging in polymers and insulators. As we have seen in the introduction this is a complex phenomenon, governed by competing dynamical processes. In chapter 5 we have focused on the inherent electronic properties of polytetrafluoroethylene, finding a spatial configuration of the valence and conduction states coherent with its well known ability to retain negative charge. We plan to extend the study to actual PTFE surfaces, exploring the role of possible surface states and defect states as well as the interaction with different materials.

- In chapter 6 we have seen that in diamond-silica contact, the material transferred from amorphous silica to crystalline diamond is critical in the triboelectric charging of the two surfaces. We obtain this result, for the first time for an amorphous materials, analyzing how the charge density changes while the two surfaces in contact are separated quasi-statically. Further insights may be achieved applying the same quasi-static approach also to lateral motion, so to understand the role of the shear forces.

Appendices

Appendix A

Tribocatalytic extraction of graphene: additional experimental and computational details

A.1 Experimental Details

A.1.1 Coating Characterization

We characterize the coating in terms of its chemical and structural composition and of its mechanical properties. Figure A.1 shows the typical XRD spectrum of the VN-Ni coating, revealing the characteristic peaks for the presence of cubic (rock-salt) VN and cubic (bcc) V. The peaks corresponding to pure vanadium are due to the bonding layer made of V that was used to improve the adhesion of the coating to the substrates. The presence of nickel is not obvious in the XRD spectrum, probably due to overlapping of peaks or to the small amount that is contained within the coating.

Figure A.2 shows the hardness (Figure A.2a) and elastic modulus (Figure A.2b) profiles of the VN-Ni coating. On the average, this coating exhibited a hardness value of about $\sim 18\,\mathrm{GPa}$, and an elastic modulus of about $\sim 220\,\mathrm{GPa}$. The surface roughness of the coatings is measured in the range of 20 to 50 nm.

Finally, low magnification cross-sectional TEM image (Figure A.3a) shows a film thickness of 500 nm. The HRTEM image in Figure A.3b shows that the film consists of nanometer scale grains with lattice spacings corresponding to Ni and VN.

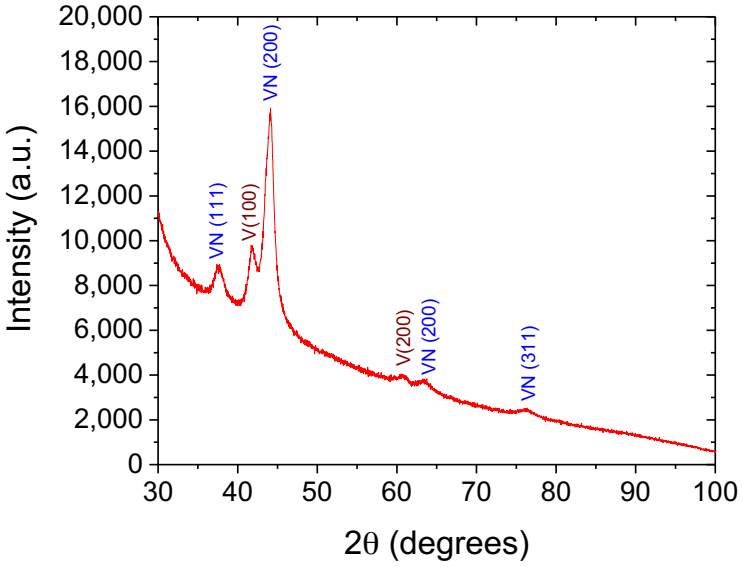

Figure A.1: X-ray diffraction patterns of the VN-Ni coating, showing the presence of vanadium nitride and the vanadium bond layer.

A.1.2 Tribological characterization

Friction and wear tests were carried out in methane (at 0.9 atm) using a high-vacuum tribometer, in which a stationary steel ball (9.5 mm in diameter) was pressed against a rotating disc as depicted in Figure 4.1a under a peak Hertz pressure of 0.6 GPa at a sliding velocity of 0.1 m/s for a distance of 360 m. The wear volumes on the ball and disc samples were assessed with the help of optical microscopy; specifically, the wear scars and tracks (see Figure 4.1) were imaged by an Olympus STM6 microscope. The amount of wear was calculated by the following wear volume equation based on the wear scar diameter measured by the microscope:

$$V = \frac{\pi h}{6}\left(\frac{3d^2}{4} + h^2\right), \tag{A.1}$$

where d is the wear scar diameter, r is the radius of the ball and h is given by the equation:

$$h = r - \sqrt{r^2 - \frac{d^2}{4}}. \tag{A.2}$$

A.1.3 Tribofilm characterization

The debris particle generated during the sliding are characterized by HRTEM. The first type of debris consists of a large graphene sheet and nano-onions. The HRTEM image in Figure A.4 shows a hexagonal lattice of graphene. Due to the curving of graphene sheets at their edge, the layer number can be directly imaged by HRTEM. Figure A.4b shows one layer of curved

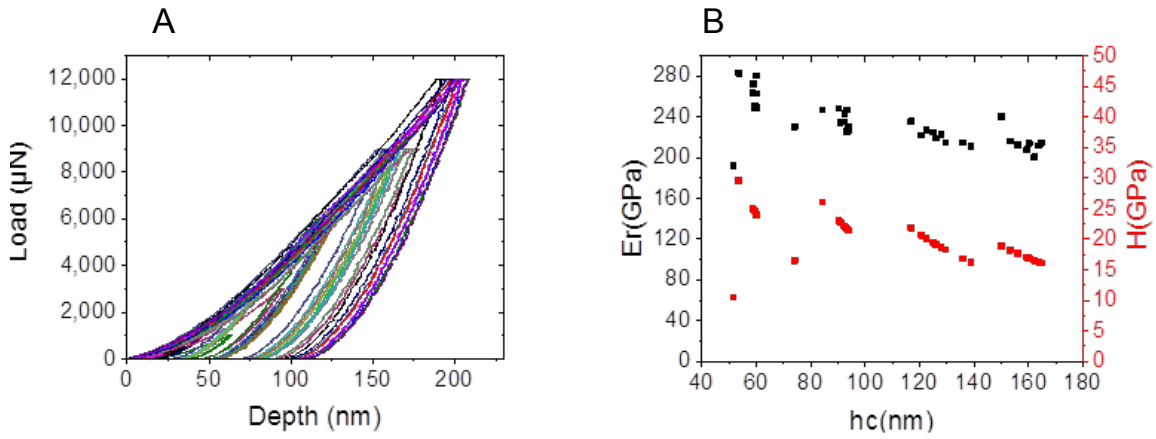

Figure A.2: Nano-indentation results from the VN-Ni coating. (a) Loading/unloading curves for the measurements using loads between 500 N and 12,000 N. (b) Hardness and Elastic Modulus as a function of the penetration.

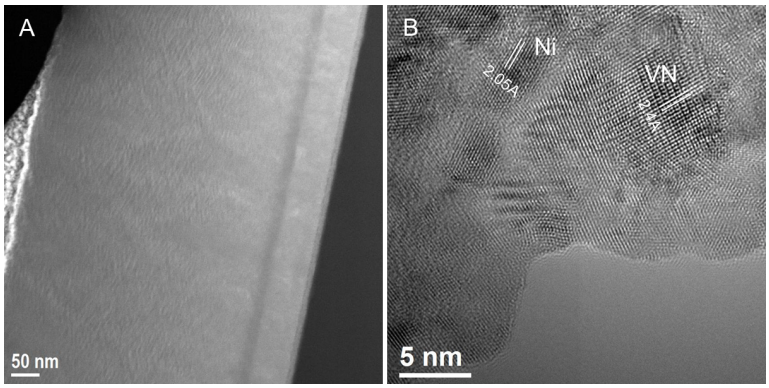

Figure A.3: (a) Low and (b) high-resolution cross-sectional TEM images showing the structural morphology of the VN-Ni film

graphene sheet, indicated by the arrow head. The layer number of graphene sheets could range from one layer to several layers. In addition to the carbon nano-onions shown in Figure 4.2, we also observed other types of carbon nanostructures, shown in Figure A.4c. EELS spectra (Figure A.4d-f) from Figure A.4a indicate that the carbon material has mainly a graphitic structure as featured by the sharp π-peak. A small amount of oxygen (Figure A.4e) absorbed on the surface of graphene is also observed, as are small amounts of Fe and V, acting as a catalyst for the growth of graphene. No noticeable amount of nitrogen is observed in these carbon materials.

The HRTEM images show that all nanoparticles in the second type of debris are wrapped by highly disordered graphitic carbon (Figure A.5). When the graphitic carbon fragment is edge-on (view from the side of a graphene fragment), a string of bright dots is observed with a lattice

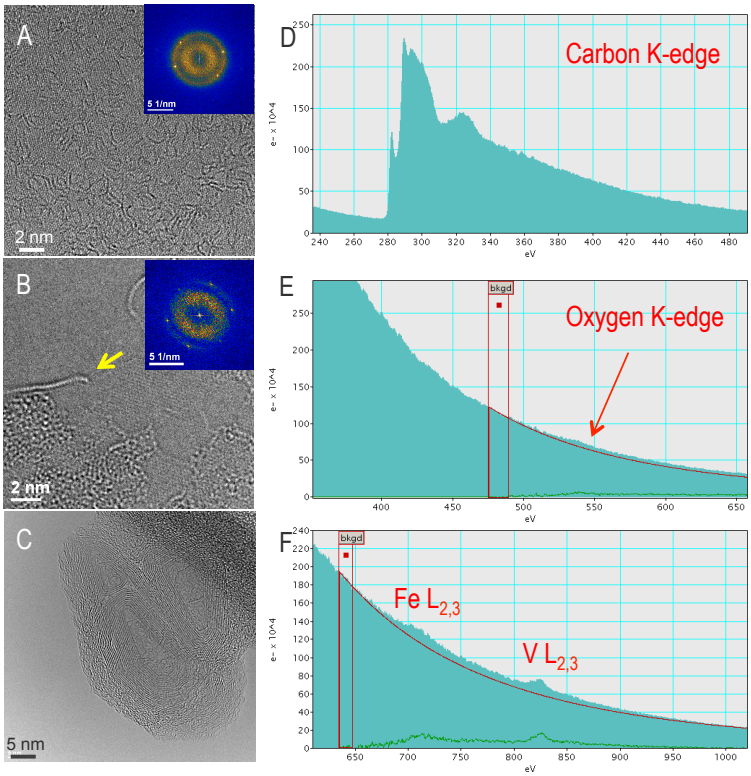

Figure A.4: (a) Low and (b) high-resolution cross-sectional TEM images showing the structural morphology of the VN-Ni film

spacing of 0.21 nm, corresponding to (10-10) lattice spacing of graphene. When graphitization is high, graphene fragments are stacked with 0.33 nm lattice spacing, corresponding to (0001) lattice spacing of graphite. The lattice spacing can vary from 0.33 nm to 0.37 nm, depending on the degree of graphitization. These highly disordered graphitic carbons actually consist of nanoscale-defected graphene fragments connected with disordered carbon, which is different from amorphous carbon (or diamond-like carbon).

The agglomerated debris consists of many nanoparticles, as shown in the high-angle annular dark-field image (Figure A.6a). Since the intensity in the high angle annular dark field (HAADF) image is roughly proportional to Z^2, it is also called the Z-contrast image. The nanoparticles shown in Figure A.6 have average size of about 5 nm. The EDS spectrum (Figure A.6c) from a large area of 100 nm in diameter shows that the agglomerated debris consists of Co, O, V, Ni, Fe, and Si with atomic ratio shown in the upper row in Figure A.6d. Since the agglomerated debris was generated in a reduced environment, oxidation of metallic nanoparticles must happen after exposure to air. By removing the contribution of oxygen, we found that the agglomerated debris consists of about 70% carbon, shown in the lower row in Figure A.6d. The EDS mapping in Figure A.6b shows a strong carbon signal at the edge of the agglomerated debris, indicating that the nanoparticles are wrapped by carbon.

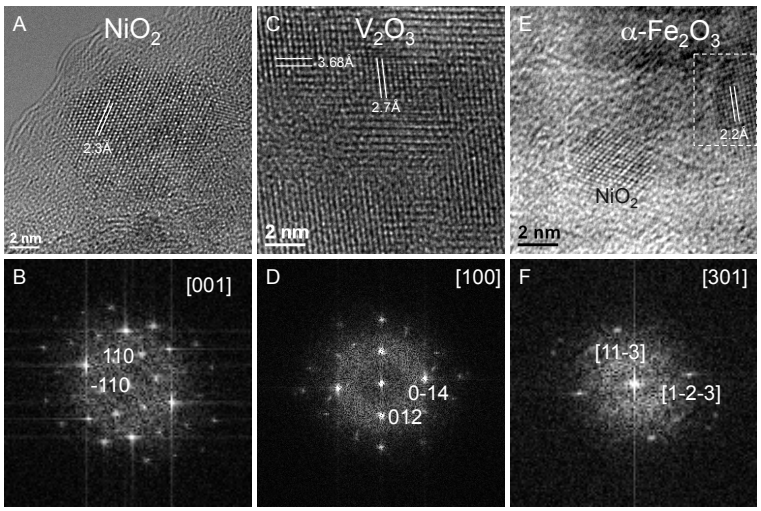

Figure A.5: (a) Low and (b) high-resolution cross-sectional TEM images showing the structural morphology of the VN-Ni film

The agglomerated debris consists of nanoparticles and disordered carbon. EELS was applied to study the $sp^2/(sp^2 + sp^3$ ratio in the disordered carbon. The carbon K-edge EELS spectrum consists of two features, a peak at 285 eV due to excitation to $p\pi^*$ states of sp^2-bonded carbon and a step at 290 eV due to excitation to $p\sigma^*$ states of sp^3 and sp^2 sites [339]. Thus, pure 100% sp^2 carbon phase, such as highly oriented pyrolytic graphite (HOPG), possess the strongest peak at 285 eV, whereas pure 100% sp^3 carbon diamond has no peak at 285 eV. The sp^2 fraction of a carbon film can be calculated by taking the ratio of the area of the 285 eV peak to the area of the 290 eV step within the energy window of 280 - 540 eV, and comparing it to the ratio of the 100% sp^2 HOPG reference [340]. However, the intensity of pre-peak at 285 eV depends on HOPG orientation strongly. Instead of HOPG, we chose glassy carbon (Figure A.7a) as reference since glassy carbon has a high sp^2 ratio, and the grains are randomly oriented. The $sp^2/(sp^2 + sp^3)$ ratio of the disordered carbon (Figure A.7d) is measured as 58% with an error of 2%. The EELS spectra for the first type of debris graphene and amorphous carbon from TEM grid are also shown in Figure A.72.

A.2 Computational details

We compare the catalytic ability of Ni and VN by calculating the reaction energies for methane dissociation on the most stable surfaces of the two materials, namely, the Ni(111) and VN(100). To this aim, we first identified the most favorable adsorption configuration of the dissociated molecule. We, thus, studied the adsorption of C and H atoms by comparing the adsorption in the high symmetry sites represented in Figure A.8. The adsorption energy is calculated as

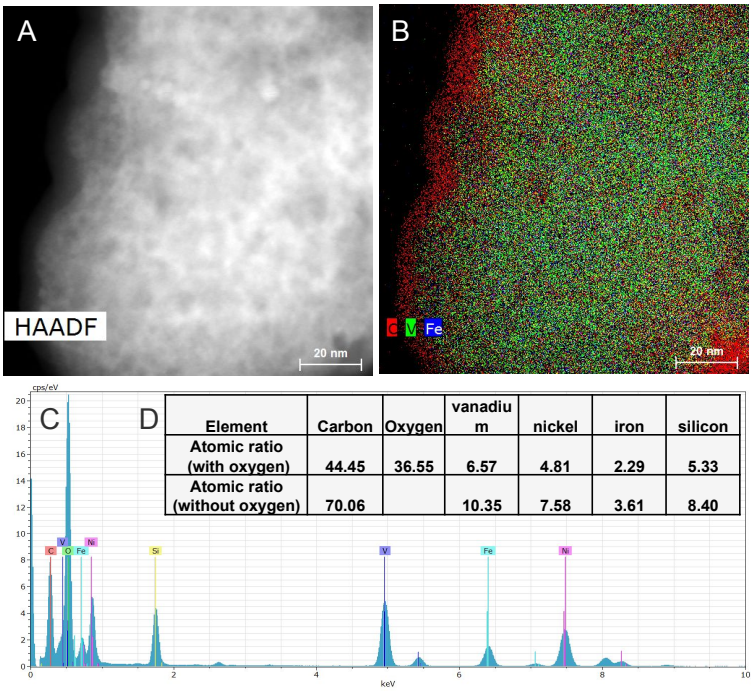

Element	Carbon	Oxygen	vanadium	nickel	iron	silicon
Atomic ratio (with oxygen)	44.45	36.55	6.57	4.81	2.29	5.33
Atomic ratio (without oxygen)	70.06		10.35	7.58	3.61	8.40

Figure A.6: (a) HAADF image and (b) EDS mapping of the agglomerated debris. (c) EDS spectrum from an area of 100 nm in diameter. (d) Atomic ratio with and without considering oxygen.

$E_{ad} = E_{sur+a} - E_{surf} - E_a$, where E_{sur+a} is the energy of the adsorbate system, E_{surf} is the energy of the clean surface, and E_a is the energy of the isolated atom.

The calculated adsorption energies are reported in Table A.1 and the optimized adsorption configurations at the most favorable sites are displayed in Figure A.9. It is known from the literature that both C and H adsorb at three-fold hollow sites on Ni(111) [236–238, 244, 248–250].

surface	adsorption site	Carbon E_{ads} (eV)	Hydrogen E_{ads} (eV)
Ni(111)	fcc hollow	-7.64	-2.92
	hcp hollow	-7.73	-3.75
VN(100)	V on top	-2.23	-1.74
	N on top	-4.45	-1.94
	bridge	-5.61	-1.38
	hollow	-4.23	-1.21

Table A.1: Calculated adsorption energies for C and H atoms at Ni(111) and VN(100) surfaces. The most favorable adsorption energies were used to compute the molecule dissociation energy.

Methane is an extremely stable molecule, since its electronic structure resembles that of a noble-gas atom. Methane weakly physisorbs on Ni(111), with a physisorption energy of

$\sim 0.02\,\text{eV}$, while it does not show any attraction by the VN(100) surface. We calculated the reaction energy for molecular dissociation on the surface as $E_R = E_{surf+C+4H} - E_{surf+CH_4}$, where $E_{surf+C+4H}$ is the energy of the fully dissociated molecule and $E_{surf+CH_4}$ is the energy of a physisorbed (or fluctuating) molecule on the surface. The energy of the final state, $E_{surf+C+4H}$, was calculated by assuming the adsorbed C and H atoms at large separation, i.e., neglecting adatom-adatom interactions. The obtained value are $E_R = 0.02\,\text{eV}$ and $E_R = 0.89\,\text{eV}$ for Ni (111) and VN (100), respectively. The positive sign of E_R indicates that molecular dissociation is an endothermic reaction on both the substrates. However, at the extreme conditions present in tribological contact, where the estimated temperature is equal to about 1000 K and strong mechanical stresses are applied, endothermic processes can be expected to occur. The lower energy cost of methane dissociation on Ni highlights its better catalytic action than VN. Therefore, we focused our *ab initio* molecular dynamics simulations on Ni interfaces.

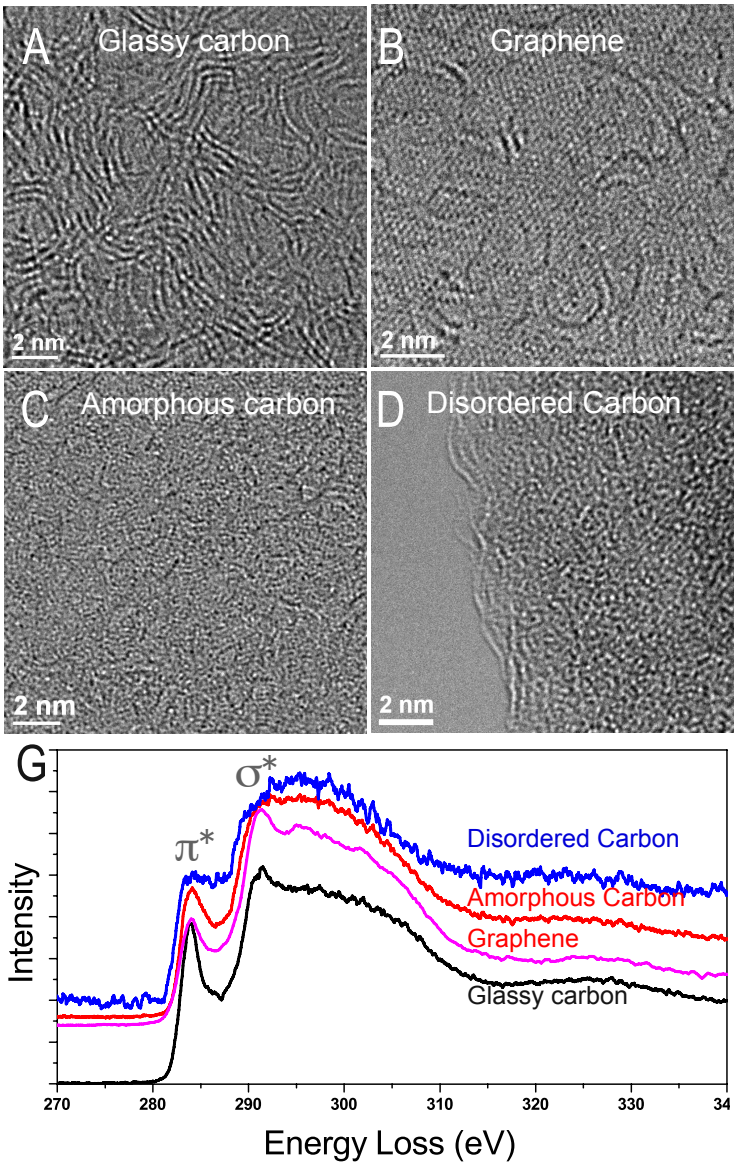

Figure A.7: HRTEM images of (a) glassy carbon, (b) graphene, (c) amorphous carbon, and (d) disordered carbon. (e) EELS spectra from corresponding samples.

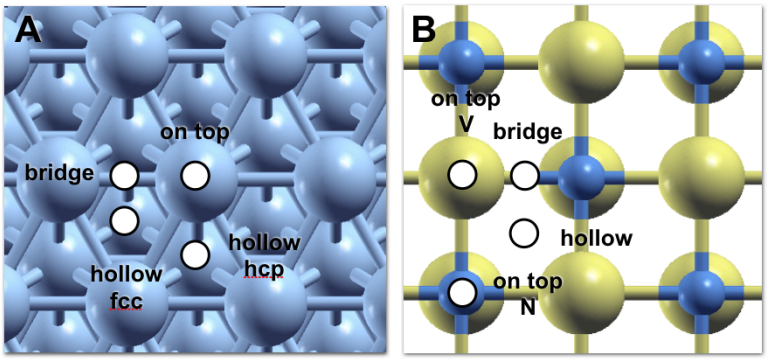

Figure A.8: High symmetry sites on Ni (111) (a) and VN (100) (b) surfaces.

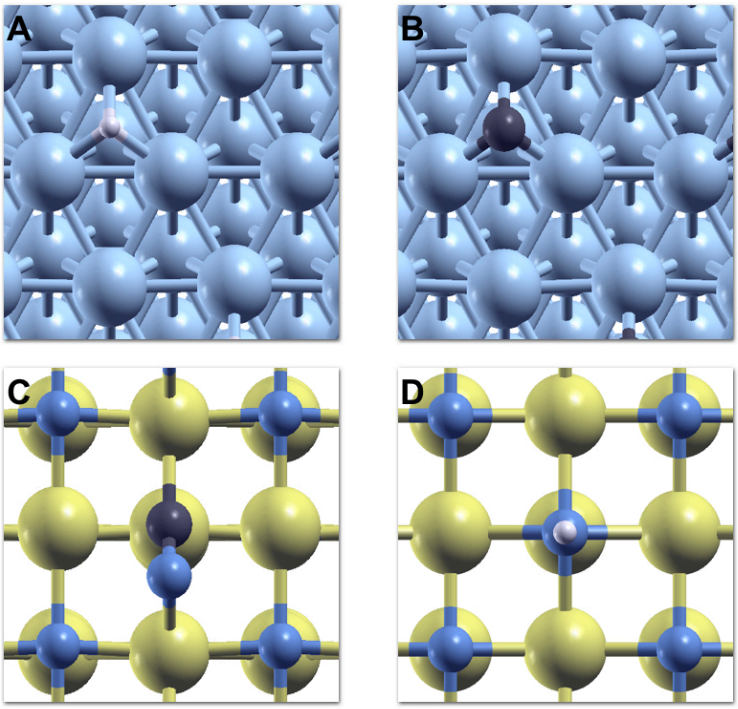

Figure A.9: High symmetry sites on Ni (111) (a) and VN (100) (b) surfaces.

Acknowledgments

I would like to thank my supervisor Prof. Maria Clelia Righi, for her guidance during the challenging but satisfying years of this PhD. I am also grateful to Prof. Carlo Calandra for sharing his exceptional knowledge, always with amazing kindness. Thanks to him I am certainly a better scientist.

Thanks to all the members of the group, Paolo, Stefan, Michael and Gabriele, who have been valuable collaborators and more importantly good friends. Thanks also to my officemates, Matteo, Maurizio and especially Giulia. The time spent in that office would have often been unbearable without our brilliant scientific discussion about football and politics. Thanks to Celeste, Jacopo and Ale, for the nights, the laughters, the support. In one word, for their friendship, in Modena and in London.

Last, but not least, I would like to thank Arianna, who will not need words to understand.

Bibliography

[1] K. Holmberg and A. Erdemir, Fme Trans **43**, 181 (2015).

[2] K. Holmberg and A. Erdemir, Friction **5**, 263 (2017), ISSN 2223-7704, URL https://doi.org/10.1007/s40544-017-0183-5.

[3] M. Dienwiebel, G. S. Verhoeven, N. Pradeep, J. W. M. Frenken, J. A. Heimberg, and H. W. Zandbergen, Phys. Rev. Lett. **92**, 126101 (2004), URL https://link.aps.org/doi/10.1103/PhysRevLett.92.126101.

[4] A. Erdemir and O. Eryilmaz, Friction **2**, 140 (2014), ISSN 2223-7704, URL https://doi.org/10.1007/s40544-014-0055-1.

[5] S. Kawai, A. Benassi, E. Gnecco, H. Söde, R. Pawlak, X. Feng, K. Müllen, D. Passerone, C. A. Pignedoli, P. Ruffieux, et al., Science **351**, 957 (2016), ISSN 0036-8075, https://science.sciencemag.org/content/351/6276/957.full.pdf, URL https://science.sciencemag.org/content/351/6276/957.

[6] J. Bae, J. Lee, S. Kim, J. Ha, B.-S. Lee, Y. Park, C. Choong, J.-B. Kim, Z. Wang, and H.-Y. e. Kim, Nature communications **5**, 4929 (2014), URL https://doi.org/10.1038/ncomms5929.

[7] Z. L. Wang, ACS Nano **7**, 9533 (2013), pMID: 24079963, https://doi.org/10.1021/nn404614z, URL https://doi.org/10.1021/nn404614z.

[8] Y. Su, J. Chen, Z. Wu, and Y. Jiang, Applied Physics Letters **106**, 013114 (2015).

[9] H. Watanabe, M. Ghadiri, T. Matsuyama, Y. L. Ding, K. G. Pitt, H. Maruyama, S. Matsusaka, and H. Masuda, International Journal of Pharmaceutics **334**, 149 (2007), ISSN 0378-5173, URL http://www.sciencedirect.com/science/article/pii/S0378517306009513.

[10] Y. Pu, M. Mazumder, and C. Cooney, Journal of Pharmaceutical Sciences **98**, 2412 (2009), ISSN 0022-3549, URL http://www.sciencedirect.com/science/article/pii/S0022354916330106.

[11] S. Karner and N. Urbanetz, Journal of Aerosol Science **42**, 428 (2011), ISSN 0021-8502, URL http://www.sciencedirect.com/science/article/pii/S0021850211000383.

[12] C. Coulomb, *Théorie des machines simples en ayant égard au frottement de leurs parties et à la roideur de leurs cordages* (Bachelier, Librairie, quai des Augustins, Paris, 1785).

[13] E. Andablo-Reyes, R. Hidalgo-Alvarez, and J. de Vicente, Soft Matter **7**, 880 (2011), URL http://dx.doi.org/10.1039/C0SM00251H.

[14] F. Bowden and D. Tabor, *The friction and lubrication of solids* (Clarendon Press, London, UK, 1964).

[15] D. Tabor and R. H. S. Winterton, Proceedings of the Royal Society of London. A. Mathematical and Physical Sciences **312**, 435 (1969), https://royalsocietypublishing.org/doi/pdf/10.1098/rspa.1969.0169, URL https://royalsocietypublishing.org/doi/abs/10.1098/rspa.1969.0169.

[16] J. N. Israelachvili and D. Tabor, Proceedings of the Royal Society of London. A. Mathematical and Physical Sciences **331**, 19 (1972), https://royalsocietypublishing.org/doi/pdf/10.1098/rspa.1972.0162, URL https://royalsocietypublishing.org/doi/abs/10.1098/rspa.1972.0162.

[17] F. Hofmann and J. P. Toennies, Chemical Reviews **96**, 1307 (1996), pMID: 11848791, https://doi.org/10.1021/cr9502209, URL https://doi.org/10.1021/cr9502209.

[18] R. E. Weber and W. T. Peria, Journal of Applied Physics **38**, 4355 (1967), https://doi.org/10.1063/1.1709128, URL https://doi.org/10.1063/1.1709128.

[19] P. Palmberg and W. Peria, Surface Science **6**, 57 (1967), ISSN 0039-6028, URL http://www.sciencedirect.com/science/article/pii/0039602867900155.

[20] G. Binnig, C. F. Quate, and C. Gerber, Phys. Rev. Lett. **56**, 930 (1986), URL https://link.aps.org/doi/10.1103/PhysRevLett.56.930.

[21] R. W. Carpick and M. Salmeron, Chemical Reviews **97**, 1163 (1997), pMID: 11851446, https://doi.org/10.1021/cr960068q, URL https://doi.org/10.1021/cr960068q.

[22] I. Szlufarska, M. Chandross, and R. W. Carpick, Journal of Physics D: Applied Physics **41**, 123001 (2008), URL https://doi.org/10.1088/0022-3727/41/12/123001.

[23] C. M. Mate, G. M. McClelland, R. Erlandsson, and S. Chiang, Phys. Rev. Lett. **59**, 1942 (1987), URL https://link.aps.org/doi/10.1103/PhysRevLett.59.1942.

[24] C. Daly and J. Krim, Surface Science **368**, 49 (1996), ISSN 0039-6028, vibrations at Surfaces, URL http://www.sciencedirect.com/science/article/pii/S0039602896010278.

[25] J. Krim, Advances in Physics **61**, 155 (2012), https://doi.org/10.1080/00018732.2012.706401, URL https://doi.org/10.1080/00018732.2012.706401.

[26] B. Persson and A. Nitzan, Surface Science **367**, 261 (1996), ISSN 0039-6028, URL http://www.sciencedirect.com/science/article/pii/S003960289600814X.

[27] J. Sokoloff, Wear **167**, 59 (1993), ISSN 0043-1648, URL http://www.sciencedirect.com/science/article/pii/004316489390055Q.

[28] J. Röder, J. E. Hammerberg, B. L. Holian, and A. R. Bishop, Phys. Rev. B **57**, 2759 (1998), URL https://link.aps.org/doi/10.1103/PhysRevB.57.2759.

[29] Y. Dong, Q. Li, and A. Martini, Journal of Vacuum Science & Technology A **31**, 030801 (2013), https://doi.org/10.1116/1.4794357, URL https://doi.org/10.1116/1.4794357.

[30] G. Zilibotti, S. Corni, and M. C. Righi, Phys. Rev. Lett. **111**, 146101 (2013), URL https://link.aps.org/doi/10.1103/PhysRevLett.111.146101.

[31] M. Wolloch, G. Levita, P. Restuccia, and M. C. Righi, Phys. Rev. Lett. **121**, 026804 (2018), URL https://link.aps.org/doi/10.1103/PhysRevLett.121.026804.

[32] D. Lacks and T. Shinbrot, Nature Reviews Chemistry **3**, 465 (2019), ISSN 2397-3358, URL https://doi.org/10.1038/s41570-019-0115-1.

[33] P. Iversen and D. J. Lacks, Journal of Electrostatics **70**, 309 (2012), ISSN 0304-3886, URL http://www.sciencedirect.com/science/article/pii/S0304388612000216.

[34] W. Gilbert, *De magnete* (Courier Corporation, 1958).

[35] A. K. T. Assis, *The experimental and historical foundations of electricity* (Apeiron Montreal, 2010).

[36] P. E. Shaw and E. H. Barton, Proceedings of the Royal Society of London. Series A, Containing Papers of a Mathematical and Physical Character **94**, 16 (1917), https:

//royalsocietypublishing.org/doi/pdf/10.1098/rspa.1917.0046, URL https://royalsocietypublishing.org/doi/abs/10.1098/rspa.1917.0046.

[37] P. E. Shaw, Proceedings of the Physical Society **39**, 449 (1926), URL https://doi.org/10.1088/0959-5309/39/1/344.

[38] W. R. Harper, *Contact and frictional electrification* (Clarendon press, 1967).

[39] W. R. Salaneck, A. Paton, and D. T. Clark, Journal of Applied Physics **47**, 144 (1976), https://doi.org/10.1063/1.322306, URL https://doi.org/10.1063/1.322306.

[40] H. H. Hull, Journal of Applied Physics **20**, 1157 (1949), https://doi.org/10.1063/1.1698290, URL https://doi.org/10.1063/1.1698290.

[41] J. Lowell and A. R. Akande, Journal of Physics D: Applied Physics **21**, 125 (1988), URL https://doi.org/10.1088/0022-3727/21/1/018.

[42] H. T. Baytekin, A. Z. Patashinski, M. Branicki, B. Baytekin, S. Soh, and B. A. Grzybowski, Science **333**, 308 (2011), ISSN 0036-8075, https://science.sciencemag.org/content/333/6040/308.full.pdf, URL https://science.sciencemag.org/content/333/6040/308.

[43] V. Panella, R. Chiarello, and J. Krim, Phys. Rev. Lett. **76**, 3606 (1996), URL https://link.aps.org/doi/10.1103/PhysRevLett.76.3606.

[44] K. C. Ludema and L. Ajayi, *Friction, wear, lubrication: a textbook in tribology* (CRC press, 2018), URL https://www.taylorfrancis.com/books/9780429190490.

[45] C. Kajdas and K. Hiratsuka, Proceedings of the Institution of Mechanical Engineers, Part J: Journal of Engineering Tribology **223**, 827 (2009), https://doi.org/10.1243/13506501JET514, URL https://doi.org/10.1243/13506501JET514.

[46] S. M. Rubinstein, G. Cohen, and J. Fineberg, Nature **430**, 1005 (2004), URL https://www.nature.com/articles/nature02830.

[47] S. M. Rubinstein, G. Cohen, and J. Fineberg, Phys. Rev. Lett. **98**, 226103 (2007), URL https://link.aps.org/doi/10.1103/PhysRevLett.98.226103.

[48] O. Ben-David, S. M. Rubinstein, and J. Fineberg, Nature **463**, 76 (2010), URL https://www.nature.com/articles/nature08676.

[49] O. Ben-David, G. Cohen, and J. Fineberg, Science **330**, 211 (2010), ISSN 0036-8075, https://science.sciencemag.org/content/330/6001/211.full.pdf, URL https://science.sciencemag.org/content/330/6001/211.

[50] O. Ben-David and J. Fineberg, Phys. Rev. Lett. **106**, 254301 (2011), URL https://link.aps.org/doi/10.1103/PhysRevLett.106.254301.

[51] I. Svetlizky and J. Fineberg, Nature **509**, 205 (2014), URL https://www.nature.com/articles/nature13202.

[52] H. Spikes, Tribology Letters **17**, 469 (2004), ISSN 1573-2711, URL https://doi.org/10.1023/B:TRIL.0000044495.26882.b5.

[53] C. Grossiord, K. Varlot, J.-M. Martin, T. L. Mogne, C. Esnouf, and K. Inoue, Tribology International **31**, 737 (1998), ISSN 0301-679X, URL http://www.sciencedirect.com/science/article/pii/S0301679X98000942.

[54] H. Spedding and R. Watkins, Tribology International **15**, 9 (1982), ISSN 0301-679X, URL http://www.sciencedirect.com/science/article/pii/0301679X82901013.

[55] R. Watkins, Tribology International **15**, 13 (1982), ISSN 0301-679X, URL http://www.sciencedirect.com/science/article/pii/0301679X82901025.

[56] M. Kawamura, Wear **77**, 287 (1982), ISSN 0043-1648, URL http://www.sciencedirect.com/science/article/pii/0043164882900540.

[57] Z. Yin, M. Kasrai, M. Fuller, G. Bancroft, K. Fyfe, and K. H. Tan, Wear **202**, 172 (1997), ISSN 0043-1648, URL http://www.sciencedirect.com/science/article/pii/S0043164896072729.

[58] J. M. Martin, C. Grossiord, T. L. Mogne, S. Bec, and A. Tonck, Tribology International **34**, 523 (2001), ISSN 0301-679X, URL http://www.sciencedirect.com/science/article/pii/S0301679X01000299.

[59] M. D. Barros, J. Bouchet, I. Raoult, T. L. Mogne, J. Martin, M. Kasrai, and Y. Yamada, Wear **254**, 863 (2003), ISSN 0043-1648, papers presented at the 280th We-Hereaus Seminar Integrating Friction and Wear Research, URL http://www.sciencedirect.com/science/article/pii/S0043164803002370.

[60] L. Taylor, A. Dratva, and H. A. Spikes, Tribology Transactions **43**, 469 (2000), https://doi.org/10.1080/10402000008982366, URL https://doi.org/10.1080/10402000008982366.

[61] J. M. Martin, Tribology Letters **6**, 1 (1999), ISSN 1573-2711, URL https://doi.org/10.1023/A:1019191019134.

[62] S. Bec, A. Tonck, J. M. Georges, and G. W. Roper, Tribology Letters **17**, 797 (2004), ISSN 1573-2711, URL https://doi.org/10.1007/s11249-004-8088-7.

[63] M. De Feo, C. Minfray, M. I. De Barros Bouchet, B. Thiebaut, and J. M. Martin, RSC Adv. **5**, 93786 (2015), URL http://dx.doi.org/10.1039/C5RA15250J.

[64] F. Barcroft, Wear **3**, 440 (1960), ISSN 0043-1648, URL http://www.sciencedirect.com/science/article/pii/0043164860902283.

[65] W. Liu and Q. Xue, Thin Solid Films **295**, 19 (1997), ISSN 0040-6090, URL http://www.sciencedirect.com/science/article/pii/S0040609096089778.

[66] H. Spikes, Lubrication Science **20**, 103 (2008), https://onlinelibrary.wiley.com/doi/pdf/10.1002/ls.57, URL https://onlinelibrary.wiley.com/doi/abs/10.1002/ls.57.

[67] B. K. Sharma, A. Adhvaryu, and S. Z. Erhan, Tribology International **42**, 353 (2009), ISSN 0301-679X, URL http://www.sciencedirect.com/science/article/pii/S0301679X08001606.

[68] D. Philippon, M.-I. de Barros-Bouchet, T. L. Mogne, E. Gresser, and J.-M. Martin, Tribology - Materials, Surfaces & Interfaces **1**, 113 (2007), https://doi.org/10.1179/175158408X273586, URL https://doi.org/10.1179/175158408X273586.

[69] J. Tannous, B. M. I. de Bouchet, T. Le-Mogne, P. Charles, and J. M. Martin, Tribology - Materials, Surfaces & Interfaces **1**, 98 (2007), https://doi.org/10.1179/175158407X231321, URL https://doi.org/10.1179/175158407X231321.

[70] A. Murase and T. Ohmori, Surface and Interface Analysis **31**, 93 (2001), https://onlinelibrary.wiley.com/doi/pdf/10.1002/sia.961, URL https://onlinelibrary.wiley.com/doi/abs/10.1002/sia.961.

[71] M.-I. De Barros Bouchet and J.-M. Martin, *Tribochemistry of n-Alkane Thiols Examined by Gas-Phase Lubrication (GPL)* (Springer International Publishing, Cham, 2018), pp. 107–128, ISBN 978-3-319-99897-8, URL https://doi.org/10.1007/978-3-319-99897-8_4.

[72] J. Hu, X. d. Xiao, D. Ogletree, and M. Salmeron, Surface Science **327**, 358 (1995), ISSN 0039-6028, URL http://www.sciencedirect.com/science/article/pii/0039602894008469.

[73] Q. Li, Y. Dong, D. Perez, A. Martini, and R. W. Carpick, Phys. Rev. Lett. **106**, 126101 (2011), URL https://link.aps.org/doi/10.1103/PhysRevLett.106.126101.

[74] E. Riedo, E. Gnecco, R. Bennewitz, E. Meyer, and H. Brune, Phys. Rev. Lett. **91**, 084502 (2003), URL https://link.aps.org/doi/10.1103/PhysRevLett.91.084502.

[75] A. Schirmeisen, L. Jansen, H. Holscher, and H. Fuchs, Applied Physics Letters **88**, 123108 (2006), https://doi.org/10.1063/1.2187575, URL https://doi.org/10.1063/1.2187575.

[76] N. N. Gosvami, J. A. Bares, F. Mangolini, A. R. Konicek, D. G. Yablon, and R. W. Carpick, Science **348**, 102 (2015), ISSN 0036-8075, https://science.sciencemag.org/content/348/6230/102.full.pdf, URL https://science.sciencemag.org/content/348/6230/102.

[77] N. N. Gosvami, J. Ma, and R. W. Carpick, Tribology Letters **66**, 154 (2018), ISSN 1573-2711, URL https://doi.org/10.1007/s11249-018-1112-0.

[78] T. Friščić, I. Halasz, P. J. Beldon, A. M. Belenguer, F. Adams, S. A. Kimber, V. Honkimäki, and R. E. Dinnebier, Nature chemistry **5**, 66 (2013), URL https://www.nature.com/articles/nchem.1505.

[79] W. G. Sawyer and K. J. Wahl, MRS Bulletin **33**, 1145 (2008).

[80] O. L. Warren, Z. Shan, S. S. Asif, E. A. Stach, J. Morris Jr, and A. M. Minor, Materials Today **10**, 59 (2007), URL https://www.materialstoday.com/characterization/articles/s1369702107700512/.

[81] Z. B. Milne, R. A. Bernal, and R. W. Carpick, Langmuir **0**, null (2019), pMID: 31397572, https://doi.org/10.1021/acs.langmuir.9b02029, URL https://doi.org/10.1021/acs.langmuir.9b02029.

[82] T. D. B. Jacobs, C. Greiner, K. J. Wahl, and R. W. Carpick, MRS Bulletin **44**, 478 (2019).

[83] R. A. Bernal and R. W. Carpick, Carbon **154**, 132 (2019), ISSN 0008-6223, URL http://www.sciencedirect.com/science/article/pii/S0008622319307754.

[84] M. Reguzzoni, M. Ferrario, S. Zapperi, and M. C. Righi, Proceedings of the National Academy of Sciences **107**, 1311 (2010), ISSN 0027-8424, https://www.pnas.org/content/107/4/1311.full.pdf, URL https://www.pnas.org/content/107/4/1311.

[85] M. Hirano and K. Shinjo, Phys. Rev. B **41**, 11837 (1990), URL https://link.aps.org/doi/10.1103/PhysRevB.41.11837.

[86] O. Hod, Phys. Rev. B **86**, 075444 (2012), URL https://link.aps.org/doi/10.1103/PhysRevB.86.075444.

[87] B. Luan and M. O. Robbins, Nature **435**, 929 (2005), URL https://www.nature.com/articles/nature03700.

[88] B. Luan and M. O. Robbins, Phys. Rev. E **74**, 026111 (2006), URL https://link.aps.org/doi/10.1103/PhysRevE.74.026111.

[89] P. A. Thompson, G. S. Grest, and M. O. Robbins, Phys. Rev. Lett. **68**, 3448 (1992), URL https://link.aps.org/doi/10.1103/PhysRevLett.68.3448.

[90] J. P. Ewen, C. Gattinoni, N. Morgan, H. A. Spikes, and D. Dini, Langmuir **32**, 4450 (2016), pMID: 27064962, https://doi.org/10.1021/acs.langmuir.6b00586, URL https://doi.org/10.1021/acs.langmuir.6b00586.

[91] W. Yan and K. Komvopoulos, Journal of Tribology **120**, 385 (1998), ISSN 0742-4787, https://asmedigitalcollection.asme.org/tribology/article-pdf/120/2/385/5642144/385_1.pdf, URL https://doi.org/10.1115/1.2834438.

[92] R. Aghababaei, D. H. Warner, and J.-F. Molinari, Proceedings of the National Academy of Sciences **114**, 7935 (2017), ISSN 0027-8424, https://www.pnas.org/content/114/30/7935.full.pdf, URL https://www.pnas.org/content/114/30/7935.

[93] A. C. T. van Duin, S. Dasgupta, F. Lorant, and W. A. Goddard, The Journal of Physical Chemistry A **105**, 9396 (2001), https://doi.org/10.1021/jp004368u, URL https://doi.org/10.1021/jp004368u.

[94] J. Yeon, H. L. Adams, C. E. Junkermeier, A. C. T. van Duin, W. T. Tysoe, and A. Martini, The Journal of Physical Chemistry B **122**, 888 (2018), pMID: 28981284, https://doi.org/10.1021/acs.jpcb.7b06976, URL https://doi.org/10.1021/acs.jpcb.7b06976.

[95] K. Mohammadtabar, S. J. Eder, P. O. Bedolla, N. Drr, and A. Martini, Langmuir **34**, 15681 (2018), https://doi.org/10.1021/acs.langmuir.8b03170, URL https://doi.org/10.1021/acs.langmuir.8b03170.

[96] S. Dag and S. Ciraci, Phys. Rev. B **70**, 241401 (2004), URL https://link.aps.org/doi/10.1103/PhysRevB.70.241401.

[97] S. Kajita and M. Righi, Carbon **103**, 193 (2016), ISSN 0008-6223, URL http://www.sciencedirect.com/science/article/pii/S0008622316301713.

[98] T. Kuwahara, G. Moras, and M. Moseler, Phys. Rev. Lett. **119**, 096101 (2017), URL https://link.aps.org/doi/10.1103/PhysRevLett.119.096101.

[99] L.-F. Wang, T.-B. Ma, Y.-Z. Hu, H. Wang, and T.-M. Shao, The Journal of Physical Chemistry C **117**, 12520 (2013), https://doi.org/10.1021/jp401097a, URL https://doi.org/10.1021/jp401097a.

[100] A. Ambrosetti, F. Ancilotto, and P. L. Silvestrelli, The Journal of Physical Chemistry C **117**, 321 (2013), https://doi.org/10.1021/jp309617f, URL https://doi.org/10.1021/jp309617f.

[101] T. Onodera, Y. Morita, A. Suzuki, M. Koyama, H. Tsuboi, N. Hatakeyama, A. Endou, H. Takaba, M. Kubo, F. Dassenoy, et al., The Journal of Physical Chemistry B **113**, 16526 (2009), pMID: 19968319, https://doi.org/10.1021/jp9069866, URL https://doi.org/10.1021/jp9069866.

[102] G. Tocci, L. Joly, and A. Michaelides, Nano Letters **14**, 6872 (2014), pMID: 25394228, https://doi.org/10.1021/nl502837d, URL https://doi.org/10.1021/nl502837d.

[103] P. Restuccia and M. C. Righi, Carbon **106**, 118 (2016), URL http://www.sciencedirect.com/science/article/pii/S0008622316303797.

[104] G. Levita and M. C. Righi, ChemPhysChem **18**, 1475 (2017), https://onlinelibrary.wiley.com/doi/pdf/10.1002/cphc.201601143, URL https://onlinelibrary.wiley.com/doi/abs/10.1002/cphc.201601143.

[105] V. Jaiswal, R. B. Rastogi, J. L. Maurya, P. Singh, and A. K. Tewari, RSC Adv. **4**, 13438 (2014), URL http://dx.doi.org/10.1039/C3RA45806G.

[106] D. E. Jiang and E. A. Carter, Phys. Rev. B **71**, 045402 (2005), URL https://link.aps.org/doi/10.1103/PhysRevB.71.045402.

[107] J. M. H. Lo and T. Ziegler, The Journal of Physical Chemistry C **111**, 11012 (2007), https://doi.org/10.1021/jp0722206, URL https://doi.org/10.1021/jp0722206.

[108] D. C. Sorescu, Phys. Rev. B **73**, 155420 (2006), URL https://link.aps.org/doi/10.1103/PhysRevB.73.155420.

[109] P. Błoński, A. Kiejna, and J. Hafner, Surface Science **590**, 88 (2005), ISSN 0039-6028, URL http://www.sciencedirect.com/science/article/pii/S0039602805006539.

[110] M. C. Righi, S. Loehl, M. I. de Barros Bouchet, D. Philippon, and J. M. Martin, RSC Adv. **5**, 101162 (2015), URL http://dx.doi.org/10.1039/C5RA14446A.

[111] M. C. Righi, S. Loehlé, M. I. De Barros Bouchet, S. Mambingo-Doumbe, and J. M. Martin, RSC Adv. **6**, 47753 (2016), URL http://dx.doi.org/10.1039/C6RA07545B.

[112] M. Reguzzoni, A. Fasolino, E. Molinari, and M. C. Righi, Phys. Rev. B **86**, 245434 (2012), URL https://link.aps.org/doi/10.1103/PhysRevB.86.245434.

[113] G. Levita, A. Cavaleiro, E. Molinari, T. Polcar, and M. C. Righi, The Journal of Physical Chemistry C **118**, 13809 (2014), https://doi.org/10.1021/jp4098099, URL https://doi.org/10.1021/jp4098099.

[114] G. Levita, P. Restuccia, and M. Righi, Carbon **107**, 878 (2016), URL https://doi.org/10.1016/j.carbon.2016.06.072.

[115] C. Lee, Q. Li, W. Kalb, X.-Z. Liu, H. Berger, R. W. Carpick, and J. Hone, Science **328**, 76 (2010), ISSN 0036-8075, https://science.sciencemag.org/content/328/5974/76.full.pdf, URL https://science.sciencemag.org/content/328/5974/76.

[116] D. Marchetto, P. Restuccia, A. Ballestrazzi, M. C. Righi, A. Rota, and S. Valeri, Carbon **116**, 375 (2017), ISSN 0008-6223, URL http://www.sciencedirect.com/science/article/pii/S000862231730129X.

[117] M. Pierno, L. Bignardi, M. C. Righi, L. Bruschi, S. Gottardi, M. Sthr, O. Ivashenko, P. L. Silvestrelli, P. Rudolf, and G. Mistura, Nanoscale **6**, 8062 (2014), URL http://dx.doi.org/10.1039/C4NR01079E.

[118] P. Restuccia, M. Ferrario, P. L. Sivestrelli, G. Mistura, and M. C. Righi, Phys. Chem. Chem. Phys. **18**, 28997 (2016), URL http://dx.doi.org/10.1039/C6CP05386F.

[119] M. I. De Barros-Bouchet, M. C. Righi, D. Philippon, S. Mambingo-Doumbe, T. Le-Mogne, J. M. Martin, and A. Bouffet, RSC Adv. **5**, 49270 (2015), URL http://dx.doi.org/10.1039/C5RA00721F.

[120] G. Zilibotti and M. C. Righi, Langmuir **27**, 6862 (2011), pMID: 21545120, https://doi.org/10.1021/la200783a, URL https://doi.org/10.1021/la200783a.

[121] S. Cahangirov, C. Ataca, M. Topsakal, H. Sahin, and S. Ciraci, Phys. Rev. Lett. **108**, 126103 (2012), URL https://link.aps.org/doi/10.1103/PhysRevLett.108.126103.

[122] S. Loehl and M. Righi, Lubricants **6**, 31 (2018), ISSN 2075-4442, URL http://dx.doi.org/10.3390/lubricants6020031.

[123] A. R. Konicek, D. S. Grierson, P. U. P. A. Gilbert, W. G. Sawyer, A. V. Sumant, and R. W. Carpick, Phys. Rev. Lett. **100**, 235502 (2008), URL https://link.aps.org/doi/10.1103/PhysRevLett.100.235502.

[124] J. D. Schall, G. Gao, and J. A. Harrison, The Journal of Physical Chemistry C **114**, 5321 (2010), https://doi.org/10.1021/jp904871t, URL https://doi.org/10.1021/jp904871t.

[125] M.-I. De Barros Bouchet, G. Zilibotti, C. Matta, M. Righi, L. Vandenbulcke, B. Vacher, and J.-M. M., The Journal of Physical Chemistry C **116**, 6966 (2012), https://doi.org/10.1021/jp211322s, URL https://doi.org/10.1021/jp211322s.

[126] N. Kato, H. Mori, and N. Takahashi, physica status solidi c **5**, 1117 (2008), https://onlinelibrary.wiley.com/doi/pdf/10.1002/pssc.200777751, URL https://onlinelibrary.wiley.com/doi/abs/10.1002/pssc.200777751.

[127] H. Mori, N. Takahashi, N. Kazuyuki, H. Tachikawa, and T. Ohmori, Tech. Rep., SAE Technical Paper (2007), URL https://www.sae.org/publications/technical-papers/content/2007-01-1015.

[128] X. Wu, T. Ohana, A. Tanaka, T. Kubo, H. Nanao, I. Minami, and S. Mori, Diamond and Related Materials **17**, 147 (2008), ISSN 0925-9635, URL http://www.sciencedirect.com/science/article/pii/S0925963507004888.

[129] T. A. Burgo, C. A. Silva, L. B. Balestrin, and F. Galembeck, Scientific reports **3**, 2384 (2013), URL https://www.nature.com/articles/srep02384.

[130] J. Lowell and A. Rose-Innes, Advances in Physics **29**, 947 (1980), https://doi.org/10.1080/00018738000101466, URL https://doi.org/10.1080/00018738000101466.

[131] T. Shinbrot, B. Ferdowsi, S. Sundaresan, and N. A. M. Araujo, Phys. Rev. Materials **2**, 125003 (2018), URL https://link.aps.org/doi/10.1103/PhysRevMaterials.2.125003.

[132] F. Bacon, *Novum organum (1620)* (1902).

[133] E. N. Harvey, Science **89**, 460 (1939), ISSN 0036-8075, https://science.sciencemag.org/content/89/2316/460.full.pdf, URL https://science.sciencemag.org/content/89/2316/460.

[134] K.-E. Byun, Y. Cho, M. Seol, S. Kim, S.-W. Kim, H.-J. Shin, S. Park, and S. Hwang, ACS Applied Materials & Interfaces **8**, 18519 (2016), pMID: 27337938, https://doi.org/10.1021/acsami.6b02802, URL https://doi.org/10.1021/acsami.6b02802.

[135] K. W. Biegaj, M. G. Rowland, T. M. Lukas, and J. Y. Y. Heng, ACS Omega **2**, 1576 (2017), https://doi.org/10.1021/acsomega.7b00125, URL https://doi.org/10.1021/acsomega.7b00125.

[136] S.-H. Shin, Y. E. Bae, H. K. Moon, J. Kim, S.-H. Choi, Y. Kim, H. J. Yoon, M. H. Lee, and J. Nah, ACS Nano **11**, 6131 (2017), pMID: 28558185, https://doi.org/10.1021/acsnano.7b02156, URL https://doi.org/10.1021/acsnano.7b02156.

[137] M. Seol, S. Kim, Y. Cho, K.-E. Byun, H. Kim, J. Kim, S. K. Kim, S.-W. Kim, H.-J. Shin, and S. Park, Advanced Materials **30**, 1801210 (2018), https://onlinelibrary.wiley.com/doi/pdf/10.1002/adma.201801210, URL https://onlinelibrary.wiley.com/doi/abs/10.1002/adma.201801210.

[138] X. Shen, A. E. Wang, R. M. Sankaran, and D. J. Lacks, Journal of Electrostatics **82**, 11 (2016), ISSN 0304-3886, URL http://www.sciencedirect.com/science/article/pii/S0304388616300353.

[139] S.-q. Lin and T.-m. Shao, Phys. Chem. Chem. Phys. **19**, 29418 (2017), URL http://dx.doi.org/10.1039/C7CP05609E.

[140] C. Xu, Y. Zi, A. C. Wang, H. Zou, Y. Dai, X. He, P. Wang, Y.-C. Wang, P. Feng, D. Li, et al., Advanced Materials **30**, 1706790 (2018), https://onlinelibrary.wiley.com/doi/pdf/10.1002/adma.201706790, URL https://onlinelibrary.wiley.com/doi/abs/10.1002/adma.201706790.

[141] A. Ciniero (2017), URL http://hdl.handle.net/10044/1/62826.

[142] A. Ciniero, D. Dini, and T. Reddyhoff, in *APS Meeting Abstracts* (2018), p. P38.011.

[143] L. S. McCarty and G. M. Whitesides, Angewandte Chemie International Edition **47**, 2188 (2008), https://onlinelibrary.wiley.com/doi/pdf/10.1002/anie.200701812, URL https://onlinelibrary.wiley.com/doi/abs/10.1002/anie.200701812.

[144] L. S. McCarty, A. Winkleman, and G. M. Whitesides, Journal of the American Chemical Society **129**, 4075 (2007), pMID: 17311380, https://doi.org/10.1021/ja067301e, URL https://doi.org/10.1021/ja067301e.

[145] M. Hogue, E. Mucciolo, C. Calle, and C. Buhler, Journal of Electrostatics **63**, 179 (2005), ISSN 0304-3886, selected Papers from the ESA 2004 Annual Conference, URL http://www.sciencedirect.com/science/article/pii/S0304388604001767.

[146] T. R. D. Ducati, L. H. Simes, and F. Galembeck, Langmuir **26**, 13763 (2010), pMID: 20704354, https://doi.org/10.1021/la102494k, URL https://doi.org/10.1021/la102494k.

[147] R. K. Pandey, Y. Sun, H. Nakanishi, and S. Soh, The Journal of Physical Chemistry Letters **8**, 6142 (2017), pMID: 29206045, https://doi.org/10.1021/acs.jpclett.7b02763, URL https://doi.org/10.1021/acs.jpclett.7b02763.

[148] K. Homewood, Journal of Electrostatics **10**, 299 (1981), ISSN 0304-3886, URL http://www.sciencedirect.com/science/article/pii/0304388681900590.

[149] J. Henniker, Nature **196**, 474 (1962), URL https://doi.org/10.1038/196474a0.

[150] B. Baytekin, H. T. Baytekin, and B. A. Grzybowski, Journal of the American Chemical Society **134**, 7223 (2012), pMID: 22494318, https://doi.org/10.1021/ja300925h, URL https://doi.org/10.1021/ja300925h.

[151] A. Barnes and A. Dinsmore, Journal of Electrostatics **81**, 76 (2016), ISSN 0304-3886, URL http://www.sciencedirect.com/science/article/pii/S0304388616300250.

[152] M. Neagoe, Y. Prawatya, T. Zeghloul, and L. Dascalescu, Journal of Electrostatics **90**, 123 (2017), ISSN 0304-3886, URL http://www.sciencedirect.com/science/article/pii/S0304388617302358.

[153] L. Beraldo da Silveira Balestrin, D. Del Duque, D. Soares da Silva, and F. Galembeck, Faraday Discuss. **170**, 369 (2014), URL http://dx.doi.org/10.1039/C3FD00118K.

[154] M. Sow, D. Lacks, and R. Mohan Sankaran, Journal of Applied Physics **112**, 084909 (2012), https://doi.org/10.1063/1.4761967, URL https://doi.org/10.1063/1.4761967.

[155] A. E. Wang, P. S. Gil, M. Holonga, Z. Yavuz, H. T. Baytekin, R. M. Sankaran, and D. J. Lacks, Phys. Rev. Materials **1**, 035605 (2017), URL https://link.aps.org/doi/10.1103/PhysRevMaterials.1.035605.

[156] J. C. Angus and I. Greber, Journal of Applied Physics **123**, 174102 (2018), https://doi.org/10.1063/1.5024742, URL https://doi.org/10.1063/1.5024742.

[157] G. Fatti, P. Restuccia, C. Calandra, and M. C. Righi, The Journal of Physical Chemistry C **122**, 28105 (2018), https://doi.org/10.1021/acs.jpcc.8b08831, URL https://doi.org/10.1021/acs.jpcc.8b08831.

[158] A. T. Kelly, I. Rusakova, T. Ould-Ely, C. Hofmann, A. Lüttge, and K. H. Whitmire, Nano Letters **7**, 2920 (2007), pMID: 17683155, https://doi.org/10.1021/nl0713225, URL https://doi.org/10.1021/nl0713225.

[159] S. Carenco, D. Portehault, C. Boissière, N. Mézailles, and C. Sanchez, Chemical Reviews **113**, 7981 (2013), pMID: 23767879, https://doi.org/10.1021/cr400020d, URL https://doi.org/10.1021/cr400020d.

[160] J. Demaree, G. Was, and N. Sorensen, Surface and Coatings Technology **51**, 6 (1992), ISSN 0257-8972, URL http://www.sciencedirect.com/science/article/pii/025789729290206P.

[161] A. Holbert, J. Batteas, A. Wong-Foy, T. Rufael, and C. Friend, Surface Science **401**, L437 (1998), ISSN 0039-6028, URL http://www.sciencedirect.com/science/article/pii/S0039602898000764.

[162] M. Seah, Acta Metallurgica **28**, 955 (1980), ISSN 0001-6160, URL http://www.sciencedirect.com/science/article/pii/0001616080901121.

[163] V. Rangarajan, R. Toncheff, and L. L. Franks, Metallurgical and Materials Transactions A **29**, 2707 (1998), ISSN 1543-1940, URL https://doi.org/10.1007/s11661-998-0311-y.

[164] A. W. James and C. M. Shepherd, Materials Science and Technology **5**, 333 (1989), https://doi.org/10.1179/mst.1989.5.4.333, URL https://doi.org/10.1179/mst.1989.5.4.333.

[165] W. Arabczyk, H.-J. Mssig, and F. Storbeck, Surface Science **251-252**, 804 (1991), ISSN 0039-6028, URL http://www.sciencedirect.com/science/article/pii/0039602891911024.

[166] C. Shell and J. Rivière, Surface Science **40**, 149 (1973), ISSN 0039-6028, URL http://www.sciencedirect.com/science/article/pii/0039602873900587.

[167] H. J. Grabke, Kovine zlitine tehnologije **27**, 9 (1993), URL https://www.dlib.si/stream/URN:NBN:SI:DOC-6LK5NE66/841d6a71-1a76-4763-a56a-36652193a3ff/PDF.

[168] E. Wachowicz and A. Kiejna, Modelling and Simulation in Materials Science and Engineering **19**, 025001 (2011), URL http://stacks.iop.org/0965-0393/19/i=2/a=025001.

[169] H. D. Shih, F. Jona, D. W. Jepsen, and P. M. Marcus, Phys. Rev. Lett. **46**, 731 (1981), URL https://link.aps.org/doi/10.1103/PhysRevLett.46.731.

[170] G. W. Fernando and J. W. Wilkins, Phys. Rev. B **33**, 3709 (1986), URL https://link.aps.org/doi/10.1103/PhysRevB.33.3709.

[171] S. R. Chubb and W. E. Pickett, Phys. Rev. B **38**, 10227 (1988), URL https://link.aps.org/doi/10.1103/PhysRevB.38.10227.

[172] M. J. Spencer, A. Hung, I. K. Snook, and I. Yarovsky, Surface Science **540**, 420 (2003), ISSN 0039-6028, URL http://www.sciencedirect.com/science/article/pii/S0039602803008835.

[173] M. J. S. Spencer, I. K. Snook, and I. Yarovsky, The Journal of Physical Chemistry B **109**, 9604 (2005), pMID: 16852156, https://doi.org/10.1021/jp044378l, URL https://doi.org/10.1021/jp044378l.

[174] M. J. S. Spencer, I. K. Snook, and I. Yarovsky, The Journal of Physical Chemistry B **108**, 10965 (2004), https://doi.org/10.1021/jp049506k, URL https://doi.org/10.1021/jp049506k.

[175] J. Mortensen, M. Ganduglia-Pirovano, L. Hansen, B. Hammer, P. Stoltze, and J. Nrskov, Surface Science **422**, 8 (1999), ISSN 0039-6028, URL http://www.sciencedirect.com/science/article/pii/S0039602898008024.

[176] D. K. Escott, S. J. Pratt, and D. A. King, Surface Science **562**, 226 (2004), ISSN 0039-6028, URL http://www.sciencedirect.com/science/article/pii/S0039602804007101.

[177] R. Imbihl, R. Behm, G. Ertl, and W. Moritz, Surface Science **123**, 129 (1982), ISSN 0039-6028, URL http://www.sciencedirect.com/science/article/pii/0039602882901352.

[178] i. c. v. c. v. Pick, P. Légaré, and C. Demangeat, Phys. Rev. B **75**, 195446 (2007), URL https://link.aps.org/doi/10.1103/PhysRevB.75.195446.

[179] C. Leygraf and S. Ekelund, Surface Science **40**, 609 (1973), ISSN 0039-6028, URL http://www.sciencedirect.com/science/article/pii/0039602873901489.

[180] F. J. Himpsel and J. E. Ortega, Surface science **268**, L279 (1992), URL https://www.sciencedirect.com/science/article/pii/003960289290935Y.

[181] J. Weissenrieder, M. Göthelid, M. Månsson, H. von Schenck, O. Tjernberg, and U. O. Karlsson, Surface Science **527**, 163 (2003), ISSN 0039-6028, URL http://www.sciencedirect.com/science/article/pii/S0039602803000189.

[182] O. T and A. Kiejna, Surface Science **637-638**, 35 (2015), ISSN 0039-6028, URL http://www.sciencedirect.com/science/article/pii/S0039602815000618.

[183] H. W. Hugosson, W. Cao, S. Seetharaman, and A. Delin, The Journal of Physical Chemistry C **117**, 6161 (2013), https://doi.org/10.1021/jp3102496, URL https://doi.org/10.1021/jp3102496.

[184] U. K. Chohan, S. P. Koehler, and E. Jimenez-Melero, Computational Materials Science **134**, 109 (2017), ISSN 0927-0256, URL http://www.sciencedirect.com/science/article/pii/S0927025617301544.

[185] L. Xu, D. Kirvassilis, Y. Bai, and M. Mavrikakis, Surface Science **667**, 54 (2018), ISSN 0039-6028, URL http://www.sciencedirect.com/science/article/pii/S0039602817305988.

[186] P. Giannozzi, S. Baroni, N. Bonini, M. Calandra, R. Car, C. Cavazzoni, D. Ceresoli, G. L. Chiarotti, M. Cococcioni, I. Dabo, et al., Journal of Physics: Condensed Matter **21**, 395502 (2009), URL http://stacks.iop.org/0953-8984/21/i=39/a=395502.

[187] J. P. Perdew, K. Burke, and M. Ernzerhof, Phys. Rev. Lett. **77**, 3865 (1996), URL https://link.aps.org/doi/10.1103/PhysRevLett.77.3865.

[188] WebElements Periodic Table: www.webelements.com (—), URL www.webelements.com.

[189] H. J. Monkhorst and J. D. Pack, Phys. Rev. B **13**, 5188 (1976), URL https://link.aps.org/doi/10.1103/PhysRevB.13.5188.

[190] M. Otani and O. Sugino, Phys. Rev. B **73**, 115407 (2006), URL https://link.aps.org/doi/10.1103/PhysRevB.73.115407.

[191] W. .Tang, E. Sanville, and G. Henkelman, Journal of Physics: Condensed Matter **21**, 084204 (2009), URL http://stacks.iop.org/0953-8984/21/i=8/a=084204.

[192] E. Sanville, S. D. Kenny, R. Smith, and G. Henkelman, Journal of Computational Chemistry **28**, 899 (2007), https://onlinelibrary.wiley.com/doi/pdf/10.1002/jcc.20575, URL https://onlinelibrary.wiley.com/doi/abs/10.1002/jcc.20575.

[193] G. Henkelman, A. Arnaldsson, and H. Jónsson, Computational Materials Science **36**, 354 (2006), ISSN 0927-0256, URL http://www.sciencedirect.com/science/article/pii/S0927025605001849.

[194] M. Yu and D. R. Trinkle, The Journal of Chemical Physics **134**, 064111 (2011), https://doi.org/10.1063/1.3553716, URL https://doi.org/10.1063/1.3553716.

[195] H. D. Shih, F. Jona, U. Bardi, and P. M. Marcus, Journal of Physics C: Solid State Physics **13**, 3801 (1980), URL http://stacks.iop.org/0022-3719/13/i=19/a=021.

[196] C. Xu and D. O'Connor, Nuclear Instruments and Methods in Physics Research Section B: Beam Interactions with Materials and Atoms **53**, 315 (1991).

[197] J. Nørskov, S. Holloway, and N. Lang, Surface Science **137**, 65 (1984), ISSN 0039-6028, URL http://www.sciencedirect.com/science/article/pii/0039602884906769.

[198] N. Lang, S. Holloway, and J. Nørskov, Surface Science **150**, 24 (1985), ISSN 0039-6028, URL http://www.sciencedirect.com/science/article/pii/0039602885902080.

[199] N. Lang, Surface Science Letters **127**, L118 (1983), ISSN 0167-2584, URL http://www.sciencedirect.com/science/article/pii/0167258483904425.

[200] J. Kołaczkiewicz and E. Bauer, Surface Science **450**, 106 (2000), ISSN 0039-6028, URL http://www.sciencedirect.com/science/article/pii/S003960280000056X.

[201] P. Błoński and A. Kiejna, Vacuum **74**, 179 (2004), ISSN 0042-207X, proceedings of the International Workshop on Surface Physics: Metals on Solid Surfaces, URL http://www.sciencedirect.com/science/article/pii/S0042207X04000132.

[202] P. Błoński and A. Kiejna, Surface Science **601**, 123 (2007), ISSN 0039-6028, URL http://www.sciencedirect.com/science/article/pii/S0039602806009563.

[203] X. Tan, J. Zhou, and Y. Peng, Applied Surface Science **258**, 8484 (2012), ISSN 0169-4332, URL http://www.sciencedirect.com/science/article/pii/S0169433212008288.

[204] I. Langmuir, Phys. Rev. **21**, 419 (1923), URL https://link.aps.org/doi/10.1103/PhysRev.21.419.

[205] H. Bonzel, Surface Science Reports **8**, 43 (1988), ISSN 0167-5729, URL http://www.sciencedirect.com/science/article/pii/0167572988900076.

[206] P. S. Bagus, D. Käfer, G. Witte, and C. Wöll, Phys. Rev. Lett. **100**, 126101 (2008), URL https://link.aps.org/doi/10.1103/PhysRevLett.100.126101.

[207] A. Migani, C. Sousa, and F. Illas, Surface Science **574**, 297 (2005), ISSN 0039-6028, URL http://www.sciencedirect.com/science/article/pii/S0039602804014086.

[208] A. Michaelides, P. Hu, M.-H. Lee, A. Alavi, and D. A. King, Phys. Rev. Lett. **90**, 246103 (2003), URL https://link.aps.org/doi/10.1103/PhysRevLett.90.246103.

[209] T. C. Leung, C. L. Kao, W. S. Su, Y. J. Feng, and C. T. Chan, Phys. Rev. B **68**, 195408 (2003), URL https://link.aps.org/doi/10.1103/PhysRevB.68.195408.

[210] D. M. Newns, Phys. Rev. **178**, 1123 (1969), URL https://link.aps.org/doi/10.1103/PhysRev.178.1123.

[211] J. K. Norskov, Reports on Progress in Physics **53**, 1253 (1990), URL http://stacks.iop.org/0034-4885/53/i=10/a=001.

[212] G. Fatti and M. Righi, Tribology Letters **67**, 125 (2019), URL https://link.springer.com/article/10.1007/s11249-019-1235-y.

[213] D. Sarid and V. Elings, Journal of Vacuum Science & Technology B: Microelectronics and Nanometer Structures Processing, Measurement, and Phenomena **9**, 431 (1991), https://avs.scitation.org/doi/pdf/10.1116/1.585585, URL https://avs.scitation.org/doi/abs/10.1116/1.585585.

[214] J. A. Dagata, Scanning **14**, 118 (1992), https://onlinelibrary.wiley.com/doi/pdf/10.1002/sca.4950140211, URL https://onlinelibrary.wiley.com/doi/abs/10.1002/sca.4950140211.

[215] M. Reguzzoni, A. Fasolino, E. Molinari, and M. C. Righi, Phys. Rev. B **86**, 245434 (2012), URL https://link.aps.org/doi/10.1103/PhysRevB.86.245434.

[216] G. Zilibotti, M. C. Righi, and M. Ferrario, Phys. Rev. B **79**, 075420 (2009), URL https://link.aps.org/doi/10.1103/PhysRevB.79.075420.

[217] P. Restuccia, G. Levita, M. Wolloch, G. Losi, G. Fatti, M. Ferrario, and M. Righi, Computational Materials Science **154**, 517 (2018), URL https://www.sciencedirect.com/science/article/pii/S092702561830510X.

[218] C. Pichard, M. Guttmann, J. Rieu, and C. Goux, Le Journal de Physique Colloques **36**, C4 151 (1975), URL https://doi.org/10.1051/jphyscol:1975416.

[219] C. McMahon Jr and L. Marchut, Journal of Vacuum Science and Technology **15**, 450 (1978), URL https://doi.org/10.1116/1.569592.

[220] E. D. Hondros and M. P. Seah, Metallurgical Transactions A **8**, 1363 (1977), ISSN 1543-1940, URL https://doi.org/10.1007/BF02642850.

[221] E. González, P. Jasen, M. Sandoval, P. Bechthold, A. Juan, B. S. Batic, and M. Jenko, Applied Surface Science **257**, 6878 (2011), URL https://doi.org/10.1016/j.apsusc.2011.03.022.

[222] W. E, W. Ren, and E. Vanden-Eijnden, Phys. Rev. B **66**, 052301 (2002), URL https://link.aps.org/doi/10.1103/PhysRevB.66.052301.

[223] W. E, W. Ren, and E. Vanden-Eijnden, The Journal of Chemical Physics **126**, 164103 (2007), https://doi.org/10.1063/1.2720838, URL https://doi.org/10.1063/1.2720838.

[224] D. Berman, S. A. Deshmukh, S. K. R. S. Sankaranarayanan, A. Erdemir, and A. V. Sumant, Science **348**, 1118 (2015), ISSN 0036-8075, http://science.sciencemag.org/content/348/6239/1118.full.pdf, URL http://science.sciencemag.org/content/348/6239/1118.

[225] S. Cahangirov, S. Ciraci, and V. O. Özçelik, Phys. Rev. B **87**, 205428 (2013), URL https://link.aps.org/doi/10.1103/PhysRevB.87.205428.

[226] S. M. Hsu, J. Zhang, and Z. Yin, Tribology Letters **13**, 131 (2002), ISSN 1573-2711, URL https://doi.org/10.1023/A:1020112901674.

[227] C. Donnet and A. Erdemir, Surface and Coatings Technology **180-181**, 76 (2004), ISSN 0257-8972, proceedings of Symposium G on Protective Coatings and Thin Films-03, of the E-MRS 2003 Spring Conference, URL http://www.sciencedirect.com/science/article/pii/S025789720301154X.

[228] P. Sutor, MRS Bulletin **16**, 24 (1991).

[229] W. Guo, J. Yin, H. Qiu, Y. Guo, H. Wu, and M. Xue, Friction **2**, 209 (2014), ISSN 2223-7704, URL https://doi.org/10.1007/s40544-014-0064-0.

[230] D. Berman, A. Erdemir, and A. V. Sumant, ACS Nano **12**, 2122 (2018), pMID: 29522673, https://doi.org/10.1021/acsnano.7b09046, URL https://doi.org/10.1021/acsnano.7b09046.

[231] D. Berman, A. Erdemir, and A. V. Sumant, Materials Today **17**, 31 (2014), ISSN 1369-7021, URL http://www.sciencedirect.com/science/article/pii/S1369702113004574.

[232] R. Zhang, Z. Ning, Y. Zhang, Q. Zheng, Q. Chen, H. Xie, Q. Zhang, W. Qian, and F. Wei, Nature nanotechnology **8**, 912 (2013), URL https://www.nature.com/articles/nnano.2013.217.

[233] A. Erdemir and C. Donnet, Journal of Physics D: Applied Physics **39**, R311 (2006), URL https://doi.org/110.1088/0022-3727/39/18/R01.

[234] V. Smil, *Natural gas: fuel for the 21st century* (John Wiley & Sons, 2015).

[235] W. Oliver and G. Pharr, Journal of Materials Research **7**, 1564 (1992).

[236] D. J. Klinke, S. Wilke, and L. J. Broadbelt, Journal of Catalysis **178**, 540 (1998), ISSN 0021-9517, URL http://www.sciencedirect.com/science/article/pii/S0021951798921753.

[237] H. Burghgraef, A. Jansen, and R. van Santen, Surface Science **324**, 345 (1995), ISSN 0039-6028, URL http://www.sciencedirect.com/science/article/pii/0039602894007160.

[238] R. Watwe, H. Bengaard, J. Rostrup-Nielsen, J. Dumesic, and J. Nazrskov, Journal of Catalysis **189**, 16 (2000), ISSN 0021-9517, URL http://www.sciencedirect.com/science/article/pii/S0021951799926994.

[239] Y. Zhang, L. Zhang, and C. Zhou, Accounts of Chemical Research **46**, 2329 (2013), pMID: 23480816, https://doi.org/10.1021/ar300203n, URL https://doi.org/10.1021/ar300203n.

[240] S. M. Kozlov, F. Vies, and A. Grling, The Journal of Physical Chemistry C **116**, 7360 (2012), https://doi.org/10.1021/jp210667f, URL https://doi.org/10.1021/jp210667f.

[241] K. S. Kim, Y. Zhao, H. Jang, S. Y. Lee, J. M. Kim, K. S. Kim, J.-H. Ahn, P. Kim, J.-Y. Choi, and B. H. Hong, nature **457**, 706 (2009), URL https://www.nature.com/articles/nature07719.

[242] A. Reina, X. Jia, J. Ho, D. Nezich, H. Son, V. Bulovic, M. S. Dresselhaus, and J. Kong, Nano Letters **9**, 30 (2009), pMID: 19046078, https://doi.org/10.1021/nl801827v, URL https://doi.org/10.1021/nl801827v.

[243] L. L. Patera, C. Africh, R. S. Weatherup, R. Blume, S. Bhardwaj, C. Castellarin-Cudia, A. Knop-Gericke, R. Schloegl, G. Comelli, S. Hofmann, et al., ACS Nano **7**, 7901 (2013), pMID: 23924234, https://doi.org/10.1021/nn402927q, URL https://doi.org/10.1021/nn402927q.

[244] H. Kwon, S. Choi, and L. Thompson, Journal of Catalysis **184**, 236 (1999), ISSN 0021-9517, URL http://www.sciencedirect.com/science/article/pii/S0021951799924508.

[245] S. Oyama, Journal of Catalysis **133**, 358 (1992), ISSN 0021-9517, URL http://www.sciencedirect.com/science/article/pii/002195179290246E.

[246] S. Ramanathan and S. T. Oyama, The Journal of Physical Chemistry **99**, 16365 (1995), https://doi.org/10.1021/j100044a025, URL https://doi.org/10.1021/j100044a025.

[247] S. Lim and M. Ashby, Acta Metallurgica **35**, 1 (1987), ISSN 0001-6160, URL http://www.sciencedirect.com/science/article/pii/0001616087902094.

[248] F. Abild-Pedersen, O. Lytken, J. Engbk, G. Nielsen, I. Chorkendorff, and J. K. Nrskov, Surface Science **590**, 127 (2005), ISSN 0039-6028, URL http://www.sciencedirect.com/science/article/pii/S0039602805006126.

[249] W. An, X. C. Zeng, and C. H. Turner, The Journal of Chemical Physics **131**, 174702 (2009), https://doi.org/10.1063/1.3254383, URL https://doi.org/10.1063/1.3254383.

[250] Y. Shibuta, R. Arifin, K. Shimamura, T. Oguri, F. Shimojo, and S. Yamaguchi, Chemical Physics Letters **565**, 92 (2013), ISSN 0009-2614, URL http://www.sciencedirect.com/science/article/pii/S0009261413002479.

[251] Y. Liao, R. Pourzal, M. A. Wimmer, J. J. Jacobs, A. Fischer, and L. D. Marks, Science **334**, 1687 (2011), ISSN 0036-8075, https://science.sciencemag.org/content/334/6063/1687.full.pdf, URL https://science.sciencemag.org/content/334/6063/1687.

[252] A. Erdemir, G. Ramirez, O. L. Eryilmaz, B. Narayanan, Y. Liao, G. Kamath, and S. K. Sankaranarayanan, Nature **536**, 67 (2016), URL https://www.nature.com/articles/nature18948.

[253] Z. Fuadi, K. Adachi, and T. Muhammad, Tribology Letters **66**, 88 (2018), ISSN 1573-2711, URL https://doi.org/10.1007/s11249-018-1036-8.

[254] G. Fatti, M. C. Righi, D. Dini, and A. Ciniero, The Journal of Physical Chemistry C **123**, 6250 (2019), https://doi.org/10.1021/acs.jpcc.8b11631, URL https://doi.org/10.1021/acs.jpcc.8b11631.

[255] T. A. L. Burgo, T. R. D. Ducati, K. R. Francisco, K. J. Clinckspoor, F. Galembeck, and S. E. Galembeck, Langmuir **28**, 7407 (2012), pMID: 22530971, https://doi.org/10.1021/la301228j, URL https://doi.org/10.1021/la301228j.

[256] T. A. L. Burgo and A. Erdemir, Angewandte Chemie **126**, 12297 (2014), https://onlinelibrary.wiley.com/doi/pdf/10.1002/ange.201406541, URL https://onlinelibrary.wiley.com/doi/abs/10.1002/ange.201406541.

[257] K. Nakayama, Wear **194**, 185 (1996), ISSN 0043-1648, URL http://www.sciencedirect.com/science/article/pii/0043164895068406.

[258] D. Puhan, R. Nevshupa, J. S. Wong, and T. Reddyhoff, Tribology International **130**, 366 (2019), ISSN 0301-679X, URL http://www.sciencedirect.com/science/article/pii/S0301679X18304766.

[259] C. A. Rezende, R. F. Gouveia, M. A. da Silva, and F. Galembeck, Journal of Physics: Condensed Matter **21**, 263002 (2009), URL https://doi.org/10.1088/0953-8984/21/26/263002.

[260] A. Ciniero, J. Le Rouzic, and T. Reddyhoff, Coatings **7**, 129 (2017), ISSN 2079-6412, URL http://dx.doi.org/10.3390/coatings7080129.

[261] D. Lacks and R. Sankaran, Journal of Physics D: Applied Physics **44**, 453001 (2011), URL https://doi.org/10.1088/10.1088/0022-3727/44/45/453001.

[262] H. T. Baytekin, B. Baytekin, J. T. Incorvati, and B. A. Grzybowski, Angewandte Chemie International Edition **51**, 4843 (2012), https://onlinelibrary.wiley.com/doi/pdf/10.1002/anie.201200057, URL https://onlinelibrary.wiley.com/doi/abs/10.1002/anie.201200057.

[263] T. Friščić, S. L. James, E. V. Boldyreva, C. Bolm, W. Jones, J. Mack, J. W. Steed, and K. S. Suslick, Chemical Communications **51**, 6248 (2015), URL https://pubs.rsc.org/en/content/articlehtml/2015/cc/c5cc90113h.

[264] A. Mokha, M. Constantinou, and A. Reinhorn, Journal of Structural Engineering **116**, 438 (1990), URL https://ascelibrary.org/doi/abs/10.1061/(ASCE)0733-9445(1990)116:2(438).

[265] J. Lancaster, Tribology International **12**, 65 (1979), ISSN 0301-679X, URL http://www.sciencedirect.com/science/article/pii/0301679X79900045.

[266] C. Daraio, V. F. Nesterenko, E. B. Herbold, and S. Jin, Phys. Rev. E **72**, 016603 (2005), URL https://link.aps.org/doi/10.1103/PhysRevE.72.016603.

[267] D. W. Grainger and C. W. Stewart, *Fluorinated Coatings and Films: Motivation and Significance* (ACD Publications, 2001), chap. 1, pp. 1–14, https://pubs.acs.org/doi/pdf/10.1021/bk-2001-0787.ch001, URL https://pubs.acs.org/doi/abs/10.1021/bk-2001-0787.ch001.

[268] D. Clark and D. Kilcast, Nature Physical Science **233**, 77 (1971), URL https://www.nature.com/articles/physci233077a0.

[269] J. Pireaux, J. Riga, R. Caudano, J. Verbist, J. Andre, J. Delhalle, and S. Delhalle, Journal of Electron Spectroscopy and Related Phenomena **5**, 531 (1974), ISSN 0368-2048, the International Journal on Theoretical and Experimental Aspects of Electron Spectroscopy, URL http://www.sciencedirect.com/science/article/pii/0368204874850358.

[270] J. Delhalle, Chemical Physics **5**, 306 (1974), ISSN 0301-0104, URL http://www.sciencedirect.com/science/article/pii/0301010474800297.

[271] K. Seki, H. Tanaka, T. Ohta, Y. Aoki, A. Imamura, H. Fujimoto, H. Yamamoto, and H. Inokuchi, Physica Scripta **41**, 167 (1990), URL https://doi.org/10.1088/0031-8949/41/1/041.

[272] C. Nakafuku and T. Takemura, Japanese Journal of Applied Physics **14**, 599 (1975), URL https://doi.org/10.1143/JJAP.14.599.

[273] R. Roberts, R. Rowe, and P. York, Powder Technology **65**, 139 (1991), ISSN 0032-5910, a Special Volume Devoted to the Second Symposium on Advances in Particulate Technology, URL http://www.sciencedirect.com/science/article/pii/003259109180176J.

[274] B.-B. Jia, X.-J. Liu, P.-H. Cong, and T.-S. Li, Wear **264**, 685 (2008), ISSN 0043-1648, URL http://www.sciencedirect.com/science/article/pii/S0043164807005728.

[275] S. B. Dake, N. R. Rajopadhye, and S. V. Bhoraskar, Journal of Physics D: Applied Physics **20**, 1631 (1987), URL https://doi.org/10.1088/0022-3727/20/12/014.

[276] J. E. Falk and R. J. Fleming, Journal of Physics C: Solid State Physics **8**, 627 (1975), URL https://doi.org/10.1088/0022-3719/8/5/010.

[277] S. Serra, E. Tosatti, S. Iarlori, S. Scandolo, and G. Santoro, Phys. Rev. B **62**, 4389 (2000), URL https://link.aps.org/doi/10.1103/PhysRevB.62.4389.

[278] C. Wang, G. Duscher, and S. J. Paddison, Microscopy **63**, 73 (2013), ISSN 2050-5698, http://oup.prod.sis.lan/jmicro/article-pdf/63/1/73/14099000/dft046.pdf, URL https://doi.org/10.1093/jmicro/dft046.

[279] K. Morokuma, The Journal of Chemical Physics **54**, 962 (1971), https://doi.org/10.1063/1.1675026, URL https://doi.org/10.1063/1.1675026.

[280] W. McCubbin, Chemical Physics Letters **8**, 507 (1971), ISSN 0009-2614, URL http://www.sciencedirect.com/science/article/pii/0009261471800799.

[281] R. V. Kasowski, W. Y. Hsu, and E. B. Caruthers, The Journal of Chemical Physics **72**, 4896 (1980), https://doi.org/10.1063/1.439773, URL https://doi.org/10.1063/1.439773.

[282] P. Otto, J. Ladik, and W. Forner, Chemical Physics **95**, 365 (1985), ISSN 0301-0104, URL http://www.sciencedirect.com/science/article/pii/0301010485801592.

[283] M. D'Amore, G. Talarico, and V. Barone, Journal of the American Chemical Society **128**, 1099 (2006), pMID: 16433525, https://doi.org/10.1021/ja0527929, URL https://doi.org/10.1021/ja0527929.

[284] M. D'Amore, F. Auriemma, C. De Rosa, and V. Barone, Macromolecules **37**, 9473 (2004), https://doi.org/10.1021/ma0488257, URL https://doi.org/10.1021/ma0488257.

[285] M. Lorenzen, M. Hanfland, and A. Mermet, Nuclear Instruments and Methods in Physics Research Section B: Beam Interactions with Materials and Atoms **200**, 416 (2003), ISSN 0168-583X, proceedings of the E-MRS 2002 Symposium I on Synchrotron Radiation and Materials Science, URL http://www.sciencedirect.com/science/article/pii/S0168583X02017329.

[286] M. Springborg and M. Lev, Phys. Rev. B **40**, 3333 (1989), URL https://link.aps.org/doi/10.1103/PhysRevB.40.3333.

[287] C. Bunn and E. Howells, Nature **174**, 549 (1954), URL https://www.nature.com/articles/174549a0.

[288] J. Weeks, E. Clark, and R. Eby, Polymer **22**, 1480 (1981), ISSN 0032-3861, URL http://www.sciencedirect.com/science/article/pii/0032386181903165.

[289] B. Farmer and R. Eby, Polymer **22**, 1487 (1981), ISSN 0032-3861, URL http://www.sciencedirect.com/science/article/pii/0032386181903177.

[290] C. A. Sperati and H. W. Starkweather, in *Fortschritte Der Hochpolymeren-Forschung* (Springer Berlin Heidelberg, Berlin, Heidelberg, 1961), pp. 465–495, ISBN 978-3-540-37047-5.

[291] R. G. Brown, The Journal of Chemical Physics **40**, 2900 (1964), https://doi.org/10.1063/1.1724924, URL https://doi.org/10.1063/1.1724924.

[292] H. D. Flack, Journal of Polymer Science Part A-2: Polymer Physics **10**, 1799 (1972), https://onlinelibrary.wiley.com/doi/pdf/10.1002/pol.1972.160100915, URL https://onlinelibrary.wiley.com/doi/abs/10.1002/pol.1972.160100915.

[293] R. Eby, E. Clark, B. Farmer, G. Piermarini, and S. Block, Polymer **31**, 2227 (1990), ISSN 0032-3861, URL http://www.sciencedirect.com/science/article/pii/003238619090307K.

[294] J. P. Perdew and A. Zunger, Phys. Rev. B **23**, 5048 (1981), URL https://link.aps.org/doi/10.1103/PhysRevB.23.5048.

[295] M. Ernzerhof and G. E. Scuseria, The Journal of Chemical Physics **110**, 5029 (1999), https://doi.org/10.1063/1.478401, URL https://doi.org/10.1063/1.478401.

[296] S. Grimme, Journal of Computational Chemistry **27**, 1787 (2006), https://onlinelibrary.wiley.com/doi/pdf/10.1002/jcc.20495, URL https://onlinelibrary.wiley.com/doi/abs/10.1002/jcc.20495.

[297] M. C. Righi, S. Scandolo, S. Serra, S. Iarlori, E. Tosatti, and G. Santoro, Phys. Rev. Lett. **87**, 076802 (2001), URL https://link.aps.org/doi/10.1103/PhysRevLett.87.076802.

[298] E. N. Brown, C. P. Trujillo, G. T. Gray, P. J. Rae, and N. K. Bourne, Journal of Applied Physics **101**, 024916 (2007), https://doi.org/10.1063/1.2424536, URL https://doi.org/10.1063/1.2424536.

[299] F. D. Murnaghan, Proceedings of the National Academy of Sciences **30**, 244 (1944), ISSN 0027-8424, https://www.pnas.org/content/30/9/244.full.pdf, URL https://www.pnas.org/content/30/9/244.

[300] J. P. Perdew and M. Levy, Phys. Rev. Lett. **51**, 1884 (1983), URL https://link.aps.org/doi/10.1103/PhysRevLett.51.1884.

[301] G. Fatti, M. C. Righi, D. Dini, and A. Ciniero, The Journal of Physical Chemistry C **123**, 6250 (2019), https://doi.org/10.1021/acs.jpcc.8b11631, URL https://doi.org/10.1021/acs.jpcc.8b11631.

[302] P. C. Sinclair, Journal of Applied Meteorology **8**, 32 (1969), https://doi.org/10.1175/1520-0450(1969)008<0032:GCODD>2.0.CO;2, URL https://doi.org/10.1175/1520-0450(1969)008<0032:GCODD>2.0.CO;2.

[303] S. Wang, L. Lin, and Z. L. Wang, Nano Letters **12**, 6339 (2012), pMID: 23130843, https://doi.org/10.1021/nl303573d, URL https://doi.org/10.1021/nl303573d.

[304] K. Nakayama and H. Hashimoto, Wear **147**, 335 (1991), ISSN 0043-1648, URL http://www.sciencedirect.com/science/article/pii/0043164891901906.

[305] K. Nakayama, Tribology Letters **6**, 37 (1999), ISSN 1573-2711, URL https://doi.org/10.1023/A:1019139002295.

[306] J. T. Dickinson, E. E. Donaldson, and M. K. Park, Journal of Materials Science **16**, 2897 (1981), ISSN 1573-4803, URL https://doi.org/10.1007/BF00552976.

[307] J. Dickinson, D. Snyder, and E. Donaldson, Thin Solid Films **72**, 223 (1980), ISSN 0040-6090, URL http://www.sciencedirect.com/science/article/pii/0040609080900024.

[308] A. Ciniero, J. L. Rouzic, I. Baikie, and T. Reddyhoff, Wear **374-375**, 113 (2017), ISSN 0043-1648, URL http://www.sciencedirect.com/science/article/pii/S0043164817300686.

[309] X. Zhao and B. Bhushan, Proceedings of the Institution of Mechanical Engineers, Part J: Journal of Engineering Tribology **215**, 173 (2001), https://doi.org/10.1243/1350650011541819, URL https://doi.org/10.1243/1350650011541819.

[310] T. Kasai, X. Fu, D. Rigney, and A. Zharin, Wear **225-229**, 1186 (1999), ISSN 0043-1648, URL http://www.sciencedirect.com/science/article/pii/S0043164899000575.

[311] D. DeVecchio and B. Bhushan, Review of Scientific Instruments **69**, 3618 (1998), https://doi.org/10.1063/1.1149148, URL https://doi.org/10.1063/1.1149148.

[312] A. L. Zharin and D. A. Rigney, Tribology Letters **4**, 205 (1998), ISSN 1573-2711, URL https://doi.org/10.1023/A:1019171625552.

[313] K. Goto, Wear **185**, 75 (1995), ISSN 0043-1648, URL http://www.sciencedirect.com/science/article/pii/0043164895066004.

[314] N. P. Brandon, N. Bonanos, P. O. Fogarty, M. N. Mahmood, A. J. Moore, and R. J. K. Wood, Journal of Applied Electrochemistry **23**, 456 (1993), ISSN 1572-8838, URL https://doi.org/10.1007/BF00707622.

[315] K. Nakayama, N. Suzuki, and H. Hashimoto, Journal of Physics D: Applied Physics **25**, 303 (1992), URL https://doi.org/10.1088/0022-3727/25/2/027/.

[316] K. Nakayama, Surface and Coatings Technology **188-189**, 599 (2004), ISSN 0257-8972, proceedings of the 31st International Conference on Metallurgical Coatings and Thin Films, URL http://www.sciencedirect.com/science/article/pii/S0257897204005602.

[317] K. Nakayama, J. A. Leiva, and Y. Enomoto, Tribology International **28**, 507 (1995), ISSN 0301-679X, URL http://www.sciencedirect.com/science/article/pii/0301679X96855381.

[318] J. Le Rouzic and T. Reddyhoff, Tribology Letters **55**, 245 (2014), ISSN 1573-2711, URL https://doi.org/10.1007/s11249-014-0352-x.

[319] J. L. Wiza, Nuclear Instruments and Methods **162**, 587 (1979), ISSN 0029-554X, URL http://www.sciencedirect.com/science/article/pii/0029554X79907341.

[320] S. Susman, K. J. Volin, D. L. Price, M. Grimsditch, J. P. Rino, R. K. Kalia, P. Vashishta, G. Gwanmesia, Y. Wang, and R. C. Liebermann, Phys. Rev. B **43**, 1194 (1991), URL https://link.aps.org/doi/10.1103/PhysRevB.43.1194.

[321] J. Yu, S. B. Sinnott, and S. R. Phillpot, Phys. Rev. B **75**, 085311 (2007), URL https://link.aps.org/doi/10.1103/PhysRevB.75.085311.

[322] S. Plimpton, Journal of Computational Physics **117**, 1 (1995), ISSN 0021-9991, URL http://www.sciencedirect.com/science/article/pii/S002199918571039X.

[323] T.-R. Shan, B. D. Devine, J. M. Hawkins, A. Asthagiri, S. R. Phillpot, and S. B. Sinnott, Phys. Rev. B **82**, 235302 (2010), URL https://link.aps.org/doi/10.1103/PhysRevB.82.235302.

[324] G. D. Mukherjee, S. N. Vaidya, and V. Sugandhi, Phys. Rev. Lett. **87**, 195501 (2001), URL https://link.aps.org/doi/10.1103/PhysRevLett.87.195501.

[325] R. L. Mozzi and B. E. Warren, Journal of Applied Crystallography **2**, 164 (1969), URL https://doi.org/10.1107/S0021889869006868.

[326] G. Levita, S. Kajita, and M. Righi, Carbon **127**, 533 (2018), ISSN 0008-6223, URL http://www.sciencedirect.com/science/article/pii/S0008622317311132.

[327] D. Petrini and K. Larsson, The Journal of Physical Chemistry C **112**, 3018 (2008), https://doi.org/10.1021/jp709625a, URL https://doi.org/10.1021/jp709625a.

[328] S. J. Sque, R. Jones, and P. R. Briddon, Phys. Rev. B **73**, 085313 (2006), URL https://link.aps.org/doi/10.1103/PhysRevB.73.085313.

[329] G. Kern, J. Hafner, and G. Kresse, Surface Science **366**, 445 (1996), ISSN 0039-6028, URL http://www.sciencedirect.com/science/article/pii/0039602896008370.

[330] G. Feldbauer, M. Wolloch, P. O. Bedolla, J. Redinger, A. Vernes, and P. Mohn, Journal of Physics: Condensed Matter **30**, 105001 (2018), URL https://doi.org/10.1088/1361-648X/aaac91/.

[331] J. Lowell and W. S. Truscott, Journal of Physics D: Applied Physics **19**, 1273 (1986), URL https://doi.org/10.1088/0022-3727/19/7/017/.

[332] J. Lowell, Journal of Physics D: Applied Physics **24**, 375 (1991), URL https://doi.org/10.1088/0022-3727/24/3/021.

[333] J. Lowell, Journal of Physics D: Applied Physics **23**, 1082 (1990), URL https://doi.org/10.1088/0022-3727/23/8/014.

[334] J. Dickinson, L. Scudiero, K. Yasuda, M.-W. Kim, and S. Langford, Tribology Letters **3**, 53 (1997), ISSN 1573-2711, URL https://doi.org/10.1023/A:1019187812406.

[335] G. J. Molina, M. J. Furey, A. Ritter, and C. Kajdas, Wear **249**, 214 (2001), ISSN 0043-1648, proceedings of the ninth Nordic Symposium on Tribology, URL http://www.sciencedirect.com/science/article/pii/S0043164801005683.

[336] Y. Momose, Y. Yamashita, and M. Honma, Tribology Letters **29**, 75 (2008), ISSN 1573-2711, URL https://doi.org/10.1007/s11249-007-9284-z.

[337] M. I. Kornfeld, Journal of Physics D: Applied Physics **9**, 1183 (1976), URL https://doi.org/10.1088/0022-3727/9/8/005.

[338] I. L. Singer, S. D. Dvorak, K. J. Wahl, and T. W. Scharf, Journal of Vacuum Science & Technology A **21**, S232 (2003), https://doi.org/10.1116/1.1599869, URL https://doi.org/10.1116/1.1599869.

[339] J. Robertson, Materials Science and Engineering: R: Reports **37**, 129 (2002), ISSN 0927-796X, URL http://www.sciencedirect.com/science/article/pii/S0927796X02000050.

[340] L. Wan and R. Egerton, Thin Solid Films **279**, 34 (1996), ISSN 0040-6090, URL http://www.sciencedirect.com/science/article/pii/0040609095081267.